

COVER PAGE

April 11, 2021

External surface water influence on explosive eruption dynamics, with implications for stratospheric sulfur delivery and volcano-climate feedback

Colin R. Rowell^{1,*}, A. Mark Jellinek¹, Sahand Hajimirza², Thomas J. Aubry^{3,4}

¹Department of Earth, Ocean, and Atmospheric Sciences, University of British Columbia, Vancouver , British Columbia , Canada

²Department of Earth, Environmental, and Planetary Sciences, Rice University, Houston , Texas, USA

³Department of Geography, University of Cambridge, Cambridge, UK

⁴Sidney Sussex College, Cambridge, UK

Correspondence*:

Corresponding Author

crowell@eoas.ubc.ca

This article is a preprint submitted to EarthArXiv, and has been accepted for publication in “Frontiers in Earth Science.” As of the listed date above, this is the final accepted version of the manuscript. The final peer-reviewed DOI is available on the corresponding Earth ArXiv webpage.

Please feel free to contact the lead author (Colin Rowell) with questions or feedback.

External surface water influence on explosive eruption dynamics, with implications for stratospheric sulfur delivery and volcano-climate feedback

Colin R. Rowell^{1,*}, A. Mark Jellinek¹, Sahand Hajimirza², and Thomas J. Aubry^{3,4}

¹*Department of Earth, Ocean, and Atmospheric Sciences, University of British Columbia, Vancouver, British Columbia, Canada*

²*Department of Earth, Environmental, and Planetary Sciences, Rice University, Houston, Texas, USA*

³*Department of Geography, University of Cambridge, Cambridge, UK*

⁴*Sidney Sussex College, Cambridge, UK*

Correspondence*:
Corresponding Author
crowell@eoas.ubc.ca

2 ABSTRACT

3

4 Explosive volcanic eruptions can inject sulfur dioxide (SO₂) into the stratosphere to form aerosol
5 particles that modify Earth's radiation balance and drive surface cooling. Eruptions involving
6 interactions with shallow layers (≤ 500 m) of surface water and ice modify the eruption dynamics
7 that govern the delivery of SO₂ to the stratosphere. External surface water controls the evolution
8 of explosive eruptions in two ways that are poorly understood: (1) by modulating the hydrostatic
9 pressure within the conduit and at the vent, and (2) through the ingestion and mixing of external
10 water, which governs fine ash production and eruption column buoyancy flux. To make progress,
11 we couple one-dimensional models of conduit flow and atmospheric column rise through a novel
12 "magma-water interaction" model that simulates the occurrence, extent and consequences of
13 water entrainment depending on the depth of a surface water layer. We explore the effects of
14 hydrostatic pressure on magma ascent in the conduit and gas decompression at the vent, and
15 the conditions for which water entrainment drives fine ash production by quench fragmentation,
16 eruption column collapse, or outright failure of the jet to breach the water surface. We show that
17 the efficiency of water entrainment into the jet is the predominant control on jet behavior. For an
18 increase in water depth of 50 to 100 m, the critical magma mass eruption rate required for eruption
19 columns to reach the tropopause increases by an order of magnitude. Finally, we estimate that
20 enhanced emission of fine ash leads to up to a 2-fold increase in the mass flux of particles $<$
21 $125 \mu\text{m}$ to spreading umbrella clouds, together with up to a 10-fold increase in water mass flux,
22 conditions that can enhance the removal of SO₂ via chemical scavenging and ash sedimentation.
23 On average, compared to purely magmatic eruptions, we suggest that hydrovolcanic eruptions
24 will be characterized by reduced climate forcing. Our results suggest one possible mechanism for
25 volcano-climate feedback: temporal changes with climate in surface distributions of water and
26 ice may modify the relative global frequency or dominance of hydrovolcanic eruption processes,
27 modulating, in turn, global patterns in volcano-climate forcing.

28 **Keywords:** External forcing, Hydrovolcanism, magma-water interactions, Explosive eruptions, 1D plume model, 1D conduit flow
29 model, Stratospheric sulfur input, Climate feedback

1 INTRODUCTION

30 Volcanic SO₂ injected into the stratosphere forms sulfate aerosols that persist for 1-3 years, affect Earth's
31 radiation balance and produce one of the strongest natural surface climate cooling mechanisms (Timmreck,
32 2012; Sigl et al., 2015; Kremser et al., 2016). Although the direct radiative forcing from volcanic aerosols
33 typically acts over annual to decadal timescales (Robock, 2000), the last decade of research has shown
34 that the climate impacts of eruptions are not restricted to discrete and intermittent cooling events with
35 durations of a few years. For example, volcanic emission from small to moderate eruptions and passive
36 degassing provide background concentrations of sulfate aerosols, resulting in a near-continuous negative
37 (cooling) forcing to the planetary surface (Solomon et al., 2011; Schmidt et al., 2012; Santer et al., 2014).
38 Furthermore, a growing body of evidence suggests that volcanic forcing from aerosols can also drive
39 non-linear climate responses on multidecadal to millennial timescales (Zhong et al., 2011; Schleussner
40 and Feulner, 2013; Zanchettin et al., 2013; Santer et al., 2014; Baldini et al., 2015; Toohey et al., 2016;
41 Soreghan et al., 2019; Mann et al., 2021). The strength of aerosol climate forcing depends strongly on the
42 SO₂ mass flux to the stratosphere (e.g. Marshall et al. (2019)), which is governed by the eruption magnitude
43 and eruption column height (the altitude at which gas and ash are dispersed as a neutrally buoyant cloud)
44 relative to the tropopause (Aubry et al., 2019; Marshall et al., 2019; Krishnamohan et al., 2019; Aubry
45 et al., 2021b). In addition to the injection height of SO₂, the chemistry and microphysics governing aerosol
46 formation and stratospheric residence time are also critical controls on the climate effects of eruptions
47 (Timmreck, 2012; Kremser et al., 2016; LeGrande et al., 2016; Zhu et al., 2020; Staunton-Sykes et al.,
48 2021). SO₂ is frequently transported together with fine ash and water from the eruption column (e.g. Rose
49 et al., 2001; Ansmann et al., 2011), where chemical scavenging of SO₂ onto ash surfaces (Rose, 1977;
50 Schmauss and Keppler, 2014) and physical incorporation into hydrometeors (Rose et al., 1995; Textor
51 et al., 2003) can scrub SO₂ from the eruption column. Water transported by the eruption cloud can enhance
52 nucleation and growth rates of aerosol particles (LeGrande et al., 2016), and ash particles provide sites
53 for aerosol nucleation or direct uptake of SO₂ (Zhu et al., 2020). Consequently, the presence of water
54 and fine ash influences resulting aerosol formation rates, particle sizes, optical properties, and residence
55 times, which are key parameters governing climate forcing (Kremser et al., 2016). Constraining the climate
56 impacts of volcanic eruptions therefore requires understanding of eruption transport processes governing
57 injection height, as well as the quantities of fine ash and water in eruption columns and clouds.

58 Climate-forcing related to eruptions is sensitive to the environmental conditions of eruptions as well as
59 global eruption frequency-magnitude distributions, both of which can evolve with global climate warming
60 or cooling. For example, sustained anthropogenic climate change will drive an increase in the strength
61 of tropospheric density stratification and tropopause height, and alter stratospheric circulation. These
62 atmospheric changes are expected to reduce the stratospheric delivery of SO₂ in moderate-magnitude
63 eruptions (Aubry et al., 2016, 2019), while exacerbating the radiative effects of relatively rare, large-
64 magnitude eruptions (e.g. Pinatubo 1991) (Aubry et al., 2021b). Other potential mechanisms for climatic
65 influence on volcanism include eruption triggering by extreme rainfall events (e.g. Elsworth et al., 2004;
66 Capra, 2006; Farquharson and Amelung, 2020) or changes to ocean stratification (Fasullo et al., 2017).
67 Glacial-interglacial cycles also influence rates and locations of global volcanism: The advance and retreat
68 of ice sheets and thickening and thinning of mountain glaciers can inhibit or enhance, respectively, melt
69 generation, dike formation, eruption rates and eruption frequency (Jull and McKenzie, 1996; Jellinek

70 et al., 2004; Huybers and Langmuir, 2009; Watt et al., 2013; Baldini et al., 2015; Cooper et al., 2018).
71 For example, Huybers and Langmuir (2009) correlated observed spikes in atmospheric CO₂ with inferred
72 increases in the rate of volcanism following the Last Glacial Maximum, and proposed a glaciovolcanic-CO₂
73 feedback, where enhanced rates of volcanism and CO₂ outgassing contribute to additional warming and
74 ice sheet loss. Increases in both sea level and in the occurrence and extents of freshwater lakes and ponds
75 with deglaciation are also likely to increase the frequency of direct interactions of erupting magma with
76 surface water. Crucially, the implications of potentially enhanced magma-water interaction (MWI) for
77 volcano-climate forcing remain largely unexplored.

78 Explosive volcanic eruptions involving interactions of magma with external surface water or ice (termed
79 hereafter *hydrovolcanic eruptions*) evolve as a result of thermophysical and chemical processes that are
80 wholly distinct from those of “dry” magmatic eruptions (those in which the main component of water
81 present is that exsolved from the melt) (Self and Sparks, 1978; Houghton et al., 2015). Figure 1 shows a
82 summary of hydrovolcanic eruption processes affecting the transport and stratospheric delivery of SO₂
83 as compared with purely magmatic eruptions. The presence of external surface water influences eruption
84 dynamics and evolution through two primary controls: (1) a modulation of hydrostatic pressure at the vent
85 and within the erupting conduit, and (2) through effects of the entrainment and thermal and mechanical
86 mixing of water into an erupting gas-pyroclast mixture on the mass, momentum, particle and enthalpy
87 fluxes that ultimately drive column rise (Woods, 2010; Wohletz et al., 2013; Smellie and Edwards, 2016;
88 Cas and Simmons, 2018). Increased hydrostatic pressure can, for example, reduce eruption explosivity by
89 suppressing bubble nucleation and growth in the conduit, reducing magma decompression and ascent rates,
90 and potentially preventing magmatic fragmentation (Smellie and Edwards, 2016; Cas and Simmons, 2018;
91 Manga et al., 2018). In contrast, secondary fragmentation and ash production can be relatively enhanced as
92 a result of the actions of large thermal stresses arising through the rapid transfer of heat from hot pyroclasts
93 to entrained surface water (Gonnermann, 2015; van Otterloo et al., 2015; Zimanowski et al., 2015). Heat
94 consumption by the vaporization of entrained external water results in a loss (or redistribution) of the
95 thermal buoyancy delivered by the eruption at the vent, which may be recovered via condensation higher in
96 the plume where temperatures are colder (Koyaguchi and Woods, 1996).

97 The extent to which water is mixed into the erupting jet and the efficiency of heat transfer between hot
98 pyroclasts and this ingested water controls the eruption column source parameters (e.g. bulk temperature,
99 density, velocity, and column radius) (Koyaguchi and Woods, 1996; Mastin, 2007b), as well as the intensity
100 of secondary fragmentation and ash production that governs the ultimate particle size distribution (PSD -
101 we refer to total particle size distributions throughout unless otherwise stated) (Mastin, 2007a; van Otterloo
102 et al., 2015). The character of the PSD governs the rates of particle aggregation and sedimentation, as
103 well as the available particle surface area (Bonadonna et al., 1998; Brown et al., 2012; Girault et al.,
104 2014). In particular, increased water content, ash surface area, and relatively colder temperatures in the
105 rising eruption column provide conditions that enhance chemical scavenging of SO₂ during transport and
106 dispersal relative to dry eruptions (Schmauss and Keppler, 2014). For example, Textor et al. (2003) simulate
107 dynamical, chemical, and microphysical processes occurring in a dry Plinian eruption and estimate that the
108 percent of SO₂ erupted at the vent that is ultimately injected into the stratosphere was \gtrsim 80%. However, in
109 marked contrast, for the glaciovolcanic eruption of Grimsvötn in 2011, Sigmarsson et al. (2013) estimate
110 that approximately 50% of the exsolved sulfur gas was dispersed to the atmosphere, with much of the
111 remainder lost to scavenging by ash particles or external surface water. As another provocative example,
112 the recent powerful and water-rich eruption of Hunga Tonga-Hunga Ha’apai injected an eruption cloud
113 to at least 30 to 35 km above sea level. Despite a cloud height comparable to the 1991 eruption of Mt.
114 Pinatubo (Bluth et al., 1997), preliminary analyses have suggested stratospheric loading of SO₂ for the

115 recent eruption is likely comparatively negligible. The exact cause for this discrepancy between apparent
116 eruption magnitude and SO₂ output for Hunga Tonga-Hunga Ha'apai relative to Mt. Pinatubo is currently
117 undetermined, but the water-rich nature of the eruption is one possible cause.

118 Magma-water interactions (MWI) and their effects throughout an eruptive phase are maximized in
119 persistent deep layers of water where significant entrainment can occur over the time of column rise.
120 In subglacial or subaqueous environments where water availability is limited by, say, ice melting and
121 melt-water drainage (e.g. Gudmundsson et al., 2012; Magnússon et al., 2012), build-up of insulating
122 volcanic tephra (e.g. Fee et al., 2020), or by simply the finite volume of a reservoir (e.g. Gudmundsson
123 et al., 2014), water access to the volcanic vent can decline during an eruption, causing the extent of MWI to
124 evolve, in turn. With declining water layer depths, eruptions styles may progress from an initial suppression
125 of explosive behavior, to collapsing jets, to buoyant plumes of increasing height (Koyaguchi and Woods,
126 1996; Mastin, 2007b; Van Eaton et al., 2012; Wohletz et al., 2013; Manga et al., 2018). This evolution
127 is important to recognize: the degree to which an erupting magma interacts with surface water can exert
128 critical control over the ultimate delivery of ash, water, and SO₂ into the troposphere and stratosphere (Rose
129 et al., 1995). Although observational, experimental, and numerical studies have individually investigated
130 processes relevant to hydrovolcanic eruptions, it is critical to assess their behavior as a system to reveal
131 controls on the ultimate fate of erupted ash and gas.

132 To make critical progress in understanding the extent to which surface water governs the character and
133 magnitude of volcano-climate forcing, it is necessary to examine syn-eruptive processes that determine the
134 transport and ultimate fate of volcanic SO₂. In particular:

- 135 1. How do hydrostatic pressure, water entrainment, and MWI affect the coupled dynamics of gas
136 exsolution and magma fragmentation in the subterranean conduit, heat transfer from pyroclasts to
137 external water, secondary production of fine ash, and transport of ash, water, and SO₂ in the eruption
138 column?
- 139 2. To what extent can MWI processes and their control on eruption source conditions be quantitatively
140 linked to the observable thickness or abundance of a surface water layer?
- 141 3. What are the critical relationships among water mass fraction at the eruption column source and mass
142 fluxes of SO₂, fine ash, and water to the stratosphere?

143 In this study, we address these questions using coupled conduit-plume 1D numerical simulations of
144 sustained, sub-Plinian to Plinian hydrovolcanic eruptions with rhyolitic magma compositions. We estimate
145 the sensitivity of the efficiency of stratospheric SO₂ injection to the presence of water layers up to 500 m
146 deep. The model approach consists of three coupled components (see Figures 1 and 2): (1) a 1D conduit
147 model simulating magma ascent and fragmentation (Hajimirza et al., 2019), which we modify with an
148 arbitrary hydrostatic pressure boundary condition applied at the vent; (2) a novel near-field “vent” model
149 simulating decompression of the initial gas-pyroclast mixture, water entrainment, and quench fragmentation
150 as a function of surface water depth Z_e ; and (3) a modified version of the 1D eruption column model
151 from Degruyter and Bonadonna (2012), incorporating a particle size distribution with sedimentation
152 following Girault et al. (2014). We focus our analysis on the main factors affecting overall column rise
153 (e.g. magma ascent and fragmentation, MWI and eruption column source parameters, and resulting column
154 gravitational stability, height, and sedimentation) and environmental conditions for vertical SO₂ transport
155 (e.g. temperature, water mass fluxes, and mass and surface area of ash particles). In considering only
156 column height, entrainment of water mass, and particle loss, we neglect a number of issues that will enter
157 into more complete future treatments of an SO₂ delivery efficiency: 1) a thermodynamic control in the

158 conduit on the SO₂ solubility behaviour below the fragmentation depth; 2) the coupled microphysics and
159 kinetics of SO₂ scavenging by ash particles sedimenting from the column and overlying umbrella cloud
160 through various mechanisms (Rose, 1977; Bursik et al., 1992; Durant et al., 2009; Niemeier et al., 2009;
161 Carazzo and Jellinek, 2012; Manzella et al., 2015); and 3) the kinetics of sulfur aerosol nucleation and
162 growth (Kremser et al., 2016) with or without ash (Zhu et al., 2020). As a consequence of ignoring the
163 above effects, our study does not address: (1) effects on the amount of sulfur gas exsolved from the melt
164 (e.g. possibly reduced SO₂ exsolution due to hydrostatic pressure); (2) scavenging and sedimentation of
165 sulfur species during eruption and column ascent (i.e. we assume 100% of exsolved sulfur is transported
166 along with the column and is delivered to the final buoyancy level or is carried downwards with column
167 collapse); (3) the formation, dispersal, atmospheric lifetime, and radiative effects of sulfate aerosols
168 following co-injection of SO₂, ash, and water into the spreading eruption cloud. However, we discuss the
169 implications of co-injection of SO₂ with enhanced quantities of fine ash and water in Section 4.

2 METHODS

2.1 A Model of Sustained, Explosive Hydrovolcanism

170 Our focus is on sustained eruptions with sufficient momentum and buoyancy fluxes at the column source,
171 which we will define carefully below, to inject SO₂ into the stratosphere. Consequently we restrict our
172 analysis and modelling efforts to a class of powerful eruptions driven by magmatic vesiculation and
173 fragmentation in the conduit, where the gas-pyroclast mixture is modified by the entrainment and mixing
174 of external water that is primarily confined to the surface environment. This approach is motivated by
175 observations of pyroclast textures and particle size distributions from several hydrovolcanic eruptions,
176 including the 25 ka Oruanui and 1.8 ka Taupo eruptions, New Zealand (Self and Sparks, 1978; Wilson
177 and Walker, 1985), the 2500 BP Hverfjall Fires eruption (Liu et al., 2017), the 10th century eruption of
178 Eldgjá Volcano, Iceland (Moreland, 2017; Moreland et al., 2019), the 1875 eruption of Askja Volcano,
179 Iceland (Self and Sparks, 1978; Carey et al., 2009), and the 2011 eruption of Grímsvötn (Liu et al., 2015).
180 Whereas airfall deposits from dry phases of each of these eruptions have total PSDs and porosities typical
181 of Plinian events (Cas and Wright, 1987; Fisher and Schmincke, 2012), PSDs from wet eruption phases are
182 relatively fines-enriched. Observations of PSDs, pyroclast textures and vesicularities from these events lead
183 to the interpretation that melts fragmenting inside the conduit produce approximately similar PSDs that
184 are modified, in turn, through a “secondary” episode of fragmentation related to the quenching of the gas-
185 pyroclast mixture within overlying surface water layers (Liu, 2016; Aravena et al., 2018; Moreland et al.,
186 2019; Houghton and Carey, 2019). In principle, PSDs can also be modified through effects of groundwater
187 infiltration through the conduit walls, which can be enhanced with an overlying water layer as has been
188 suggested on the basis of field observations (Barberi et al., 1989; Houghton and Carey, 2019). However,
189 numerical simulations of Aravena et al. (2018) demonstrate that the extent of groundwater infiltration from
190 100-300 m-thick aquifers perched at or above the fragmentation depth depends on the magma mass eruption
191 rate (MER). Crucially, for $MER \gtrsim 5 \times 10^6$ kg / s, which is typical of the sustained explosive eruptions
192 and rhyolitic magma composition on which we focus, Aravena et al. (2018, Supplemental Material) find
193 that water infiltration into the conduit flow is largely restricted to less than about 5 to 6 wt.% for rhyolitic
194 magmas. In addition, their calculations suggest that conduit failure or collapse is likely favored where
195 ingested water mass fractions in the conduit exceed about 5 wt%. Aravena et al. (2018) further suggest
196 this condition may be an explanation for why phreatomagmatic activity associated with direct interaction
197 of un-fragmented melt with external water is more commonly dominant in eruptions with relatively low
198 MER, a result consistent with field observations (Walker, 1981; Houghton and Wilson, 1989; Cole et al.,
199 1995; Moreland et al., 2019; Houghton and Carey, 2019); for completeness we include eruptions with

201 MER as low as 5.5×10^5 kg/s, however we note that the above assumptions are likely less valid for these
202 low values.

203 Taking these observations and inferences into consideration in our modelling approach, we assume
204 that secondary fragmentation from MWI is driven predominantly by quench fragmentation (also known
205 as thermal granulation) (van Otterloo et al., 2015), as opposed to phreatomagmatic fragmentation by
206 molten-fuel-coolant interaction (Büttner et al., 2002). Following Jones et al. (2019) and Hajimirza et al. (In
207 press), the MWI model is based on the physics of water entrainment for a subaqueous jet as well as the
208 energetics of quench fragmentation. We do not consider classes of hydrovolcanic events driven primarily
209 by episodic molten-fuel coolant interactions (Wohletz et al., 2013; Houghton et al., 2015; Zimanowski
210 et al., 2015). We focus on eruptive phases in a sub-Plinian to Plinian to Phreatoplinian continuum under
211 established classification schemes (Walker, 1973; Self and Sparks, 1978). Furthermore, we model only
212 the sustained, steady-state phases of these events. Figure 2 shows a conceptual overview of the problem
213 definition and model setup in the near-vent region where an erupting jet emerges from the volcanic vent
214 and encounters a shallow (≤ 500 m) water layer (see Supplementary Figure S1 for a detailed overview
215 of the model internal workflow). On the basis of arguments from Aravena et al. (2018) for eruptions
216 with $\text{MER} \gtrsim 10^6$ kg/s, we do not consider water infiltration into the shallow conduit and assume MWI
217 occurs only within the overlying water layer. We include further discussion on this assumption and sample
218 calculations of the effects of water infiltration into the conduit in Section 4.4. This study is not an exhaustive
219 coverage over the full range of hydrovolcanic events, but rather is a first attempt at characterizing the broad
220 behavior of an important end-member of sustained hydrovolcanic eruption for which (a) primary magmatic
221 fragmentation is the dominant driving mechanism, (b) fuel-coolant interactions play at most a minor role in
222 the momentum and energy budgets, and (c) substantial stratospheric injection of SO_2 is a likely outcome.

223 2.2 1D Conduit Model

224 We use the one dimensional conduit model of Hajimirza et al. (2021) and integrate flow properties over
225 the cross-sectional area of the conduit. We assume a vertical cylindrical conduit with radius a_c and depth z
226 (for a complete description of mathematical symbols and nomenclature, see Table 1). The conduit radius is
227 fixed except near the surface, where flaring near the vent is possible to enforce mass conservation for a
228 choked flow at the vent (Gonnermann and Manga, 2013). We assume the flow is steady - i.e. the duration
229 of magma ascent is much shorter than the duration of Plinian eruptions (Mastin and Ghiorso, 2000). The
230 magma is a mixture of rhyolitic melt (76% SiO_2) and H_2O bubbles that exsolve continuously during
231 ascent because H_2O solubility is proportional to the square root of pressure. We also assume crystals
232 are only present as a dilute suspension of uniformly distributed sub-micron scale microphenocrysts that
233 enable a 1D approximation of heterogeneous bubble nucleation (Shea, 2017). This simplified picture
234 also leads to assumptions that the presence of microphenocrysts has negligible effects on magma density
235 and rheology. Thus, below the level of fragmentation we define magma as a mixture of silicate melt and
236 H_2O bubbles, and we assume the melt phase is incompressible (Massol and Koyaguchi, 2005). The flow
237 transitions discontinuously above the level of fragmentation to a dilute mixture of continuous H_2O vapor
238 with suspended fragments of vesicular pyroclasts. For model purposes, we treat water as the only magmatic
239 volatile: SO_2 (and other gases) do not contribute to the thermodynamic state of the magma and are carried
240 within the mixture passively. We use the term "gas" interchangeably with water vapor throughout unless
241 otherwise stated.

242 We assume the relative velocity between the melt/pyroclast and bubble/gas phases to be negligible
243 below and above the fragmentation level. Below fragmentation, bubbles are entrained in the very viscous
244 melt and the magma rises as a foam (e.g. Mastin and Ghiorso, 2000; Gonnermann and Manga, 2007).

245 Above fragmentation, a real volcanic flow will experience complex phenomena including solid/gas phase
 246 separation and sound wave dispersion, as well as buoyancy effects including the excitation of compaction
 247 and porosity waves (e.g. Bercovici and Michaut, 2010; Michaut et al., 2013). Such dynamics are important
 248 for degassing and can modify fragmentation processes in one-dimensional conduit models. However,
 249 their inclusion is practically challenging and the effect of resulting fluctuations in MER on the height
 250 and gravitational stability of steady-state plumes is ultimately small in comparison to controls arising
 251 through parameterizations for water and air entrainment. For simplicity and to retain a focus on the effect
 252 of entrainment and MWI on plume height and SO₂ delivery to the stratosphere, we neglect these dynamics
 253 and apply the common pseudo-gas approximation for fully-coupled gas and particle flow (Wilson et al.,
 254 1980; Mastin and Ghiorso, 2000). The properties of the magma mixture (melt and bubbles or gas and
 255 pyroclasts) are, consequently, the volumetric average of the two phases. We also assume the conduit flow
 256 to be isothermal (Colucci et al., 2014) because heat loss to conduit walls is negligible over the time scale of
 257 rise through the depth z (Mastin and Ghiorso, 2000). The latent heat flux consumed through the exsolution
 258 of a H₂O with magma ascent helps to enforce this condition, although the effect is very small.

259 With these assumptions and simplifications, conservation of mass and momentum for the ascending
 260 magma are (Wilson et al., 1980; Mastin and Ghiorso, 2000)

$$\frac{\partial(\rho u A)}{\partial z} = 0, \quad (1)$$

261 and

$$\rho u \frac{\partial u}{\partial z} = -\frac{\partial p}{\partial z} - \rho g - F_{\text{fric}}, \quad (2)$$

262 respectively. Here u is magma ascent rate and $A = \pi a_c^2$ is the conduit cross sectional area. The bulk magma
 263 density is

$$\rho = \chi_v \rho_v + (1 - \chi_v) \rho_m, \quad (3)$$

264 where χ_v is the volume fraction of bubbles, and ρ_v and $\rho_m = 2400 \text{ kg/m}^3$ are gas and melt densities
 265 respectively. The frictional pressure loss $F_{\text{fric}} = \rho u^2 f / a_c$ where f is a friction factor. Below the
 266 fragmentation depth $f = 16/Re + f_0$ and above the fragmentation depth $f = f_0$. Here, the Reynolds
 267 number $Re = 2\rho u a / \eta$, where η is the viscosity of the mixture. The reference friction factor $f_0 = 0.0025$
 268 depends on the conduit wall roughness (Mastin and Ghiorso, 2000). By substituting Equation (1) into (2)
 269 and defining the isothermal mixture sound speed

$$\left(\frac{\partial \rho}{\partial p} \right)_{T_0} = c^2, \quad (4)$$

270 we obtain (Gonnermann and Manga, 2013; Hajimirza et al., 2021)

$$-\frac{\partial p}{\partial z} = \frac{\rho g + F_{\text{fric}} - \frac{\rho u^2}{A} \frac{\partial A}{\partial z}}{1 - M^2}, \quad (5)$$

271 where the Mach number $M = u/c$. Below the fragmentation depth the sound speed of the mixture
 272 $c = (K/\rho)^{1/2}$, where K is the bulk modulus of the mixture given by:

$$\frac{1}{K} = \frac{\chi_v}{K_v} + \frac{1 - \chi_v}{K_m}. \quad (6)$$

273 Above the fragmentation depth, the bulk modulus of the gas phase K_v is calculated for the mixture
 274 temperature from the equation of state for water (Holloway, 1977).

275 The conduit model includes treatments for water vapor exsolution from the melt and subsequent bubble
 276 growth from Hajimirza et al. (2021). At a given depth below fragmentation, heterogeneous bubble
 277 nucleation on crystal nanolites occurs with a specified critical supersaturation, and growth is by the
 278 diffusion of water from the melt. Above the fragmentation depth the bubble volume and number density are
 279 fixed, although vapor can continue to exsolve and escape from pyroclasts into the surrounding free vapor
 280 by permeable flow. We employ a fixed porosity threshold of 75% as a fragmentation condition, which is
 281 consistent with measurements and analyses of pumice permeabilities and vesicle size distributions that
 282 show that PSDs follow power laws comparable to those of pore-scale microstructures in erupted pumice
 283 (Kaminski and Jaupart, 1998; Rust and Cashman, 2011). We consequently do not fix a PSD in the conduit
 284 and assume only that fragmentation proceeds to small enough length scales such that gas escape from
 285 connected pores in the entrained pyroclasts is sufficient to ensure that pore-scale pressures are equivalent to
 286 the free gas in the conduit at the vent (Rust and Cashman, 2011).

287 Assuming negligible gas escape or water infiltration through conduit walls, the primary effect of overlying
 288 surface water or ice is to modify the pressure boundary condition at the volcanic vent. Above magmatic
 289 fragmentation, the gas-pyroclast mixture fluidizes, accelerates, and decompresses towards the conduit exit.
 290 If the flow speed remains below the mixture sound speed c , then the vent exit pressure p_c must balance the
 291 ambient pressure above the vent p_e , which is determined by water depth:

$$p_e = \rho_e g Z_e + p_{atmo}. \quad (7)$$

292 Here ρ_e is the density of external water and p_{atmo} is the atmospheric pressure at the water surface. However,
 293 if $M \rightarrow 1$, the flow becomes choked, which causes the flow at vent to be overpressured relative to ambient
 294 (Gonnermann and Manga, 2013). As a metric for vent overpressure, we introduce the vent overpressure
 295 ratio $\beta = p_c/p_e$. To enforce mass conservation for choked flow, either choking must occur at the vent exit
 296 of a fixed radius conduit or the conduit radius must flare accordingly (Gonnermann and Manga, 2013). The
 297 conduit modelling approach is therefore to seek solutions where the pressure in the conduit flow matches
 298 the surface pressure boundary condition (i.e. $\beta \approx 1$), or for which the conduit is choked at (no flaring) or
 299 near (with flaring) the vent (i.e. $\beta \gtrsim 1$, $M \approx 1$).

300 To gain insight into how an ascending magma responds to changes in hydrostatic pressure related to
 301 loading by overlying layers of water or ice, it is instructive to compare solutions for eruptions with and
 302 without external water, with other independent parameters fixed. To this end we choose a fixed conduit
 303 depth $z = 6$ km, an initial magmatic temperature $T_0 = 1123.15$ K and a maximal (unexsolved) magmatic
 304 water content corresponding to saturation as determined with the method of Liu et al. (2005). We then
 305 use an iterative search to find conduit parameters that satisfy the pressure-balanced or choked conditions.
 306 We first allow conduit radius to vary to obtain solutions for a “dry” or subaerial vent where no external
 307 water is present and the ambient pressure above the vent is equal to atmospheric ($Z_e = 0$). Subaerial vent
 308 simulations were run and suitable conduit radii obtained for a range of “control” MER $10^{5.5} \leq Q_0 \leq 10^9$
 309 kg/s, and we refer to these subaerial vent scenarios as “control” simulations hereafter. For control scenarios,
 310 we seek specifically solutions where choking occurs at the vent exit and thus no conduit flaring is required.
 311 This calculation provides a reference conduit radius to use in scenarios with a water layer present above
 312 the vent, with water depths $0 < Z_e \leq 500$ m. For these hydrovolcanic cases, we then fix the conduit
 313 radius to that of the control scenario and find an adjusted conduit MER q_c such that the surface pressure

314 and/or choking boundary conditions are again satisfied. All values of MER referred to herein (i.e. Q_0 , q_c)
 315 indicate magmatic mass fluxes in the conduit (i.e. excluding external water). See Supplementary Figure S2
 316 for a visualization of the search process for conduit radius and MER in control and hydrovolcanic cases,
 317 respectively. Although we choose MER as our adjusted parameter, other parameter choices are possible,
 318 such as the excess pressure of the magma reservoir at the base of the conduit or modification of the vent
 319 geometry. To make clear our approach and the consequences of our approximations and simplifications,
 320 see Section 3.1 for example conduit model results.

321 2.3 Vent and MWI Model

322 2.3.1 Initial Particle Size Distribution

323 The model PSD is specified explicitly at the vent ($z = 0$) using output from the conduit model. We define
 324 an initial power-law PSD following Kaminski and Jaupart (1998) and Girault et al. (2014), over the particle
 325 size range $-10 \leq \phi_i \leq 8$. The number of particles N_i at size ϕ_i is given by

$$N_i = 2^{\log_2(N_0) + D_0 \phi_i}, \quad (8)$$

where D_0 is the power-law exponent, N_0 is an arbitrary normalization constant, and subscript i indicates a
 particle size bin. We choose a default value of $D_0 = 2.9$. Each size class is assigned an effective porosity
 value χ_i on the basis of an effective particle radius according to

$$\chi_i = \chi_0, \quad r_i \geq r_{c1}, \quad (9)$$

$$\chi_i = \chi_0(1 - r_{c2}/r_i), \quad r_{c2} \leq r_i \leq r_{c1}, \quad (10)$$

$$\chi_i = 0, \quad r < r_{c2}. \quad (11)$$

326 Here, $\chi_0 = 0.75$ is the porosity threshold for fragmentation, r_i is the particle radius for bin i , $r_{c1} = 10^{-2}$ m
 327 and $r_{c2} = 10^{-4}$ m. Particles of sufficiently small size have, thus, no effective porosity and densities equal
 328 to that of the pure melt phase ($\rho_{s,i} = \rho_m$). By contrast, the density of larger particles is a strong function
 329 of porosity and bubble gas density (Kaminski and Jaupart, 1998). This approach leads to expressions for
 330 particle mass fraction in each size bin, $n_{s,i}$, and the bubble gas mass fraction of each size bin, $n_{b,i}$:

$$\rho_{s,i} = (1 - \chi_i)\rho_m + \chi_i\rho_v, \quad (12)$$

331

$$n_{s,i} = \frac{N_i r_i^3 \rho_{s,i}}{N_\phi \sum_{i=1} (N_i r_i^3 \rho_{s,i})}, \quad (13)$$

332

$$n_{b,i} = \frac{\frac{\rho_v \chi_i}{\rho_m (1 - \chi_i)}}{\left(1 + \frac{\rho_v \chi_i}{\rho_m (1 - \chi_i)}\right)}, \quad (14)$$

333 where subscript s denotes the bulk ‘‘solids’’ phase (melt plus bubbles) and N_ϕ is the number of particle size
 334 bins. Figure 3d shows the initial PSD for $D = 2.9$, accounting for particle density as a function of porosity
 335 (light gray line and square symbols).

336 2.3.2 Vent Decompression

337 Figure 2 highlights the geometry and relevant length scales for the MWI model. For an overpressured jet
 338 in the near-vent region with $M \geq 1$ (e.g Ogden et al., 2008), we assume that mixing of the gas-pyroclast

339 mixture with external water is negligible over a “decompression length scale” L_d where expanding
 340 gas prevents pyroclasts inside the jet from interacting with external water (e.g. Kokelaar, 1986). Our
 341 decompression model therefore assumes that turbulent entrainment and mixing of external water begins
 342 at heights above L_d . For L_d , we use a modified form of the free decompression condition of Woods and
 343 Bower (1995) to find the height at which the jet gas pressure plus dynamic pressure is equivalent to external
 344 water hydrostatic pressure:

$$p_d + \frac{u_d^2 \rho_d}{2} = \rho_e g (Z_e - L_d) + p_{atmo}, \quad (15)$$

where p is pressure, u_d is the speed after decompression, and ρ is density. Subscripts d and e denote properties of the jet mixture after “decompression” and of “external” water, respectively. Assuming the decompression speed is approximately the mixture sound speed (i.e., $M = 1$ at the expanding shock front) (Ogden et al., 2008) and using the dusty-gas approximation (Woods and Bower, 1995),

$$u_d \approx c_d \approx c_{v,d} \sqrt{\frac{\rho_{v,d}}{\rho_d \chi_{v,d}}} \quad (16)$$

$$= \sqrt{\frac{\rho_v}{\rho_d \chi_{v,d}} \frac{\gamma P_d}{\rho_v}} \quad (17)$$

$$\approx \sqrt{\frac{\gamma P_d}{\rho_d}}, \quad (18)$$

345 where subscript v denotes the “vapor” phase, the free gas volume fraction $\chi_v \approx 1$, and γ is the ratio of
 346 specific heats for the vapor phase. Substituting Equation 18 into Equation 15 gives

$$p_d = \frac{p_e(L_d)}{1 + \frac{\gamma}{2}}. \quad (19)$$

347 Assuming that the mixture volume is approximately conserved, the decompression length L_d is proportional
 348 to the change in jet radius with decompression:

$$L_d = 2\Delta a = 2(a_d - a_c), \quad (20)$$

349 where

$$a_d = \left(\frac{\rho_c u_c a_c^2}{\rho_d c_d} \right)^{1/2}, \quad (21)$$

350 and

$$\rho_d = \left(\frac{1 - n_v}{\rho_s} + \frac{n_v}{\rho_{v,d}} \right)^{-1}. \quad (22)$$

351 Here n_v is the jet gas mass fraction, and the subscript c indicates properties in the “conduit” prior to
 352 decompression. Momentum and energy are not perfectly conserved after decompression in this formulation
 353 as they are in Woods and Bower (1995), because the radially averaged decompression velocity is taken to
 354 be the mixture sound speed. However, this approach is consistent with the results of numerical simulations
 355 (e.g. Ogden et al., 2008), where excess energy is dissipated via shock formation and related effects of
 356 supersonic flow, and radially average velocities after decompression are close to sonic. These equations
 357 give a decompression length approximately similar to the Mach disk height relation of Ogden et al. (2008),
 358 (see Supplementary Figure S3 for a comparison), but with the difference that $L_d \rightarrow 0$ for $\beta \lesssim 1$. This

359 is an important distinction since the formal definition of L_d in our model is the height at which the jet
 360 overpressure is sufficiently small that turbulent mixing and entrainment can begin. For a pressure-balanced
 361 jet ($\beta = 1$), this critical height should be immediately above the vent. We note, however, that due to the
 362 rapid pressure change with height in the water column, the mixture will continue to expand and decompress,
 363 such that the static estimate of L_d used here is likely a lower bound.

364 2.3.3 Water Entrainment and MWI Model

365 The mixing of water, steam, pyroclasts, and lithic debris in the vent region in explosive hydrovolcanic
 366 eruptions is complex and may involve effects of shocks, supersonic flow, film boiling, and multiple
 367 fragmentation mechanisms (Wohletz et al., 2013; Houghton and Carey, 2015; van Otterloo et al., 2015) that
 368 introduce inherently time-dependent and three-dimensional mechanisms for entrainment and mechanical
 369 stirring that are not captured in a one-dimensional steady-state integral model. However, following extensive
 370 studies of entrainment and mixing into turbulent plumes (Morton et al., 1956; Linden, 1979; Turner, 1986),
 371 a recent complementary analysis of water entrainment into supersonic, submerged gas jets (Zhang et al.,
 372 2020) and studies of the bulk energetics of interactions between hot pyroclasts and water (Dufek et al.,
 373 2007; Mastin, 2007a; Schmid et al., 2010; Sonder et al., 2011; Dürig et al., 2012; Woodcock et al., 2012;
 374 Moitra et al., 2020) we can parameterize these processes to explore effects on total budgets for mass,
 375 energy, and buoyancy. Following Morton et al. (1956); Kaminski et al. (2005); Carazzo et al. (2008); Zhang
 376 et al. (2020); Hajimirza et al. (In press), we will relate the radial entrainment speed of water or atmosphere
 377 to the local rise speed of a jet and prescribe resulting velocity, pressure and temperature fields. We assume
 378 the rate of mixing and heat transfer between solid pyroclasts and entrained water to be sufficiently fast
 379 that all phases are well-mixed and at equal temperature inside the jet over the timescale of rise through the
 380 water column. We discuss consequences of this assumption further in Section 4.

381 We initialize the water entrainment model at height L_d above the vent. Initial conditions for jet velocity,
 382 radius, and density are determined after decompression by balancing jet gas pressure with hydrostatic
 383 pressure at L_d . Other parameters such as gas mass fraction and temperature are obtained from values at
 384 the top of the conduit model, while the PSD and pyroclast porosity and density are determined according
 385 to Section 2.3.1 above. An iterative MATLAB solver integrates solutions to the differential equations for
 386 water and particle mass, bulk momentum and energy, and PSD mass fractions from the decompression
 387 height to the water surface. The physical properties of entrained water are calculated using the International
 388 Association for the Properties of Water and Steam 1995 formulation (Junglas, 2009). To capture the
 389 evolution with height of the mixture energy (enthalpy plus average vertical kinetic and gravitational
 390 potential energy), we follow a similar approach to Mastin (2007b). The initial enthalpy of the solid phase
 391 at the vent surface h_{s0} is determined from a weighted combination of the enthalpy of exsolved gas bubbles
 392 and the specific heat of the melt phase:

$$h_{s0} = h_b(p_b, T_0) \sum_{i=1}^{N_\phi} n_{s,i} n_{b,i} + C_m (T_0 - T_{ref}) \sum_{i=1}^{N_\phi} (1 - n_{b,i}) n_{s,i}. \quad (23)$$

393 Here $h_b(p_b, T_0)$ is bubble gas enthalpy as a function of pressure and temperature, $C_m = 1250 \text{ J/(kg K)}$
 394 is the melt heat capacity (assumed constant), and $T_{ref} = 274.15 \text{ K}$ is a reference temperature. The total
 395 mixture enthalpy, h is then

$$h = n_w h_w(p, T) + (1 - n_w) h_s, \quad (24)$$

396 where n_w and h_w are the mass fraction and enthalpy of water (gas and liquid) within the jet mixture. At the
397 decompression length, the total power supplied by the jet is

$$\dot{E}_0 = q_c(h_0 + g'L_d + \frac{u_d^2}{2}), \quad (25)$$

398 where q_c is the conduit MER and $g' = g(\rho - \rho_e)/\rho_e$ is the reduced gravity, and the dot notation over E
399 indicates the time derivative of the system's energy at decompression length L_d .

400 From an initial value T_0 , the bulk temperature of the jet mixture T is calculated at each solver step
401 following Mastin (2007b). Specifically, the enthalpy at each step is compared with two values: the enthalpy
402 h_{vap} that the mixture would have at the water saturation temperature assuming 100% steam (dryness
403 fraction $x_v = 1$), and h_{liq} , where the water phase is 100% liquid ($x_v = 0$). For $h > h_{vap}$, the mixture
404 temperature is found using an iterative approach to match the known enthalpy value h . For $h_{liq} < h < h_{vap}$,
405 $T = T_{sat}$ and $x_v = (h - h_{liq})/(h_{vap} - h_{liq})$. We employ a stop condition as dryness fraction reaches
406 $x_{v,crit} = 0.02$. This condition is justified physically because as the jet water fraction becomes mostly liquid
407 with $x_v \rightarrow 0$, the resulting high-density jets always collapse almost immediately after breaching the water
408 surface and are therefore ineffectual at injecting SO_2 into the stratosphere. Conceptually, this condition is
409 equivalent to the case where *at most* only minor quantities of steam breach the water surface, potentially
410 generating steam plumes but carrying negligible quantities of volcanic ash or other volatiles (e.g. Cahalan
411 and Dufek, 2021). We refer to the above ultra-high water fraction scenarios as the ‘‘steam plume’’ regime
412 hereafter. For greater water depths still, the gas jet would entirely condense and fail to breach the water
413 surface (Cahalan and Dufek, 2021). Furthermore, as the vapor fraction approaches zero, steep gradients in
414 density significantly increase problem stiffness and computation time, and we thus discard these results
415 and do not integrate further.

416 Entrainment of ambient fluid into a jet or plume is driven by both radial pressure variations arising from
417 the relatively fast rise of the jet and local shear across the jet-water interface (see Figure 1). Entrainment
418 parameterizations in integral plume models typically assume that the rate of radial inflow of ambient fluid
419 v_ε at any height is proportional to the upflow speed (Morton et al., 1956):

$$v_\varepsilon = \alpha u, \quad (26)$$

420 where α is an entrainment coefficient of order 0.1. Here we employ a variable entrainment coefficient
421 following Kaminski et al. (2005); Carazzo et al. (2008):

$$\alpha = 0.0675 + (1 - \frac{1}{A})\text{Ri} + \frac{a}{2} \frac{d}{dz} \ln(A), \quad (27)$$

422 where

$$\text{Ri} = \frac{g'a}{u^2} \quad (28)$$

423 is the local Richardson number that expresses the balance between the momentum and stabilizing buoyancy
424 fluxes at a given height. The shape function $A = A(z)$ depends on the diameter of the jet and Ri at
425 $z = 0$. This well-established hypothesis for ambient fluid entrainment is, however, strictly valid only where
426 turbulence is fully developed. This picture assumes that there is a direct momentum exchange between
427 large entraining eddies that form plume edges and a full spectrum of turbulent overturning motions that
428 mix momentum, heat and mass across the plume radius down to spatial scales limited by either molecular

429 diffusion or dissipation by very fine ash (Lherm and Jellinek, 2019). In general, this condition is established
 430 over heights of roughly 5 to 10 vent diameters (i.e. the vent near-field, see also Figure 2) and corresponds to
 431 a transition from flow as a jet governed by the momentum flux delivered at L_d to flow as a buoyant plume
 432 driven by a balance between buoyancy and inertial forces (Carazzo et al., 2006; Saffaraval and Solovitz,
 433 2012). A key issue for the character and magnitude of effects related to MWI is whether and where in the
 434 water layer this transition occurs such that water entrainment is fully established.

435 To constrain this transition height relative to L_D we follow an approach developed in Kotsovinos (2000)
 436 to identify the dynamical ‘‘crossover height’’ L_X at which fully turbulent plume rise starts and above which
 437 Equation 26 holds. Below L_X , the flow evolves predominantly in response to the momentum flux supplied.
 438 In this regime, drag related to turbulent instabilities, accelerations, overturning motions and mixing is not
 439 established and on dimensional grounds the evolving height of the jet

$$h_{jet} \sim (\pi a_d^2 u_d)^{1/4} t_{jet}^{1/2}. \quad (29)$$

440 Above L_X , plume height predominantly governed by a balance between buoyancy and inertial forces is, by
 441 contrast,

$$h_{BI} \sim \left(\frac{g'q}{\pi a_d^2} \right)^{1/2} t_{BI}^{3/2}. \quad (30)$$

442 The transition height L_X occurs where $h_{jet} = h_{BI}$, which corresponds to where the characteristic time
 443 scale $t_{jet} = t_{BI}$. After algebra we obtain

$$L_X = \pi^{5/8} u_d^{3/4} \left(\frac{a_d^5 \rho_d}{g'q} \right)^{1/4}. \quad (31)$$

444 Starting from height $z = L_d$, we assume the thickness a_{mix} of a turbulent mixing layer at the jet boundary
 445 develops monotonically over distance L_X :

$$a_{mix} = a \frac{z - L_d}{L_X}; \quad a_{mix} \leq a, \quad (32)$$

446 above which the radial turbulent mixing is complete and the velocity profile is top-hat or Gaussian,
 447 consistent with the assumption of self-similar flow (Morton et al., 1956; Turner, 1986). We then obtain
 448 an effective entrainment coefficient, α_{eff} , by scaling the entrainment coefficient based on the volumetric
 449 growth of the mixing layer:

$$\alpha_{eff} = \alpha \frac{2a a_{mix} - a_{mix}^2}{a^2}. \quad (33)$$

450 Using a similar entrainment parameterization to Mastin (2007b) which accounts for the relative density
 451 difference of the ambient and entraining fluid, the rate of water entrainment into the jet is

$$\frac{dq_{w,e}}{dz} = 2\pi a \alpha_{eff} u \sqrt{\rho \rho_e}. \quad (34)$$

452 In a recent study of supersonic air jets intruding 1-400 m deep layers of water from below (Zhang
 453 et al., 2020) shows that entrainment and mixing is significantly augmented by buoyancy effects related
 454 to the rise of air through layers of relatively dense water. Their results suggest that this mechanism will
 455 dominate the mechanics of entrainment for water layer depths exceeding a few hundred meters. This

456 condition is presumably set by the height in the water column at which the overturn time of large entraining
 457 eddies related to the rise of buoyant air becomes less than the time scale for water ingestion through
 458 shear-induced turbulence (Equation 27). The extent to which this mechanism governs the evolution of
 459 rapidly expanding hot volcanic jets erupting through comparably thick layers of water is, however, unclear
 460 and particularly so where L_d is of the same order of magnitude as the water depth. For completeness, we
 461 compare results obtained from Equations 27 to 33 with complementary calculations assuming entrainment is
 462 partially governed through the buoyancy-driven ‘‘Rayleigh-Taylor’’ entrainment mode of Zhang et al. (2020).
 463 Specifically, we define an alternative α_{eff} as a weighted average of the shear-driven and Rayleigh-Taylor
 464 entrainment modes:

$$\alpha_{eff} = B\alpha + (1 - B)\alpha_{RT}, \quad (35)$$

465 where

$$\alpha_{RT} = 4\pi \frac{a_d}{q_c} a \sqrt{\frac{2\rho}{3} (3\sigma\rho_e\omega)^{1/2}}. \quad (36)$$

466 Here, α_{RT} is the Rayleigh-Taylor coefficient for buoyancy driven entrainment, B is a specified weighting
 467 determining the relative contributions of buoyancy effects and shear to the total water entrainment, σ is
 468 the surface tension at the water-steam interface, and $\omega \approx (0.3u)^2/(2\pi a)$ is the average radial acceleration
 469 of the interface (Zhang et al., 2020). The geometric constant of 0.3 is an approximate scaling for the
 470 magnitude of turbulent velocity fluctuations (Cerminara et al., 2016) and ensures that the radial momentum
 471 flux carried by the inflow is an order of magnitude smaller than the vertical momentum flux carried by
 472 the jet itself. This condition is required for the jet to remain intact and approximately conical, consistent
 473 with the results of (Zhang et al., 2020), and for the equations underlying the 1D plume model to hold
 474 (Morton et al., 1956). We compare the consequences of different entrainment modes for eruption behavior
 475 in Sections 3.2 and 4.1.

476 2.3.4 Quench Fragmentation Model

477 The process of quench fragmentation of pyroclastic particles of various size during MWI is complex.
 478 Driving thermal stresses and stress concentrations arising through interactions with cold water depend on
 479 the curvatures of the outer surfaces of pyroclasts, their porosity and surface area-to-volume ratio, and on
 480 the spatial distributions and rates of both surface cooling and film boiling. How to capture thoroughly these
 481 particle-scale effects and their consequences for the mean particle size distribution in an evolving volcanic
 482 jet mixture is unclear and remains a subject of vigorous research (e.g. Wohletz, 1983; Büttner et al., 2002,
 483 2006; Mastin, 2007a; Woodcock et al., 2012; Patel et al., 2013; Liu et al., 2015; van Otterloo et al., 2015;
 484 Fitch and Fagents, 2020; Dürig et al., 2020b; Moitra et al., 2020; Hajimirza et al., In press). However, with a
 485 specified magmatic heat flow at the vent, considerations of the surface energy consumed to generate fine ash
 486 fragments (Sonder et al., 2011), guided by published experiments along with observational constraints on
 487 the hydromagmatic evolution of particle sizes (Costa et al., 2016), provide a way forward that is appropriate
 488 for a 1D integral model. Figure 3 highlights the salient features of the fragmentation model, using the
 489 example of a single simulation with $q_c = 1.03 \times 10^8$ kg/s and $Z_e = 120$ m. Sonder et al. (2011) performed
 490 lab experiments submerging molten basalt into a fresh water tank to constrain the partitioning of thermal
 491 energy lost from the melt between that which is transferred from melt to heat external water and that which
 492 is consumed irreversibly through fracturing of the melt to generate new surface area and fine ash. At any
 493 height above the vent, the total power delivered to entrained external water from the melt is

$$\Delta\dot{E}_e = (1 - \zeta)\Delta\dot{E}_m, \quad (37)$$

494 and $\Delta\dot{E}_m$ is the rate of heat loss from the melt phase. The remaining heat loss from the melt i.e. $\zeta\Delta\dot{E}_m$ is
 495 the energy consumed by fragmentation. Note that we define fragmentation energy efficiency in the opposite
 496 sense to Sonder et al. (2011) such that $\zeta = 1 - \eta$, where η is as defined in that work. The parameter ζ is
 497 an empirical fragmentation energy efficiency that gives the fraction of thermal energy lost irreversibly to
 498 fragmenting pyroclasts to generate fine ash. Where thermal stresses related to cooling produce no fine ash,
 499 $\zeta = 0$ and $\Delta\dot{E}_e = \Delta\dot{E}_m$. Experimentally, Sonder et al. (2011) find $0.05 \lesssim \zeta \lesssim 0.2$ for thermal granulation
 500 processes, with typical values of ~ 0.1 .

501 Below, we use Equation 37 to define power transfer during each height step of the MWI model. In more
 502 detail, entrained water must thermally equilibrate with both pyroclasts and internal water already in the
 503 volcanic jet. With both sinks for thermal energy included, we recast Equation 37 to be the total power
 504 transferred to entrained water at each height step:

$$\Delta\dot{E}_e = (1 - \zeta)\Delta\dot{E}_m + \Delta\dot{E}_w, \quad (38)$$

505 where $\Delta\dot{E}_w$ is the power supplied for heating external water by heated water already in the volcanic jet.
 506 Although this energy sink is very small for typical magma water mass fractions of $\lesssim 5\%$ at the vent height,
 507 this contribution to the energy balance in Equation 38 evolves to be significant with height in the jet as a
 508 result of progressive water entrainment.

509 Neglecting a comparatively very small contribution from the specific heat of water trapped within the
 510 pores of pyroclasts, Equation 38 can be recast as an enthalpy change with water entrainment over a height
 511 step:

$$-\Delta q_{w,e}(h_{w,f} - h_e) = (1 - \zeta)q_s C_m (T_f - T) + q_w (h_{w,f} - h_w), \quad (39)$$

512 where $\Delta q_{w,e}$ is the mass flux of entrained water, $h_{w,f}$ is the final enthalpy of the water phase after thermal
 513 equilibration (i.e. where the jet gas and particles are well-mixed and at the same temperature), h_e is
 514 the external water enthalpy, q_w and h_w are the mass fluxes and enthalpy, respectively, of water already
 515 equilibrated thermally within the jet. In Equation 39, T_f and T are the unknown final mixture temperature
 516 and known initial mixture temperature for the current height step, respectively. To estimate heat transfer
 517 to the entrained water phase, we assume that the change in temperature after equilibration $T_f - T$ is
 518 sufficiently small at each step that the jet water heat capacity can be approximated as constant for the
 519 current step, such that

$$h_{w,f} = h_w + C_w (T_f - T), \quad (40)$$

520 where C_w is the water heat capacity at temperature T . Substituting 40 into 39 leads to

$$T_f = \frac{(1 - \zeta)q_s C_m T + q_w C_w T - \Delta q_{w,e}(h_w - C_w T - h_e)}{(\Delta q_{w,e} + q_w)C_w + (1 - \zeta)q_s C_m}. \quad (41)$$

521 T_f can then be used to estimate heat transfer to entrained water $\Delta h_w = h_{w,f} - h_e$, which is used along
 522 with ζ and the PSD to later calculate the specific fragmentation energy, ΔE_{ss} .

523 Since we assume that the energy consumption during quench fragmentation results from the generation
 524 of new surface area (Sonder et al., 2011; Dürig et al., 2012; Fitch and Fagents, 2020; Hajimirza et al., In
 525 press), we calculate the specific surface area at each particle bin size assuming spherical particle geometry:

$$S_i = \frac{3\Lambda}{\rho_i r_i}, \quad (42)$$

526 where Λ is a scaling parameter accounting for particle roughness, as true particle surface area can potentially
 527 exceed that of ideal spherical particles by up to two orders of magnitude (Fitch and Fagents, 2020). We
 528 take a default value $\Lambda = 10$, and discuss the effects of different choices for Λ in Sections 3.2 and 4. The
 529 total surface specific surface area for a given PSD is

$$S = \sum_{i=1}^{N_\phi} S_i n_{s,i}. \quad (43)$$

530 To simulate the evolution of the PSD by quench fragmentation, we prescribe a representative range
 531 of particle sizes produced by thermal granulation based on the fine mode of particle sizes for the
 532 phreatomagmatic phase C of the 1875 Askja eruption, as reported in Costa et al. (2016). The resulting
 533 “output” PSD, $n_{si,f}$, is a normal probability density function, in ϕ size units, with mean $\phi_\mu = 3.43$
 534 ($\sim 100 \mu\text{m}$) and standard deviation $\phi_\sigma = 1.46$, and is shown in Figure 3a (gray shaded region).

535 The “input” particle sizes (i.e. particles that fragment to produce the fine fraction) are defined according
 536 to the available surface area in the coarse fraction ($\phi < \phi_\mu$). We use the output mean, ϕ_μ as a fragmentation
 537 cutoff - particles of this size and smaller are assumed to not participate in quench fragmentation, but
 538 can participate in heat transfer to water. This allows the definition of an effective fragmentation energy
 539 efficiency as a function of particle size (see Figure 3a, black line),

$$\zeta_i = \begin{cases} \zeta \frac{1-n_{si,f}}{n_{s\phi_\mu,f}} & \phi_i < \phi_\mu \\ 0 & \phi_i \geq \phi_\mu, \end{cases} \quad (44)$$

540 where $n_{s\phi_\mu,f}$ is the mass fraction of the mean size bin in the output PSD. Fragmentation efficiency thus
 541 quickly reduces to zero as particle sizes approach the mean output size. In addition to the above particle
 542 size limitation on fragmentation, we also halt fragmentation once the bulk mixture passes below the glass
 543 transition temperature. We define the glass transition lower bound for a hydrous rhyolitic melt using an
 544 empirical fit to data from Dingwell (1998) (note that Equation 45 is a distinct equation from the empirical
 545 fit provided in that work):

$$T_g = 785.5 - 83.48 \log(c_{H_2O}), \quad (45)$$

546 where c_{H_2O} is the residual concentration (in wt.%) of H_2O still dissolved in the melt and obtained from the
 547 conduit model (see Figure 3b). Since the glass transition occurs over a range of temperatures (Giordano
 548 et al., 2005; van Otterloo et al., 2015), we apply the glass transition limit using a smooth-heaviside step
 549 function of temperature,

$$h_{sm} = \left\{ 1 + \exp \left[\frac{-6}{\Delta T_g} \left(T - \left(T_g + \frac{\Delta T_g}{2} \right) \right) \right] \right\}^{-1}, \quad (46)$$

550 where ΔT_g is the glass transition temperature range, with typical values of ~ 50 K (Giordano et al., 2005).
 551 Using h_{sm} to scale ζ with temperature (Figure 3c), Equation 44 becomes:

$$\zeta_i = h_{sm} \begin{cases} \zeta \frac{1-n_{si,f}}{n_{s\phi_\mu,f}} & \phi_i < \phi_\mu \\ 0 & \phi_i \geq \phi_\mu, \end{cases} \quad (47)$$

552 and the effective fragmentation energy efficiency for determining total fragmentation energy from the PSD
553 is

$$\zeta_{eff} = \sum_{i=1}^{N_\phi} (1 - n_{bi}) n_{s,i} \zeta_i. \quad (48)$$

554 Note that fracturing and fragmentation can in reality still occur once the bulk temperature cools below T_g ,
555 contrary to our assumption here. However, due primarily to a decrease in thermal expansion coefficient
556 below T_g (Bouhifd et al., 2015), we assume that thermal stresses below T_g are insufficient to cause
557 substantial further alteration to the PSD and magmatic energy budget (the PSD is considerably enriched
558 in fine ash already at external water mass fractions sufficient to cool below T_g , see Figure 3). See
559 Supplementary Material Section S3 and Supplementary Figure S4 for a discussion of the rationale for
560 Equations 46-48 based on thermal stress estimates. The PSD of the coarse particle fraction (i.e. particle
561 sizes that experience mass loss due to quench fragmentation), $n_{si,0}$, is calculated as proportional to available
562 particle surface area in each size bin, modified by the fragmentation efficiency (Figure 3a, gray lines):

$$n_{si,0} = \frac{\zeta_i S_i n_{s,i} (1 - n_{bi})}{N_\phi \sum_{i=1} \zeta_i S_i n_{s,i} (1 - n_{bi})}. \quad (49)$$

563 Finally, we define the specific fragmentation energy (per mass of pyroclasts in the jet)

$$\Delta E_{ss} = \frac{\zeta_{eff}}{1 - \zeta_{eff}} \frac{\Delta h_w}{q_s} \frac{dq_{w,e}}{dz}, \quad (50)$$

564 and the change in mass of the pyroclast fraction due to gas release from vesicles on fragmentation

$$\frac{dm_{w,fr}}{dz} = m_s \frac{\Delta E_{ss}}{S_f E_s} \left[\sum_{i=1}^{N_\phi} \frac{n_{bi} n_{s,i}}{1 - n_{bi}} - \sum_{i=1}^{N_\phi} \frac{n_{bi} \left(n_{s,i} + \frac{dw_{s,i}}{dz} \right)}{1 - n_{bi}} \right], \quad (51)$$

565 where we choose $E_s = 100 \text{ J/m}^2$ for the particle surface energy for fragmentation (Dürig et al., 2012). The
566 final system of differential equations for evolution of the PSD, and conservation of water mass, pyroclast
567 mass, momentum, and energy, are respectively

$$\frac{dn_{s,i}}{dz} = \frac{\Delta E_{ss}}{S_f E_s} (-n_{si,0} + n_{si,f}), \quad (52)$$

568

$$\frac{dq_w}{dz} = \frac{dq_{w,e}}{dz} + \frac{dq_{w,fr}}{dz}, \quad (53)$$

569

$$\frac{dq_s}{dz} = -\frac{dq_{w,fr}}{dz}, \quad (54)$$

570

$$\frac{d}{dz} (\rho u^2 a^2) = g(\rho_w - \rho) r^2, \quad (55)$$

571

$$\frac{d\dot{E}}{dz} = \frac{dq_{w,e}}{dz} (g'z + h_w) - q_s \Delta E_{ss}. \quad (56)$$

572 Figure 3d shows the evolution of the total PSD during water entrainment and quench fragmentation
 573 in the MWI stage of the model according to Equation 52. The coarse to mid-size fraction of particles
 574 ($-3 \lesssim \phi \lesssim 2$) of particles deplete fastest owing to the surface area dependence in Equation 49. For example
 575 results of the MWI model, see Section 3.2.

576 2.4 1D Plume Model

577 For jets that breach the water surface, conditions at $z = Z_e$ are taken as the source parameters for the
 578 integral plume model. We use the integral plume model of Degruyter and Bonadonna (2012), modified
 579 with the particle fallout parameterization of Girault et al. (2014) to simulate differences in sedimentation
 580 in the eruption column as a function of fine ash production. Figure 3e shows the total PSD evolution
 581 due to particle fallout in the eruption column for a PSD that has been fines-enriched during MWI. The
 582 conservation equations for mass of dry air, water vapor, liquid water, and particles are, respectively

$$\frac{d}{dz}(\rho_a u a^2 \chi_a) = 2v_\varepsilon a \rho_{a,e} \chi_{a,e}, \quad (57)$$

$$\frac{d}{dz}(\rho_v u a^2 \chi_v) = 2v_\varepsilon a \rho_{v,e} \chi_{v,e} - \lambda \rho_v a^2 \chi_v, \quad (58)$$

$$\frac{d}{dz}(\rho_l u a^2 \chi_l) = \lambda \rho_v a^2 \chi_v, \quad (59)$$

$$\frac{d}{dz}(\rho_{s,i} u a^2 \chi_{si}) = -\xi \frac{q_s n_{s,i} u \phi_{s,i}}{a u}, \quad (60)$$

586 where v_ε is the entrainment velocity, subscript a denotes properties for dry air, $\lambda = 10^{-2} \text{ s}^{-1}$ is a constant
 587 condensation rate (Glaze et al., 1997), $u_{\phi,i}$ are particle settling velocities following Bonadonna et al. (1998),
 588 and $\xi = 0.27$ is the particle fallout probability. The equations for vertical momentum and energy are,
 589 respectively:

$$\frac{d}{dz}(\rho u^2 a^2) = g(\rho_e - \rho) a^2 - w \frac{d(\rho u r^2)}{dz} + u \sum_{i=1}^{N_\phi} \frac{dq_{s,i}}{dz}, \quad (61)$$

$$\frac{d}{dz}(\rho C T u a^2) = C_e T_e \rho_e a u_\varepsilon - \rho u a^2 g + L \frac{d}{dz}(\rho_l u a^2 \phi_l) + C_s T \sum_{i=1}^{N_\phi} \frac{dq_{s,i}}{dz}, \quad (62)$$

591 where C_s and C_e are the heat capacities of particles and air, respectively, T_e is the ambient air temperature,
 592 and L is the latent heat of condensation of water vapor. Note that the plume model retains the capability
 593 for simulating cross-winds as in Degruyter and Bonadonna (2012), but we show here only the vertical
 594 component of the momentum equation as we do not consider wind effects (wind fields are set to zero
 595 in atmospheric profiles). For further details on the plume model, we refer the reader to Degruyter and
 596 Bonadonna (2012, 2013), and to Girault et al. (2014) for the particle fallout details.

597 2.5 Simulation Scenarios

598 The conduit, MWI, and plume models are solved in series, with the conduit model providing source
 599 conditions for the MWI model, and the MWI model, in turn, providing source conditions for the plume
 600 model. As described above, our model approach is to simulate eruptions across a parameter space with
 601 $10^{5.5} \leq Q_0 \leq 10^9 \text{ kg/s}$ and $0 \leq Z_e \leq 500 \text{ m}$. In Table 2 we define the *Reference* scenario which employs
 602 default values as described above for the various model parameters. Specifically, the *Reference* scenario
 603 uses a water entrainment scheme that includes both decompression and cross-over length scalings, and

604 default fragmentation parameters $\Lambda = 10$, $\zeta = 0.1$, $D = 2.9$. The atmospheric profile used in the *Reference*
 605 scenario is obtained from ERA reanalysis data for the 2011 eruption of Grímsvötn Volcano (Hersbach
 606 et al., 2020; Aubry et al., 2021a), and we use a vent altitude of 1700 m above sea level. Note that we are
 607 not attempting to reproduce precise conditions for that eruption, but rather use this as a representative
 608 environmental condition for a high-latitude subglacial or sublacustrine eruption. To explore the effects of
 609 various model assumptions and parameter choices, we carried out nine additional simulation scenarios in
 610 addition to the *Reference* scenario, with each varying a single model parameter and performed over the
 611 same parameter space for MER and water depth. The second scenario we define, *Low-Lat*, uses an ERA
 612 reanalysis atmospheric profile for the 2014 eruption of Tungurahua Volcano with vent altitude 0 m a.s.l. as
 613 a representative atmosphere for a low-latitude submarine setting, keeping other parameters the same as the
 614 *Reference* scenario (see Supplementary Figure S5 for a comparison of atmospheric profiles used in the
 615 *Reference* and *Low-Lat* scenarios). Additional scenarios are broadly categorized into those with differing
 616 water entrainment assumptions and those with different fragmentation parameters relative to the *Reference*
 617 scenario. Entrainment scenarios include those without one or both of the decompression and crossover
 618 length scalings (*No- L_d* , *No- L_X* , and *No- L_d -No- L_X*), and a scenario with the Rayleigh-Taylor entrainment
 619 scheme of Equation 35 (αRT). Additional fragmentation scenarios include one with a higher particle
 620 roughness (*High- Λ*), higher and lower fragmentation energy efficiencies (*High- ζ* and *Low- ζ*), and a higher
 621 initial PSD power-law exponent (*High- D*). We highlight the effects of different entrainment scenarios in
 622 Section 3.2, and discuss the consequences of different parameter choices for these scenarios in Section 4.

3 RESULTS

623 3.1 Conduit Flow: Effects of an External Water Layer

624 An external water layer modifies the hydrostatic pressure in the conduit, which affects water saturation
 625 and exsolution, and in turn, magma decompression rate and fragmentation conditions (Cas and Simmons,
 626 2018). In Figure 4, we compare conduit model output for control ($Z_e = 0$ m, red lines) and hydrovolcanic
 627 ($Z_e = 400$ m, blue lines) simulations for $Q_0 \sim 1.6 \times 10^8$ kg/s. In the dry scenario, gas exsolution begins
 628 with an initial bubble nucleation event at a depth of 5.5 km below the vent (panel (e)). Above the first
 629 nucleation event, gas exsolution continues, driving increasing magma buoyancy, ascent and decompression
 630 rates. A sharp increase in exsolution and bubble growth near $z = 1.3$ km drives the gas volume fraction
 631 above the fragmentation threshold of 75% (panel (d)). At this depth, fragmentation occurs and the flow
 632 becomes a fluidized mixture of gas and suspended pyroclasts. Above this fragmentation depth, the flow
 633 accelerates to the mixture sound speed near the vent and becomes choked (panel (b)). At the vent the
 634 choked flow has a significant overpressure with $\beta \approx 11$ (panel (a) inset), and erupts to form an explosively
 635 decompressing subaerial jet.

636 Consistent with previous studies of subaqueous eruptions, the higher hydrostatic pressure at the vent
 637 in the hydrovolcanic case results in less gas exsolution and bubble growth, and consequently a slower
 638 decompression rate in the ascending magma (Cas and Simmons, 2018). Slower exsolution also results in
 639 lower total gas exsolution from the magma, and lower gas volume fraction above fragmentation (panel (d)).
 640 Above the fragmentation depth in the wet scenario, both the reduced mixture buoyancy related to a lower
 641 fraction of free gas and the higher hydrostatic pressure contribute to a reduced acceleration of the mixture,
 642 and the flow is subsonic ($M \approx 0.5$, panel (b)) and pressure-balanced ($\beta \approx 1$, panel (a) inset) at the vent.
 643 For this water depth and MER, we consequently find no viable conduit solution where the vent is choked
 644 (see also Supplementary Figure S2 for conduit solution search details). Across all model scenarios (see
 645 Table 2), water depths sufficient to cause this pressure-balanced condition usually lead to a weak jet that
 646 does not breach the water surface and/or to a steam plume condition (see Section 3.3 and Figure 9 below).

647 Figure 5 shows select parameters of the conduit model output as a function of MER and water depth,
 648 including vent overpressure ratio (panel (a), color field and contours), Mach number at the vent (b), MER
 649 adjustment relative to control runs (c), magma decompression rate at fragmentation depth (d), fragmentation
 650 depth (e), and the weight percent of residual water content dissolved in the pyroclasts at vent level (f). For
 651 the control runs ($Z_e = 0$), the vent is always overpressured and choked, with $\beta \rightarrow 45$ for the largest values
 652 of MER. Overpressure declines rapidly with increasing water depth until choking at the vent is impossible
 653 and the gas-pyroclast mixture enters the water layer as a pressure balanced, subsonic jet (solid blue line in
 654 panels (a),(c),(d)). We find that the largest water depth for which choking is possible is typically equal to
 655 about 5 vent radii. For example, for $Q_0 = 10^7$ kg/s, conduit radius $a_c = 20$ m, and the choking threshold
 656 depth occurs at ~ 100 m, whereas this threshold increases to ~ 220 m for $Q_0 = 10^8$ kg/s and $a_c = 45.5$
 657 m. For depths greater than the choking limit, the Mach number falls off rapidly to values of 0.5 and 0.1
 658 for depths equal to about 10 and 30 vent radii, respectively. For sufficiently large water depths and small
 659 MER, we find no conduit solutions in which fragmentation occurs (blue region, panel (a) top-left). As
 660 introduced in Section 2.2, for hydrovolcanic runs we adjust the MER relative to control runs to match the
 661 vent boundary condition. Figure 5c shows the ratio of adjusted MER to control MER, q_c/Q_0 , which for
 662 control simulations is always equal to 1 by definition. The adjustment is minor (no more than about 10%)
 663 and positive in most cases where vent choking is maintained. For water depths greater than the choking
 664 threshold, q_c begins to decrease, reaching values as low as 20-30% of Q_0 for low MER and large water
 665 depths. This trend is, however, not universal: for low MER, a strong second nucleation event occurs near
 666 the fragmentation depth and leads to relatively larger values of released gas and consequently greater MER
 667 until water depths of about 150 to 200 m (panels (c) and (f), lower-left corner).

668 Figure 5d shows the peak magma decompression rate \dot{p} at the fragmentation depth. Where the choking
 669 condition holds, peak decompression rate ranges between about 4 and 7 MPa/s and varies with MER, but
 670 for all depths greater than about 5 vent radii, decompression rate decreases, falling to values well below
 671 3 MPa/s for depths greater than about 15 to 20 vent radii. The blue dashed line in panel (d) shows the
 672 maximum water depth for which peak bubble overpressure $\Delta p_b = p_b - p_m$ (i.e. the difference between
 673 the gas pressure inside bubbles and pressure in the ascending magma *at the fragmentation depth*) is equal
 674 to 5 MPa, which is an approximate low bound for the tensile strength of the magma (Cas and Simmons,
 675 2018). Our fragmentation criterion allows fragmentation regardless of peak decompression rate or bubble
 676 overpressures, so long as sufficient vapor exsolution occurs to reach a porosity of 75%. However, the
 677 decrease in both maximum decompression rate and maximum bubble overpressure with increasing water
 678 depth has important implications if alternative criteria for magma fragmentation are considered, which
 679 we discuss further in Section 4.3. Fragmentation depth (panel (e)) is governed by decompression and gas
 680 exsolution rates and decreases with both increasing MER and increasing hydrostatic pressure, reaching
 681 about 500 m at its shallowest for the largest values of MER and water depth. As shown in Figure 5f, we
 682 find that for $Q_0 \lesssim 3 \times 10^6$ kg/s and $Z_e \lesssim 150$ to 200 m, a second nucleation event in the conduit near
 683 fragmentation results in a notably higher total gas exsolution from pyroclasts (a difference of up to about
 684 0.5 wt%). Higher total gas exsolution increases the free gas mass fraction at the vent, which in turn slightly
 685 boosts vent overpressure and adjusted MER. Importantly for our results, enhanced gas exsolution alters the
 686 glass transition temperature according to Equation 45, with consequences for quench fragmentation during
 687 MWI that we discuss below.

688 3.2 MWI model and the effects of water entrainment

689 Figure 6 shows MWI model results for four simulation scenarios with different water entrainment
 690 parameterizations: the *Reference* scenario (blue) with scalings for both decompression length (L_d , equations
 691 15 to 20) and crossover length (L_X , equations 29 through 33), no crossover length scaling (*No- L_X* , red),

692 no decompression length ($No-L_d$, purple), and with the weighted Rayleigh-Taylor entrainment coefficient
 693 in Equations 35 and 36 (α_{RT} , light blue). In the simulation shown ($q_c = 1.03 \times 10^8$ kg/s, and $Z_e = 120$
 694 m), the jet in the *Reference* scenario begins entraining water after decompression at a height of about 55 m
 695 above the vent. In contrast to a sub-aerial jet, the gas jet is buoyant in sub-aqueous settings and accelerates
 696 towards the water surface (panel (a)). Bulk temperature (panel (b)) decreases with water entrainment,
 697 and bulk density (panel (c)) decreases from both an increase in the vapor mass fraction (panel (d), solid
 698 lines) and decompression as the jet moves upwards in the water column. New ash surface area is produced
 699 through quench fragmentation (panel (e)), proportional to the mass of water ingested. This process proceeds
 700 until the mixture cools below the glass transition at a height of about 105 m above the vent (marked with
 701 circle symbols in panels (b) and (e)), after which no additional ash surface area is generated. The effective
 702 entrainment coefficient (panel (f)), scaled by L_X (Equation 31), grows approximately linearly from an
 703 initial value of zero according to Equation 33, resulting in a continuous increase in the rate of water
 704 ingestion. In the $No-L_X$ scenario, the entrainment coefficient is equal to that given by Equation 27. Here,
 705 the entrained mass of water rises much more sharply with height and causes the mixture to reach the glass
 706 transition by around 10 m of above the decompression length L_D . Furthermore, in these calculations water
 707 vapor saturation is reached after only 25 m of rise. Above water saturation, the liquid water fraction in the
 708 jet increases rapidly with height (panel (d), dashed lines). The concomitant increase in density reduces
 709 jet acceleration relative to the *Reference*, until breach of the water surface occurs. In the $No-L_d$ scenario,
 710 the entrainment coefficient initiates at a value of zero as in the *Reference*, but entrainment begins from
 711 $z = 0$ rather than $z = L_d$. The crossover length $L_T = 230$ m is greater than water depth for this event, and
 712 consequently the entrainment rate increases over the full height of the water layer (see Equations 32, 33),
 713 reaching a larger maximum value at the water surface ($\alpha = 0.076$ versus $\alpha = 0.04$ in the *Reference*). The
 714 bulk mixture temperature for the $No-L_d$ scenario reaches the saturation temperature at a height of 80 m,
 715 and ultimately a similar total mass of entrained water to the $No-L_X$ scenario on reaching the water surface
 716 (about 45 wt.%). The α_{RT} scenario uses a weighted combination of entrainment coefficients driven by
 717 buoyancy and turbulent shear. Buoyancy-driven entrainment in Equation 36 is approximately proportional
 718 to the surface area to volume ratio of the plume, i.e. $\alpha_{RT} \propto a^2/q_c$. For the relatively large MER shown
 719 here, q_c dominates in the above ratio resulting in a low value of α_{RT} , and the weighted α_{eff} is consequently
 720 a middle value between the *Reference* and $No-L_X$ scenarios. We further discuss the consequences of these
 721 water entrainment scenarios in Sections 3.3 and 4.1.

722 For a specified fragmentation efficiency ζ , the production of ash surface area from quench fragmentation
 723 increases with the extent of water entrainment, which increases with water depth (see Equation 38). Quench
 724 fragmentation proceeds rapidly compared with the timescale for the jet to cross the water layer (Figures
 725 3d and 6e). In the model, the primary limit for fine ash production is, thus, the height at which water
 726 entrainment causes the mixture temperature to become less than the glass transition temperature. For
 727 $C_m = 1250$ J/(kg K) and $T_0 = 1123$ K, this condition is met where $n_e \gtrsim 0.12$. However, even with
 728 this imposed temperature limit for quench fragmentation, Figure 3d shows that the PSD is substantially
 729 enriched in fine ash for this mass fraction of entrained water. For an initial PSD exponent of $D = 2.9$
 730 (Figure 3d, light grey line), the mass fraction of ash particles less than $120 \mu\text{m}$ ($\phi \leq 3$) is about 45%, while
 731 it is 80% after the glass transition is passed (Figure 3d, black line). Therefore in the absence of the glass
 732 transition limit, coarse particles could be fully depleted. In Section 4 we further discuss the consequences
 733 of our choice of fragmentation model and the associated key parameters: initial PSD, particle roughness,
 734 fragmentation energy efficiency, and glass transition temperature.

735 3.3 Effects of the Water Layer on Column Rise

736 Figure 7 shows eruption column model results for two example simulations with $Q_0 = 10^7$ kg/s: a control
 737 simulation ($Z_e = 0$ m), and a hydrovolcanic case with $Z_e = 70$ m. Dashed grey lines show parameters
 738 of the ambient atmosphere. The control scenario (in red) inherits conditions directly from sub-aerial vent
 739 decompression: bulk density (panel (a)) is determined by the mass fractions of pyroclasts and magmatic
 740 vapor (shown in panels (e) and (f), respectively), velocity (panel (b)) is equal to the mixture sound speed,
 741 and the bulk temperature is equal to the initial value in the conduit (panel (d)). The jet cools rapidly with
 742 entrainment of ambient air and condensation of water vapor begins shortly above the vent, though the
 743 liquid mass fraction remains below 1% (panel (f), dashed lines). The jet becomes buoyant (density less
 744 than ambient atmosphere) within a few hundred meters of the vent, becomes negatively buoyant above the
 745 neutral buoyancy height of about 9 kilometers above the vent (Z_{nbl}), and rises to a maximum overshoot
 746 height Z_{max} of over 12 km. In contrast, the hydrovolcanic simulation emerges at the water vapor saturation
 747 temperature, $T_{sat} = 367K$, with a total water mass fraction of 46% (near the threshold for gravitational
 748 collapse). Acceleration through the water layer results in a higher initial velocity relative to the control
 749 simulation (see Figure 6a), and the high mass fraction of water vapor gives the initial jet a relatively low
 750 density. However, due to the low temperature and increasing density from condensation, the hydrovolcanic
 751 jet generates buoyancy much more slowly than in the control case, becoming buoyant relative to ambient 3
 752 km above the vent. The reduction in total buoyancy flux results in maximum height and neutral buoyancy
 753 level approximately 1.5 km and 700 m less than the control case, respectively.

754 To demonstrate behavior of the coupled system, Figure 8 shows values of controlling parameters in
 755 the conduit, vent, and column model components for *Reference* simulations with $Q_0 = 10^8$ kg/s and
 756 varying water depths $0 \leq Z_e \leq 300$ m. Figure 8a compares the eruption column maximum height and
 757 level of neutral buoyancy (in km above sea level) against tropopause and vent altitudes. Panels (b) through
 758 (e) highlight parameters of the conduit including adjusted MER q_c , fragmentation depth Z_{frag} , vent
 759 overpressure β , and vent Mach number M . Panels (f) through (i) show output of the MWI model. Panel (f)
 760 shows the scalings for decompression L_d and crossover length L_X , and panel (g) shows the maximum value
 761 of the effective entrainment coefficient over the height of the water layer (as determined by equations 27
 762 and 33, see Figure 6f). Panels (h) and (i) show jet radius and velocity, respectively, at two different heights:
 763 after decompression $z = L_d$ and at the water surface level $z = Z_e$ (water surface level also corresponds to
 764 the eruption column source height as shown in Figure 2). Finally, panels (j) and (k) show the water mass
 765 fractions (vapor and liquid) and temperature for the eruption column source (i.e. $z = Z_e$). In all panels
 766 in Figure 8, vertical dashed lines show the threshold water depths for four important behavior regimes:
 767 (1) the height at which water depth and decompression length are equivalent $L_d = Z_e$, (2) the water
 768 depth above which the subaerial eruption column collapses before reaching a level of neutral buoyancy,
 769 (3) transition at the vent between a pressure balanced jet at high Z_e and one that is overpressured and
 770 choked ($\beta \gtrsim 1.05$, $M \gtrsim 0.95$) at lower Z_e , and (4) the depth above which the water dryness fraction
 771 $x_v \lesssim .05$, where at most minor quantities of steam breach the water surface (the “steam plume” condition
 772 as introduced in Section 2.3.3). The decompression length L_d defines the lower limit for water entrainment
 773 to start, and decreases with increasing hydrostatic pressure. For water depths in excess of L_D (panel (f)),
 774 water begins to entrain and mix into the jet, whereas our decompression length scaling prevents water
 775 ingestion for shallower depths (panel (g)). As the water mass fraction increases above about 30%, the
 776 water saturation temperature is reached and the column source includes liquid water (panel (j)), increasing
 777 its density. Consequently, jet velocity (panel (i)) decreases for greater water depths, and combined with
 778 reduced heat content in the particle fraction to generate buoyancy (panel (k)), it becomes impossible
 779 for the jet to undergo a buoyancy reversal, and gravitational collapse occurs (panel (a)). Since the vent

780 maintains the choked and overpressured condition until depths greater than the collapse threshold, the
 781 collapse condition for the subaerial column is not significantly influenced by changes in conduit conditions
 782 with increasing water depth, and is primarily determined by the mass fraction of entrained external water.
 783 At the upper limit for water entrainment, once the water mass fraction reaches ~ 0.7 , the heat budget of the
 784 pyroclasts is largely exhausted and most of the plume water ($\gtrsim 95\%$ by mass) is in liquid form, resulting in
 785 steam plume conditions where the a dense pyroclast jet collapses within at most ~ 1 km above the water
 786 surface.

787 Figure 9a shows total plume water mass fraction at the base of the subaerial eruption column as a function
 788 of MER and water depth for the *Reference* scenario. For comparison, the vent radius is marked in purple.
 789 The hatched light gray region highlights conditions for which stable buoyant plumes form, whereas collapse
 790 occurs for all simulations outside this region. At slightly lower water depths than the collapse threshold
 791 and for $\text{MER} \gtrsim 10^6$ kg/s, buoyant plumes breach the tropopause (tropopause height $Z_{tp} \approx 8.6$ km a.s.l. for
 792 the high latitude atmosphere used in the *Reference* scenario). The critical conduit MER for stratospheric
 793 injection, Q_{crit} , is highly sensitive to water depth. For example, the MER required for a buoyant column to
 794 reach the tropopause for a water depth of 150 m is over 10 times that for a water depth of 50 m, and nearly
 795 100 times that for a subaerial vent. This is driven primarily by the shift of the column collapse condition
 796 with increasing water depth (see also Figure 10). A notable feature is that for $\text{MER} \gtrsim 10^{8.3}$, the column
 797 collapses for the control case with no external water, but becomes a buoyant column for entrained water
 798 mass fractions up to $\sim 30\%$. In addition, low MER eruptions are able to support higher mass fractions of
 799 external water without collapse (e.g. $n_w \approx 45\%$ for $q_c = 10^7$ kg/s versus $n_w \approx 35\%$ for $q_c = 10^8$ kg/s).
 800 The relative buoyancy of low MER columns is caused by more efficient entrainment of air at smaller jet
 801 radii, as well as entrainment of atmospheric humidity and condensation and latent heat release in the plume.
 802 We note that condensation of atmospheric moisture has a more significant impact on buoyancy for smaller
 803 MER in the condensation parameterization used here (Glaze et al., 1997; Aubry and Jellinek, 2018). The
 804 solid blue line in Figure 9a marks the threshold where weak steam plumes may form, or fail to breach
 805 the water surface entirely for greater depths still. In the *Reference* scenario, the steam plume threshold is
 806 approximately coincident with the water depth limit for choked and overpressured vents. This limiting
 807 condition is a consequence of greater entrainment efficiency near the choking limit; Since $L_d \rightarrow 0$ as
 808 $\beta \rightarrow 1$, and entrainment rate grows over the height of the water column until $z = L_d + L_X$, maximum
 809 water entrainment rates are favored for pressure-balanced jets. However, the choking and steam plume
 810 limits need not be coincident, as shown in Figure 9b.

811 Figure 9b shows the threshold water depths for failed plumes (dashed lines) and stratospheric injections,
 812 (solid lines), for a subset of the simulation scenarios (see Table 2). The black lines in panel (b) are for
 813 the *Reference* scenario with high latitude (Iceland) atmosphere (corresponding to the solid blue line for
 814 steam plumes and solid black line for stratospheric injection in panel (a)). Blue lines show the scenario
 815 for low latitude (Equador) atmosphere (*Low-Lat*). Neglecting the effects of wind, atmospheric humidity,
 816 stratification, and tropopause height are the primary drivers of differences between these two scenarios,
 817 particularly affecting the low values of Q_{crit} for water depths less than about 60 m. The remaining lines in
 818 Figure 9b show the results of the different entrainment scenarios in the MWI model as shown in Figure
 819 6 and Table 2. With the exception of the αRT scenario, these alternative scenarios for water entrainment
 820 lead to more rapid mixing of the jet with external water, thereby reducing the maximum depth of water
 821 through which the jet can penetrate and increasing the critical MER required to reach the tropopause. For
 822 the αRT scenario, the dependence of the entrainment coefficient on jet surface area to volume ratio (see
 823 Equation 36) causes the collapse and steam plume conditions to occur at shallow water depths compared to
 824 *Reference* scenario for $Q_0 \lesssim 10^7$. In contrast as $Q_0 \rightarrow 10^8$, collapse conditions still occur for shallower

825 water depths than the *Reference*, but the steam plume condition occurs at greater depths. For large MER,
 826 jet radius expands rapidly as the jet rises in the water column due to both decompression and an increase in
 827 steam volume fraction. As a consequence, α_{RT} decreases with height in the water column, reducing water
 828 entrainment rate and delaying the point at which the steam plume condition is reached. Critically, for all
 829 entrainment scenarios considered here, and regardless of the choice of atmospheric profile, we find that
 830 only the largest eruptions with $Q_0 \sim 10^9$ kg/s breach the tropopause for water depths greater than about
 831 200 m.

832 Figure 10 shows example results of eruption column height at both high latitude (*Reference* scenario, left
 833 column) and low latitude (*Low-Lat*, right column). Panels (a), (b) show column heights at varying water
 834 depth for three control values of MER, and (c), (d) show heights for varying MER at three fixed values of
 835 water depth. Solid lines show maximum column height, dashed lines show neutral buoyancy height, open
 836 circles show thresholds for column collapse, and closed circles show the threshold for steam plumes. The
 837 dominant effect of added external water on column height is to drive column collapse, which is consistent
 838 with the results of previous integral models of hydrovolcanic columns (e.g. Koyaguchi and Woods, 1996;
 839 Mastin, 2007b). Panels (a) and (b) show that for buoyant plumes, column height is essentially unchanged
 840 for water depth below decompression length, while for greater depths there is a 10 to 25% decrease in
 841 column height. For relatively low water depths and low MER, the release of latent heat drives increased
 842 column height, particularly from entrained atmospheric moisture in a humid atmosphere (e.g. panel (b)
 843 for $Z_e = 20$ m and $Q_0 = 10^6$ kg/s). However, for the high latitude atmosphere this is largely offset by the
 844 decreases in total height resulting from changes to column source parameters (e.g. panel (a) for $Z_e = 70$
 845 m and $Q_0 = 10^7$ kg/s, see Figure 8). Therefore in most cases, we find that both maximum height and
 846 neutral buoyancy levels of plumes decrease relative to the control simulations for increasing water depth.
 847 For buoyant plume scenarios with non-zero mass fraction of external water ($Z_e > L_d$), neutral buoyancy
 848 levels are typically reduced by 10 to 25%. Panels (c) and (d) show that increasing water depth narrows the
 849 range of MER for which buoyant columns may form. For example, at only 100 m of water depth, buoyant
 850 columns are restricted to MER between about 3×10^7 and 2×10^8 kg/s for the reference scenario, and an
 851 even narrower range for the low latitude atmosphere. Water depths greater than about 200 to 250 m result
 852 in either column collapse or failed plume conditions in our *Reference* simulations, except for very large
 853 MER $\sim 10^9$ kg/s.

854 3.4 Evolution of Particle Surface Area With Fragmentation and Sedimentation

855 Figure 11a shows particle specific surface area S (surface area per unit mass of particles - a metric for
 856 fine ash production) at the water surface after MWI, as a function of the concentration of residual water
 857 dissolved in the melt, c_{H_2O} . Symbol size represents MER for all panels in Figure 11 and colors denote
 858 the mass fraction of entrained external water. The upper limit of S following quench fragmentation is
 859 determined in the model primarily by the glass transition temperature, T_g . Simulations with high rates
 860 of exsolution in the conduit (particularly those with strong second bubble nucleation events near the
 861 fragmentation depth, see Figure 5f) result in lower c_{H_2O} and higher T_g (see Equation 45 and Figure 3b)
 862 upon entering the water layer. Higher T_g in turn reduces the total thermal energy available for production
 863 of fine ash during quench fragmentation, and these events have PSD's with consequently lower particle
 864 surface area. Since total gas exsolution is inversely correlated with Q_0 in our conduit model, values of S
 865 after quench fragmentation increase with increasing Q_0 , as shown by symbol size in Figure 11a.

866 Figure 11b shows S at both column source (i.e. water surface $z = Z_e$, grey symbols) and at maximum
 867 column height ($z = Z_{max}$, blue symbols) as a function of the water mass fraction at the plume source.
 868 In both panels (b) and (c), circles show buoyant plumes that do not breach the tropopause, 'x' symbols

869 show collapsing columns, and diamonds show plumes that are both buoyant and of sufficient magnitude to
870 breach the tropopause at the height of neutral buoyancy Z_{nbl} . Considering first values of S at the eruption
871 column source (grey symbols, panel (b)), the sharp plateau in S above $n_w \approx 0.15$ in panel (b) is a result of
872 cooling below the glass transition temperature, marked with a vertical blue bar (see also Figure 6e). For
873 entrained water mass fractions greater than this, quench fragmentation halts and S remains approximately
874 constant at a value determined primarily by the glass transition and the size of particles produced by quench
875 fragmentation (see Section 2.3.4 and Figure 3).

876 Blue symbols in panel (b) highlight the effects of sedimentation on ash surface area over the rise of the
877 subaerial eruption column. The PSD is further enriched in fine ash following fallout of coarse particles, and
878 S consequently increases with height of the eruption column. Furthermore, because the local rate of particle
879 loss from the edges of entraining eddies is proportional to the ratio of particle fall speeds to the mixture
880 rise speed according to Equation 60, buoyant plumes with low MER, rise velocities, and radii have the
881 largest increase in S during column rise. For collapsing columns ('x' symbols), S increases proportional to
882 maximum height prior to collapse. Owing to a combination of fines enrichment from quench fragmentation
883 and enhanced sedimentation due to reduced column rise speeds, all buoyant hydrovolcanic plumes (circle
884 and diamond symbols) increase in particle specific surface area at their maximum height with increasing
885 mass fraction of water.

886 The combined effects of quench fragmentation followed by sedimentation in the rising column influence
887 both total retained mass of ash in the eruption cloud and the surface area per unit mass of particles. Figure
888 11c shows the fraction of total erupted particle mass remaining in the column at its maximum rise height,
889 again as a function of water mass at the column source; symbols are as in panel (b), with colors showing S
890 at maximum column height. Small eruptions that do not reach the tropopause (circle symbols) lose the
891 greatest portion of their particle mass to sedimentation, while collapsing columns retain mass up to their
892 (relatively much lower) maximum height before collapsing entirely. Of note, however, are the subset of
893 eruptions that are both buoyant and of sufficiently high magnitude to breach the tropopause (highlighted
894 with an arrow in panel (c)). With increasing water mass fractions, such events not only retain a greater
895 portion of their initial pyroclast mass relative to control runs, but also have a more fines-enriched PSD in
896 the spreading cloud as measured by the S parameter. Provided they generate buoyant eruption columns, the
897 above results highlight the greater total flux of ash surface area to the spreading cloud for hydrovolcanic
898 scenarios, with important implications for chemical and microphysical interactions with SO_2 .

4 DISCUSSION

899 Here for the first time, we link the dynamics of magma flow in a volcanic conduit to the turbulent rise of an
900 overlying subaerial eruption column for a submerged volcanic vent, using a model which governs water
901 mixing into a gas-pyroclast jet and the coupled energetics of quench fragmentation. In marked contrast to
902 previous studies which parameterize the mass fraction of external water ingested into the subaerial eruption
903 column source (e.g. Koyaguchi and Woods, 1996; Mastin, 2007b; Van Eaton et al., 2012), we interrogate
904 eruption dynamics that evolve with magma-water interactions that depend explicitly on the depth of an
905 external water layer. Integral conduit and eruption column models of "dry" eruptions are well established
906 in previous studies (Gonnermann and Manga, 2007; de' Michieli Vitturi and Aravena, 2021; Woods, 2010).
907 Consequently, here we focus on effects of a water layer on the mechanical couplings among the conduit,
908 vent and eruption column model components and their consequences for column rise and gravitational
909 stability. We identify critical water depth conditions where column heights exceed the tropopause, explore
910 sensitivities of these results to parameterizations for water entrainment and quench fragmentation, and
911 compare results to observations of hydrovolcanic eruptions. We address, in particular, how key parameters

912 in the fragmentation model influence the fragmentation energy budget and govern the production of particle
913 surface area (ash). In addition to modulating the rise of a hydrovolcanic eruption column, the extent of
914 ash production potentially affects also the SO₂ absorption and the heterogeneous nucleation and growth
915 of sulfur aerosols. Thus, we conclude by discussing the co-injection across the tropopause of ash, SO₂,
916 and water in hydrovolcanic eruption clouds and implications for chemistry, microphysics, and associated
917 climate impacts.

918 **4.1 Water Entrainment and Mixing Efficiency Governs Eruption Column Buoyancy**

919 For a given MER, the model parameter that exerts the greatest control on atmospheric injection height
920 and mass loading of fine ash and water is the effective water entrainment coefficient α_{eff} . For a given
921 water depth, the height above the vent at which water entrainment effectively begins and the rate at which
922 water ingestion occurs govern the total mass of external water introduced into the column. The resulting
923 water budget controls, in turn, the total thermal energy transfer from the melt to heat external water and
924 supply the irreversible work to fragment pyroclasts to produce ash. The extent and rate of water entrainment
925 therefore governs the conditions for column collapse or buoyant rise, the extent of fine ash production
926 by quench fragmentation, and the depth at which water vapor is largely exhausted and the pyroclastic jet
927 transitions to a weak steam plume. To make clear the insight gained through our considering the controls
928 on the entrainment mechanics that govern column evolution, we will discuss in detail the behavior of our
929 different entrainment scenarios. For comparison, we introduce natural examples of eruptive phases that
930 involve interaction with water layers at various depths.

931 Except in the special case where the column does not decompress on exiting the vent, the decompression
932 length L_D acts to reduce the fraction of the water column height where entrainment can occur. Below the
933 crossover length L_X , where turbulent buoyant plume rise starts, the evolving local rate of entrainment
934 is less than the steady-state value above L_X . These expectations are broadly consistent with Saffaraval
935 et al. (2012) who demonstrate that for overpressured jets, entrainment was 30 to 60% less efficient at axial
936 distances less than about 5 vent diameters and vent overpressures up to about 3 atmospheres. In more detail,
937 over the decompression length L_D water entrainment is impossible by definition and none occurs where
938 $L_D > Z_e$. In contrast, for $L_D \leq Z_e$ water ingestion is possible and enhanced for (shallow) water depths
939 greater than around 2 vent radii because increases in hydrostatic pressure suppress decompression (Figure
940 8f). Consequently, with no decompression scaling (*No- L_d* scenario), whereas the threshold depth for steam
941 plumes is, for example, not significantly affected because the decompression length is very small at these
942 depths (see Figure 8f), the threshold water depth for column collapse and stratospheric injection decreases
943 by ~ 20 to 30% (see Figure 9b).

944 The mechanism of decompression length inhibiting water entrainment in our model can be related to
945 observations of real eruptions in shallow water layers. For example, the 2016-2017 eruption of Bogoslof
946 volcano featured both transient explosions and sustained plumes emerging from vents typically in water
947 depths of 5 to 100 m (Lyons et al., 2019). Lyons et al. (2019) interpreted acoustic signals of transient
948 events at Bogoslof to result from explosive expansion of large bubbles of magmatic gas, which limited
949 the direct interaction of external water with the erupting fragmented mixture. Deposits from these events
950 in the near-vent region suggested that little or no condensed water was present during emplacement of
951 pyroclastic surges, and Waythomas et al. (2020) interpreted this to mean that any water present was entirely
952 in vapor form, further suggesting that these explosive events were drier than is typical of "Surtseyan"-type
953 activity. The requirement for low liquid water content in pyroclastic surges at Bogoslof, combined with
954 the observations of Lyons et al. (2019), suggests either a highly efficient mixing process and complete
955 vaporization (possibly driven by molten-fuel-coolant explosions (Wohletz et al., 2013)), or limited ingestion

956 of external water by explosive expansion of magmatic gas in a shallow water setting. Whereas events in our
957 model with water depths less than L_d result in no incorporation of external water, we suggest this regime is
958 analogous to real events similar to those of Bogoslof where water depths are comparable to or less than
959 length scales for gas decompression, resulting in *limited* (though likely non-zero) amounts of external
960 water incorporated into the eruption column. An overpressured vent is required for this event to occur,
961 which is possible for either a steady eruption with choked vent flow, or for transient explosions originating
962 in the shallow conduit. In our simulations, pyroclasts cool to the water saturation temperature around water
963 mass fractions of 30-35% assuming that mixing and heat transfer are complete, at which point the liquid
964 water content rises dramatically. This is therefore a likely upper bound for the mass fraction of external
965 water in these relatively dry events at Bogoslof.

966 The crossover length scale L_X governs where in the water layer column rise transitions from that of a
967 pure jet to a turbulent buoyant plume. At and above this transition, entrainment by turbulent motions is
968 fully developed (see Equation 27). The crossover length is most sensitive to jet radius and velocity after
969 decompression (see Equation 31). The column rise speed changes little over L_D so long as the conduit
970 remains choked. However, the jet radius after decompression decreases rapidly with increasing hydrostatic
971 pressure and decreasing vent overpressure, and for deep water L_X approaches a value less than half of
972 that for a subaerial jet (see Figure 8 panels (d), (f), and (h)). As L_X decreases with increasing water depth,
973 α_{eff} increases more rapidly with height above the vent (see Equations 32, 33) and the jet entrains external
974 water at slightly greater rates for deeper water layers. However, more important remains the total height
975 over which water entrainment occurs. Without considering the crossover length scale (*No- L_X* scenario),
976 entrainment sufficient to cause column collapse or steam plumes occurs within only a few tens of meters of
977 where entrainment starts, even for very large MER (see Figure 9b). Because of the progressive increase of
978 α_{eff} with height in scenarios that include the L_X scaling, removing it in the *No- L_X* scenario has a greater
979 impact on the threshold for steam plumes than for the column collapse condition, relative to the *No- L_d*
980 scenario.

981 By definition, the *No- L_d -No- L_X* scenario has entrainment at rates corresponding to those for fully
982 developed turbulence in subaerial jets (e.g. Morton et al., 1956; Carazzo et al., 2008), and even for the
983 largest MER leads to ingestion of water masses sufficient to overwhelm jets that would otherwise lead to
984 stratospheric injections. For example at $Q_0 \approx 10^9$ kg/s stratospheric injection is prevented at water depths
985 greater than about 60 m, compared to a limit of 250 m in the *Reference* scenario (see Figure 9b). The
986 entrainment rates and collapse conditions in the *No- L_d -No- L_X* scenario are therefore likely inconsistent
987 with real hydrovolcanic eruptions. For example the $\sim 24,000$ BP Oruanui hydrovolcanic eruption in New
988 Zealand had estimated magma mass fluxes of 10^8 to 10^9 kg/s and is recognized for its remarkably wide
989 dispersal of airfall deposits (Wilson, 2001). This eruption emerged through Lake Taupo, which in modern
990 times has water depths averaging about 150 m, and is believed to have had depths of at least 100 m at the
991 time of the eruption (Nelson and Lister, 1995). These inferences are consistent with little water entrainment
992 and mixing in the near-field and reinforce the importance of considering L_d and L_X in the evolution of
993 buoyant subaerial columns from submerged volcanic jets.

994 The isothermal, single-phase experiments of Zhang et al. (2020) show that fully developed turbulence
995 with steady-state entrainment in subaqueous, supersonic jets occurs at a distance from the vent greater than
996 about ten vent diameters, with comparatively inefficient and transient entrainment modes dominating closer
997 to the jet source. For such subaqueous jets, both turbulent shear and buoyancy effects contribute to the
998 development of large turbulent eddies that inject surrounding water. For comparison with the typical shear-
999 driven entrainment condition used in our *Reference* scenario and to highlight potential variability in the

1000 entrainment mechanisms of real sub-aqueous volcanic jets, we parameterize buoyancy-driven entrainment
1001 in the αRT scenario using a slightly modified form of the “Rayleigh-Taylor” entrainment coefficient of
1002 Zhang et al. (2020) in Equations 35 and 36. Differences between the αRT and *Reference* scenarios (see light
1003 blue and black lines in Figure 9b, respectively) are governed by the $\alpha \propto a^2/q_c$ dependence of Equation
1004 36. For $Q_0 \lesssim 10^7$, the ratio of jet cross-sectional area to mass flux a^2/q_c is relatively large, resulting in
1005 large entrainment rates comparable to those for fully developed plumes (i.e. *No- L_d -no L_X* scenario) and
1006 consequently shallow water depths for the column collapse and steam-plume conditions. For $Q_0 \gg 10^7$
1007 kg/s, as entrained water is vaporized jet density initially decreases, resulting in enhanced Rayleigh-Taylor
1008 entrainment and column collapse for slightly shallower depths than the *Reference* scenario. However, for
1009 larger water depths where the jet cools to the water saturation temperature, entrained water remains liquid,
1010 jet density increases and radius decreases (see Figure 8, panels (h) and (j)). As a result, q_c dominates
1011 in Equation 36 for water depths much greater than the threshold for collapse, and entrainment rates are
1012 suppressed. The reduced entrainment rates for large MER and deep water layers, in turn, prevent total
1013 exhaustion of the particle heat budget such that, in contrast to other scenarios, the steam plume condition
1014 occurs for pressure-balanced jets much deeper than the limit for vent choking (see Figure 9b). As a final
1015 remark here, we reiterate that the mechanics of water entrainment exert the greatest control over column
1016 rise. Our results underscore, however, that this process is poorly understood and is a key avenue for future
1017 work on hydrovolcanism. As implemented, the shear-driven and buoyancy-driven modes govern water
1018 ingestion for very different MER-water depth conditions. Whereas it is straightforward to embrace both
1019 contributions parametrically through the effective entrainment coefficient given by Equation 35, there are
1020 no observational or experimental constraints on how best to characterize the relative contributions of each
1021 mode. Furthermore, how the underlying dynamics and their couplings are modified by local MFCI as well
1022 as particle inertial and buoyancy effects, as well as the character and thermal mixing properties of MWI,
1023 are unknown.

1024 Conditions leading to gravitational collapse in our model (water mass fractions $\gtrsim 30$ -40 wt%) are
1025 consistent with those in previous integral plume models of wet eruption columns (Koyaguchi and Woods,
1026 1996; Mastin, 2007b). Our results are further consistent with observations that buoyant, ash-laden subaerial
1027 eruption columns are rarely observed for water depths greater than about 100 m (Mastin and Witter, 2000).
1028 However, a challenge with interpretation of integral plume models is that they predict sharp boundaries
1029 between behavioral regimes (i.e. collapse or no collapse), whereas real eruptions have gradual transitions
1030 between behaviors. Columns that are either fully buoyant or completely collapsing are now understood to
1031 be end member behaviors, with eruption columns undergoing partial collapse and simultaneous rise of
1032 buoyant central columns and secondary plumes from pyroclastic density currents being commonplace (Neri
1033 et al., 2002; Gilchrist and Jellinek, 2021). Indeed, hydrovolcanic eruptions are noted for highly dispersive
1034 eruption columns with multiple spreading levels (Carazzo and Jellinek, 2013; Houghton and Carey, 2015),
1035 owing to complex cloud microphysical processes including latent heat exchange and hydrometeor formation
1036 (Van Eaton et al., 2012, 2015), wet particle aggregation (Brown et al., 2012; Telling et al., 2013; Van Eaton
1037 et al., 2015), or collective settling and diffusive convection (Carazzo and Jellinek, 2012, 2013). The
1038 thresholds shown in Figure 9, including for column collapse, stratospheric injection, vent choking, and
1039 plume failure are best interpreted as gradual transitions between likely behavioral regimes. Similarly, the
1040 condition for steam plumes represents a transitional regime where jets of liquid water, ash and steam can
1041 still breach the water surface and may produce water-rich plumes driven by moist convection, but the vast
1042 majority of water and particle mass collapses immediately at the surface or does not breach it at all (see
1043 Figure 8a). As an example of this regime, the eruption of South Sarigan Volcano in 2010 occurred in
1044 water depths of 180-350 m, and produced a column up to 12 km in height during its peak phase. However,

1045 satellite observations showed that the plume was very short-lived and consisted primarily of water, with
 1046 only minimal ash fallout or aerosols detected (McGimsey et al., 2010; Global Volcanism Program, 2013;
 1047 Green et al., 2013).

1048 A final consideration for the development of buoyancy in the subaerial eruption column is the effect of
 1049 thermal disequilibrium. To validate the assumption of thermal equilibrium in an integral model, Koyaguchi
 1050 and Woods (1996) assumed timescales for heat transfer between particles and entrained water of order
 1051 1 second or less, which is reasonable for particle diameters less than about 1 mm, and also requires the
 1052 column to be well-mixed. For the range of water depths considered here, typical timescales for the jet to
 1053 penetrate the water surface are about 0.1 to 5 seconds (assuming choked flow at the vent). Our MWI model
 1054 therefore assumes entrainment and heat transfer occur on timescales < 0.1 seconds, and further assumes
 1055 that internal turbulent mixing of the jet mixture with entrained water is complete on these timescales. If
 1056 disequilibrium heat transfer or incomplete mixing are considered, entrained water may not vaporize fully
 1057 over the timescale of rise through the water column, even for jets with bulk pyroclast temperatures well
 1058 above the water saturation temperature. In turn, the subaerial jet would host domains of varying fractions of
 1059 liquid water and vapor, resulting in heterogeneous density distributions in the early stages of the eruption
 1060 column. Such effects are beyond the capability of a 1D integral model and could further contribute to
 1061 partial column collapse or particle shedding events, with consequently reduced mass flux of particles and
 1062 gas in the rising column. An additional consequence of incomplete mechanical and thermal mixing is that
 1063 the column may retain a hot core of particles that do not supply thermal energy to entrained external water
 1064 to drive quench fragmentation, which is consistent with observations of pyroclast textures and particle sizes
 1065 (e.g. Moreland, 2017). Our assumed complete mixing and parameterized fragmentation efficiency thus
 1066 probably provides an upper bound to the extent of quench fragmentation and ash production.

1067 **4.2 Trade-offs Among Thermal Energy Budget, Particle Loss, Particle Surface** 1068 **Roughness, and Fragmentation Efficiency**

1069 Our fragmentation model aims to capture the essential energy and mass budget characteristics of quench
 1070 fragmentation derived from observational and experimental constraints on the glass transition temperature
 1071 T_g (Dingwell, 1998), the fragmentation energy efficiency ζ (Sonder et al., 2011), particle roughness Λ
 1072 (Zimanowski and Büttner, 2003; Fitch and Fagents, 2020), the initial PSD power-law exponent D (e.g.
 1073 Girault et al., 2014), and measured hydrovolcanic particle sizes (Costa et al., 2016). Here we focus on the
 1074 consequences of varying Λ , ζ , and D for production of fine ash. For reference, we refer to Section 3.4 and
 1075 Figure 11b, which plots *Reference* scenario particle specific surface area at two heights - column source
 1076 and maximum column height - as a function of column water mass fraction at the water surface. These
 1077 same data for the *Reference* scenario (i.e. gray and blue diamond symbols in Figure 11b) are again plotted
 1078 in Figure 12 in blue (now circles and diamonds for values at the column source and maximum height,
 1079 respectively), together with results of scenarios with alternative fragmentation model parameters (see Table
 1080 2). As in Figure 11b, MER is represented by symbol size. As described in Section 3.4, cooling below the
 1081 glass transition temperature limits the generation of additional ash surface area for total mass fractions of
 1082 water $n_w \gtrsim 0.15$. First examining the *Reference* scenario ($\zeta = 0.1$, $\Lambda = 10$, $D = 2.9$, and mean output
 1083 particle size, $\phi_\mu = 3.4$; blue symbols in Figure 12), this mechanical limit results in approximately a 20%
 1084 increase in ash specific surface area S at the base of the eruption column, and a 10-15% increase in S
 1085 at the spreading height, relative to control scenarios. As discussed in Section 3.4, coarse particle fallout
 1086 is relatively enhanced for low-MER events which have small radii and lower column rise speeds when
 1087 compared with larger MER. As a consequence, sedimentation in low-MER ($\ll 10^7$ kg/s) columns exerts a
 1088 stronger control on particle surface area than does quench fragmentation in our simulations, whereas the
 1089 two mechanisms are comparable in magnitude for larger eruptions.

1090 Red symbols in Figure 12 show the *High- Λ* scenario, where the particle roughness scale Λ is increased
1091 from 10 to 25 and other input parameters are held constant. Similar to Fitch and Fagents (2020), Λ has
1092 the largest influence on total ash surface area. Increasing Λ to 25 results in a proportional increase in
1093 initial surface area; the minimum value of S for the *Reference* scenario with no entrained external water
1094 is 860 m²/kg, and is 2160 m²/kg for the *High- Λ* scenario. However, the energy requirement to generate
1095 particles of a given size also increases proportionally. Since the fragmentation energy budget per unit mass
1096 of pyroclasts is approximately the same as in the *Reference* scenario (determined by magma heat capacity,
1097 fragmentation energy efficiency, and the glass transition temperature), the amount of total surface area
1098 generated during MWI is similar to the *Reference* scenario, but the proportional increase in S resulting
1099 from MWI is less than 10% relative to the control simulations. Comparing change in surface area resulting
1100 from water entrainment and quench fragmentation (red circles) with that resulting from sedimentation
1101 (difference between circles and diamonds), the effects of sedimentation in this case exert a much stronger
1102 control on ash surface area in the eruption cloud than does MWI. High particle roughness scenarios thus
1103 have the greatest total ash surface area in the eruption cloud, but a relatively modest change compared to
1104 control simulations with no external water.

1105 The fragmentation energy efficiency ζ governs the relative partitioning of irreversible thermal energy
1106 loss from the melt between that used to heat and vaporize water and that consumed by fragmentation and
1107 production of particle surface area. Choosing a low value for the fragmentation energy efficiency, $\zeta = 0.05$,
1108 (*Low- ζ* scenario, yellow symbols in Figure 12) reduces the energy consumed by fragmentation per unit
1109 mass of entrained water, resulting in overall less ash production before the glass transition limit is reached.
1110 This scenario has both the lowest total particle surface area after quench fragmentation and a modest change
1111 relative to control scenarios of 5 to 10%. The high fragmentation energy efficiency scenario with $\zeta = 0.15$,
1112 (*High- ζ* scenario, data not shown) has an effect of similar magnitude but opposite sign on specific surface
1113 area S compared with the *Low- ζ* scenario. S after sedimentation in the eruption column, however, is very
1114 similar to that for the *Reference* scenario, and we consequently do not show those results in Figure 12.

1115 The initial PSD, governed by D , determines the relative weight of particles towards fine or coarse
1116 fractions prior to MWI. Since we fix the particle sizes produced by quench fragmentation to values based
1117 on the phreatomagmatic Phase C of the Askja 1875 eruption (see Section 2.3.4 and Figure 3), an initial PSD
1118 already enriched in these particle sizes will not change significantly in our MWI model, and consequently
1119 little fragmentation energy will be consumed. The *High- D* scenario with $D = 3.2$, (purple symbols in
1120 Figure 12) results in very high initial particle surface area (~ 2050 m²/kg) but only minor changes to
1121 the PSD and S from MWI and sedimentation (the highest values of S at the maximum plume height are
1122 ~ 2200 m²/kg). Consequently, the strongest control on production of ash surface in this scenario is the
1123 minimum particle size that can be produced during quench fragmentation.

1124 The results of the various fragmentation scenarios above reveal an important trade-off among particle
1125 size distribution, particle roughness, and the consumption of fracture surface energy during quench
1126 fragmentation. The primary effect of the glass transition limit and fragmentation energy efficiency is
1127 to determine the energy budget for fragmentation, whereas particle roughness and surface energy limit
1128 the mass of fine particles that can be produced within a given energy budget. The initial PSD, in turn,
1129 determines the mass of “coarse” particles available with which to generate new fine ash. The mass in
1130 this coarse fraction is dependent on the choice of particle sizes that fragment during quenching, and the
1131 preferred sizes of particles produced. Our simple mechanical energy balance model relies on a prescribed
1132 initial PSD and on a perfect conversion of fragmentation energy to the plastic work of brittle fragmentation.
1133 For a given ζ , the approach provides a crude and probably lower bound that should be applied cautiously.

1134 Whereas we fix the particle sizes generated by quench fragmentation to those of a known deposit, modal
1135 particle sizes from quench fragmentation vary as a function of melt properties and cooling rates (van
1136 Otterloo et al., 2015), as well as bubble size distributions (Liu et al., 2015). Our model further assumes that
1137 quench fragmentation is a brittle failure process limited in extent by rapid cooling below the glass transition
1138 temperature (e.g. Mastin, 2007a; van Otterloo et al., 2015). This limit constrains failure to occur only
1139 in conditions in which the melt phase can accumulate elastic thermal stresses in excess of a yield stress.
1140 This approach neglects, for example, potentially important time-dependent effects related to the growth
1141 of thermal stress gradients and stress concentrations, which can arise with additional cooling (Woodcock
1142 et al., 2012; van Otterloo et al., 2015), and evolve depending on the character of the water boiling regime
1143 at the melt-water interface (Moitra et al., 2020). The cessation of quench fragmentation with decreasing
1144 particle temperature is probably more gradual in real eruptions than in our model (see Supplementary
1145 Material Section S2 and Supplementary Figure S4 for additional discussion of thermal stresses during
1146 quench fragmentation). Despite these complexities, together with consideration of the entrained masses of
1147 water in hydrovolcanic eruption columns, these constraints allow estimation of the total mass and surface
1148 area of fine ash delivered to the spreading levels of buoyant hydrovolcanic eruption clouds.

1149 **4.3 Water Layer Depth, Volatile Saturation and Fragmentation in the Conduit, and Vent** 1150 **Choking**

1151 The additional hydrostatic pressure with a water layer overlying the vent influences the results of our
1152 coupled model in two primary ways: (1) it modulates the extent to which a vent is choked and overpressured,
1153 and (2) it controls the total amount of gas exsolved from the melt (Smellie and Edwards, 2016; Cas and
1154 Simmons, 2018; Manga et al., 2018), which, in turn, influences both the magma ascent rate and the quench
1155 fragmentation process. For water depths near the collapse threshold, magma flow at the vent is choked
1156 and overpressured (see Figure 8 panels (a),(d), and (e), and Figure 9a). Consequently, the column collapse
1157 condition is not heavily influenced by changes in conduit conditions with increasing water depth, and is
1158 primarily determined by the mass fraction of entrained external water. However, for water depths sufficient
1159 to suppress vent overpressure, $L_d \rightarrow 0$ and L_X approaches its minimum value. Entrainment consequently
1160 starts near the vent and ingestion rates are typically faster overall for pressure-balanced jets, which is
1161 broadly consistent with experimental comparisons of overpressured and pressure-balanced jets (Saffaraval
1162 and Solovitz, 2012). This condition leads to the tendency for the steam plume regime to coincide with the
1163 water depth limit for choking (Figure 9a). However, as discussed in Section 4.1, the choking and steam
1164 plume conditions need not coincide if entrainment rates are either very high (e.g. *No- L_d -no L_X* scenario) or
1165 very low (e.g. αRT scenario for $Q_0 \gtrsim 10^8$ kg/s). Therefore buoyant columns are most likely for subaqueous
1166 eruptions that are choked and overpressured at the vent as opposed to pressure-balanced, but this is not a
1167 strict requirement and depends on the dynamics of decompression and water entrainment near the vent, as
1168 well as the conditions for choking (for example the mixture sound speed).

1169 Comparing total exsolution for small and large water depths (Figure 5f), differences in vapor exsolution
1170 in the conduit model control the glass transition temperature (Figure 3b), which, in turn, governs the heat
1171 budget available for ash production during the quench fragmentation (Figure 11a). This effect is most
1172 apparent when considering events with a second nucleation event occurring in the conduit model for low
1173 MER (Figure 5f). Specifically, diffusion rate of vapor leaving the melt is sensitive to bubble number density,
1174 so a second nucleation event near fragmentation enhances exsolution rate above fragmentation, leading
1175 to the sharp change in total exsolution shown in Figure 5f. Simulations with a strong second nucleation
1176 in the conduit result in distinctly different production of ash surface area during quench fragmentation
1177 (Figure 11a for $c_{H_2O} < 0.6$ wt.%). As we will show in Section 4.5 below, the influence of this process on
1178 the dispersed mass of fine ash is apparent in our model even at the spreading height of the eruption cloud.

1179 For primary brittle fragmentation and explosive volcanism to occur during magma ascent in the conduit
 1180 (i.e. without the influence of external water), either gas overpressure in bubbles must exceed the tensile
 1181 strength of the melt, or the rate of magma ascent must be sufficiently high to exceed the critical strain
 1182 rate for brittle failure of the melt (Papale, 1999; Gonnermann, 2015). As described in Section 3.1, both
 1183 maximum decompression rate and maximum bubble overpressure (as recorded at the fragmentation depth)
 1184 decrease with increasing hydrostatic pressure in our conduit model. In Figure 5d, we show that for water
 1185 depths of about 200 m or greater, the maximum bubble overpressure Δp_b in our model falls below values
 1186 likely to cause rupture of bubble walls. Were bubble overpressure used as the fragmentation criteria in our
 1187 conduit model, fragmentation could in principle still occur, albeit at shallower depths in the conduit, but
 1188 becomes increasingly less likely with increasing water depth (Campagnola et al., 2016; Cas and Simmons,
 1189 2018). For example, Manga et al. (2018) used a strain-rate fragmentation criterion to estimate that for the
 1190 2012 submarine eruption of Havre volcano, magmatically-driven brittle fragmentation in the conduit could
 1191 only have occurred if the vent were shallower than about 290 m. It is worth noting that brittle fragmentation
 1192 mechanisms in general, particularly those driven by water interaction, are not precluded at such depths,
 1193 though explosive expansion of steam is suppressed (Murch et al., 2019; Dürig et al., 2020a). Critically,
 1194 increasing thicknesses of water or ice will increasingly suppress the conditions for which sustained brittle
 1195 or explosive fragmentation may drive gas jets or plumes, particularly those capable of reaching tens of
 1196 kilometers into the atmosphere.

1197 4.4 Sensitivity: Water Infiltration into the Shallow Conduit

1198 As highlighted in Section 2.1, our coupled conduit-vent-plume model scenarios do not include the effect
 1199 of water infiltration into the shallow conduit. However, some ingress of groundwater into the conduit
 1200 is likely in many circumstances. Accordingly, we show sample calculations and simulations to explore
 1201 potential effects on eruption column behavior in our MWI and plume models. Existing models of magma-
 1202 water interaction (MWI) in the shallow conduit (i.e. above the level of fragmentation) (Starostin et al.,
 1203 2005; Aravena et al., 2018) have highlighted that the increased gas content resulting from vaporization
 1204 of external water leads to an increase in vent velocity, vent overpressure, and mass eruption rate (MER),
 1205 and reduced eruption temperatures. Of greatest importance for the purposes of this study are the extent to
 1206 which water infiltration into the shallow conduit may influence the behavior regimes highlighted in Section
 1207 3.3 and Figure 9, thereby influencing the conditions for stratospheric injection. In particular, added water
 1208 in the conduit will increase the gas pressure at the vent, and therefore deepen the critical water depth at
 1209 which vent choking and overpressure are suppressed. Here we perform a sensitivity analysis for changes to
 1210 the choking condition arising from the infiltration of external water into the conduit, and resulting effects
 1211 on water entrainment, plume rise, and stratospheric injection in our model. We do not consider cases where
 1212 the conduit geometry is modified by failure or erosion during MWI, and we also do not include the effects
 1213 of fragmentation resulting from water infiltration into the conduit prior to eruption (i.e. additional energy
 1214 consumed through mechanical modifications to the grain size distribution).

1215 For a choked conduit flow ($M = 1$) the theoretical pressure at the vent can be approximated as (Koyaguchi,
 1216 2005)

$$p_{choke} \approx \sqrt{n_v R_v T} \frac{q}{A_c} \approx \rho c^2, \quad (63)$$

1217 where $c = \sqrt{n_v R_v T}$ is a simplified expression for the pseudo-gas sound speed (Woods and Bower, 1995),
 1218 R_v is the specific gas constant for water vapor, T is the mixture temperature, and $A_c = \pi a_c^2$ is the conduit
 1219 cross-sectional area. Equation 63 is in excellent agreement with our conduit simulations with choked vents,
 1220 whereas simulations in which hydrostatic pressure exceeds p_{choke} are pressure-balanced ($\beta \approx 1$, $M < 1$)

1221 at the vent (see Supplementary Figure S6). Considering Equation 63 and neglecting any changes to the
 1222 conduit geometry or magmatic mass flux, the addition of external water into the conduit will have the
 1223 dual effect of increasing the gas mass fraction n_v (provided the water is all vaporized), and decreasing
 1224 the mixture temperature T . From the results of Aravena et al. (2018), mass fractions of external water
 1225 infiltrating into the conduit n_{ec} greater than about 5 wt.% are not favored for rhyolitic compositions and
 1226 will tend to lead to conduit failure. Here for completeness, we consider mass fractions $0 \leq n_{ec} \leq 0.15$, at
 1227 which values all of the water is in the vapor phase after mixing (pressures in the regimes presented here are
 1228 generally well below the critical point for water). To calculate the mixture temperature after infiltration
 1229 and mixing of external water into the conduit, we calculate water properties for groundwater assuming an
 1230 average depth of 100 m below the rock surface (accounting for hydrostatic pressure from external water)
 1231 and at temperature $T_{ec} = 274.15$ K using the IAPWS-95 Standard (Junglas, 2009). For simplicity we
 1232 assume constant latent heat of vaporization L_{ec} and heat capacities for water C_l and vapor C_v (for example,
 1233 typical average values are 1.85×10^6 J/kg, 4.22×10^3 Jkg⁻¹K⁻¹, 2.23×10^3 Jkg⁻¹K⁻¹, respectively, for
 1234 temperature ranges between T_{ec} and magmatic temperature T_0), and magma $C_m = 1250$ Jkg⁻¹K⁻¹. The
 1235 approximate energy balance following thermal mixing of external water into the conduit is

$$0 \approx (1 - n_v)C_m(T - T_0) + n'_0C_v(T - T_0) + n_{ec}[C_l(T_{sat} - T_{ec}) + L_{ec} + C_v(T - T_{sat})], \quad (64)$$

1236 where $n'_0 = n_0(1 - n_{ec})$ is the adjusted mass fraction of initial magmatic water vapor after mixing with
 1237 external water, and $n_v = n_{ec} + n'_0$ is the total water vapor mass fraction after mixing. Solving Equation 64
 1238 for the final temperature T gives

$$T \approx \frac{T_0C_B - n_{ec}C_l(T_{sat} - T_{ec}) - n_{ec}(L_{ec} + C_vT_{sat})}{C_B + n_{ec}C_v}, \quad (65)$$

1239 where $C_B = (1 - n'_0)C_m + n'_0C_v$. Equations 63 and 65 can be used to calculate the theoretical pressure
 1240 for a choked vent $p_{choke}(q_0, n_{ec})$, assuming vent radii equal to those of the control simulations with no
 1241 external water (see Section 2.5). Where p_{choke} is less than ambient hydrostatic pressure, the vent pressure
 1242 can be assumed equal to the hydrostatic pressure, resulting in a pressure-balanced jet with $M < 1$. Mixture
 1243 density, sound speed, vent velocity, and particle volume fraction are then calculated from corresponding
 1244 water equations of state and magmatic properties using the above estimated pressure and temperature. See
 1245 Supplementary Material Section S3 and Figures S6 and S7 for a comparison of model results with these
 1246 theoretical relationships.

1247 To demonstrate the effect of water infiltration into the conduit on the MWI and eruption column models,
 1248 Figure 13 shows a series of model simulations in which we calculate the vent condition from the above
 1249 relations (i.e. without running the conduit model, but using a sound speed corresponding to Equation 6 and
 1250 running the MWI and plume models from the calculated vent condition). We use a fixed magmatic mass
 1251 flux of $q_0 = 2 \times 10^7$ kg/s, $0 \leq n_{ec} \leq 0.15$ (see also Supplementary Figure S7), and vary water depths from
 1252 0 to 300 m ($Z_e/a_c \approx 12$). Panel (a) shows the critical water depth at which hydrostatic pressure exceeds
 1253 the vent choking pressure, resulting in a transition to a pressure-balanced jet. Values of n_{ec} corresponding
 1254 to the simulations shown in panels (b)-(e) are highlighted with blue and gray circles. For $n_{ec} = 0.15$, the
 1255 water depth limit for choking is more than doubled (from 130 to 267 m) relative to the case with no external
 1256 water in the conduit. Panels (b), (c), and (d) show subaerial eruption column source parameters after breach
 1257 of the water surface for varying water depth Z_e and conduit water fractions n_{ec} , and panel (e) shows
 1258 the eruption column height. Panel (b) shows the total mass fractions of vapor and liquid water (external
 1259 and magmatic). Importantly, the water depth at which liquid water dominates the jet (the steam plume

1260 condition) differs only by about 20 meters between scenarios. Panel (c) shows column source temperature,
 1261 highlighting the change in decompression length and onset of mixing with surface water that results from
 1262 increased gas pressure at the vent. Panel (d) shows the increase in jet velocity, driven by changes in the
 1263 mixture sound speed and jet density as it travels through the water column. Panel (e) shows the maximum
 1264 plume height and level of neutral buoyancy, which decrease by up to about 3 and 1.7 km respectively with
 1265 $n_{ec} = 0.15$. The water depth threshold for column collapse is increased by up to about 40 m relative to
 1266 scenarios with no external water in the conduit. The critical result of the above analysis is that despite a
 1267 doubling of the depth threshold for vent choking highlighted in panel (a), infiltration of external water into
 1268 the conduit changes the behavior thresholds of the eruption column passing through a surface water later
 1269 by a comparatively small amount of tens of meters. An important caveat to this discussion is that these
 1270 simulations do not include the potential for highly energetic and impulsive releases of energy driven by
 1271 fuel-coolant interaction, or related changes in the magmatic mass flux and vent geometry that may arise
 1272 from an influx of external water.

1273 4.5 Stratospheric Injection in Hydrovolcanic Eruptions and Implications for Sulfate 1274 Aerosol Lifecycle

1275 Radiative forcing by sulphate aerosols is governed by the total mass of injected sulfur dioxide, the height,
 1276 season, and latitude of injection, and the chemical and microphysical processes that determine the resulting
 1277 aerosol particle size distribution (Timmreck, 2012; Lacis, 2015; Kremser et al., 2016; Marshall et al.,
 1278 2019; Toohey et al., 2019). The injection height relative to tropopause height is critical for determining
 1279 the mass of stratospheric sulfur burden. However, the total mass and size distribution characteristics of
 1280 fine ash as well as high water content in hydrovolcanic eruptions are also likely to play a role in the life
 1281 cycle of sulfur aerosols. For example, LeGrande et al. (2016) showed that the coincident injection of
 1282 SO₂ with high concentrations of water can shorten the characteristic timescale for conversion of SO₂ to
 1283 aerosol from weeks to days, enhancing aerosol radiative forcing in the earliest weeks after an eruption.
 1284 Chemical scavenging of SO₂ onto ash surfaces is a potentially important source of SO₂ removal both
 1285 during eruption column rise and in the days and weeks following an eruption (Rose, 1977; Schmauss and
 1286 Keppler, 2014; Zhu et al., 2020). Experimental results from Schmauss and Keppler (2014) demonstrated
 1287 that SO₂ absorption onto ash particle surfaces is most efficient where volcanic plumes are cool, SO₂ is
 1288 dilute, and ash surface areas are high - all conditions that are likely to be enhanced in hydrovolcanic
 1289 eruption columns relative to purely magmatic cases. Zhu et al. (2020) reported that persistent fine ash
 1290 particles dispersed along with SO₂ from the 2014 eruption of Kelut Volcano contributed to enhanced
 1291 nucleation of aerosol particles onto ash surfaces and aerosol particles sizes up to 10 times that of typical
 1292 background stratospheric aerosol. Critically, chemical uptake of SO₂ onto ash surfaces increased the rate
 1293 of sulfur removal by sedimentation by 43% in the first two months following the eruption.

1294 Figure 14 shows estimates for the flux of SO₂, fine ash, and water to the tropopause for simulations with
 1295 two different atmospheric profiles (*Reference*, top row of panels and *Low-Lat*, bottom row). Panels (a)
 1296 and (b) show the estimated fraction of SO₂ delivered to or above the tropopause, where we approximate
 1297 the vertical distribution of the SO₂ cloud $\psi_{SO_2}(z)$ as a gaussian profile of thickness proportional to (and
 1298 centered on) injection height Z_{nbl} (Aubry et al., 2019):

$$\psi_{SO_2} = \exp\left(\frac{-(z - Z_{nbl})^2}{(0.108(Z_{nbl} - Z_e))^2}\right) \quad (66)$$

1299 The estimated fraction of SO₂ delivered to the stratosphere is the fraction of the integrated area of Equation
 1300 66 that lies above the tropopause. Events with injection heights close to the tropopause ($Q_0 \approx 3 \times 10^6$ kg/s

1301 and $Q_0 \approx 3 \times 10^7$ kg/s in the high and low latitude atmospheres, respectively) show reduced efficiency
1302 of stratospheric delivery of SO_2 for water depths that surpass the decompression length (and therefore
1303 non-zero quantities of external water are entrained). The exceptions are columns in the low-latitude
1304 atmosphere with minor quantities of entrained water ($n_w \approx 0.15$), which have increased column heights
1305 relative to control scenarios (see Figure 10b). Panels (b) and (c) show the ratio of fine ash mass flux (particle
1306 diameter $< 125 \mu\text{m}$) at the maximum plume height relative to control simulations. We find that events
1307 with sufficient entrained water to pass the glass transition (and thus maximize production of fine ash in our
1308 model) deliver a fine ash mass flux approximately 2-fold that of the control simulations. For low MER
1309 simulations with a second nucleation event in the conduit ($Q_0 \lesssim 4 \times 10^6$ kg/s), and consequently relatively
1310 less fine ash production, the mass flux of fine ash delivered is approximately 1.5 times that of the control
1311 cases. Finally, panels (e) and (f) show the ratio of water mass flux at maximum plume height compared to
1312 control scenarios. Buoyant hydrovolcanic plumes that breach the tropopause carry water mass fluxes of up
1313 to 10 times that of control simulations. Low-latitude eruption columns in humid atmospheres entrain a
1314 greater mass of atmospheric moisture, such that this ratio is somewhat less for the *Low-Lat* scenario, with
1315 typical values of 2 to 7 times that of control simulations.

1316 In summary, we find that incorporation of high mass fractions of external water in eruption columns
1317 acts to reduce eruption column height or induce gravitational collapse, while also enhancing conditions
1318 for chemical scavenging of SO_2 into ash and hydrometeors, including initially colder temperatures, high
1319 available ash surface area, and abundant water. For SO_2 that does reach the stratosphere, results of LeGrande
1320 et al. (2016) and Zhu et al. (2020) suggest that the presence of water and fine ash enhance aerosol reaction
1321 rates and sedimentation. Our results imply that in the absence of an explicit functional dependence on
1322 the change in PSD related to MWI, the SO_2 delivery efficiency given by Equation 66 is at best an upper
1323 bound where eruptions interact with water layers deeper than about 50 m. On the basis of results presented
1324 here, we suggest that hydrovolcanic eruption processes will on average act to reduce the climate impacts of
1325 volcanic aerosols. However, the evaluation of stratospheric sulfur loading in volcanic eruptions requires
1326 further analysis, particularly of microphysical processes not included in our model. For example, moist
1327 convection in water saturated air may enhance lofting of secondary plumes even for collapsing columns,
1328 potentially delivering SO_2 to the stratosphere following dynamics similar to thunderstorms (Van Eaton et al.,
1329 2012; Houghton and Carey, 2015). Alternatively, formation of hydrometeors (graupel, hail, or liquid water
1330 droplets) and aggregation of ash particles can lead to sedimentation of fine ash and water at much higher
1331 rates than predicted by particle settling time alone (Brown et al., 2012; Van Eaton et al., 2015), and column
1332 buoyancy and sedimentation processes can be further modified by interaction with atmospheric cross-winds
1333 (Girault et al., 2016). If sedimentation occurs faster than the timescales for chemical scavenging of SO_2
1334 onto ash surfaces, this can lead to early separation of ash and gas phases, as was observed for the 2011
1335 eruption of Grímsvötn Volcano (Prata et al., 2017). However, if the timescale for SO_2 scavenging is fast
1336 relative to particle fallout time as a result of say, high particle surface area and cold column temperature
1337 (Schmauss and Keppler, 2014), then aggregation-enhanced particle settling could act to efficiently remove
1338 scavenged SO_2 from the eruption column. For example, despite the observed separation of ash and gas
1339 clouds in the Grímsvötn eruption, Sigmarsson et al. (2013) estimated that approximately 30% of outgassed
1340 SO_2 was scavenged by ash particles and subsequently removed from the eruption cloud, with an additional
1341 10% lost directly to the subglacial lake (16% and 5% of the total magmatic sulfur budget, respectively).

1342 4.6 Implications of Hydrovolcanism for Volcano-Climate Feedback

1343 We have discussed coupled processes in hydrovolcanic eruptions which suggest that the stratospheric
1344 sulfate aerosol climate impacts of hydrovolcanic eruptions are likely to be reduced relative to dry eruptions.

1345 This hypothesis, in turn, suggests the potential for a largely unrecognized mechanism for volcano-climate
1346 feedback, where changes to the relative extent or frequency of hydrovolcanism resulting from evolving
1347 climatic conditions (glacial-interglacial cycles, for example) in turn modulate volcanic aerosol forcing. This
1348 feedback mechanism potentially acts concurrently to the effect of changing stress fields on the crust as a
1349 result of ice sheet advance and retreat, referred to as the ‘unloading effect’ in Cooper et al. (2018). Regional
1350 to global-scale changes in the occurrence of hydrovolcanism could for example arise from enhanced
1351 eruption rates in glaciated regions during glacial unloading (e.g. Jellinek et al., 2004; Sigmundsson et al.,
1352 2010; Albino et al., 2010). Huybers and Langmuir (2009) suggest that globally enhanced rates of volcanism
1353 would lead to an amplifying feedback where outgassing of volcanic carbon contributed to additional
1354 warming. This hypothesis was based on the assumption that time-averaged radiative forcing of volcanic
1355 CO₂ is stronger (over century to millennial timescales) than that of short-lived aerosol cooling events.
1356 However, the potential for climate impacts on multi-decadal to millennial timescales (Zhong et al., 2011;
1357 Baldini et al., 2015; Soreghan et al., 2019; Mann et al., 2021) challenges this view, and there is open debate
1358 on whether (or under what climate conditions and/or timescales) the effects of global volcanism drive net
1359 climate cooling or warming (Baldini et al., 2015; Lee and Dee, 2019; Soreghan et al., 2019). For example,
1360 Baldini et al. (2015) suggest that large volcanic sulphate injections during the Last Glacial Maximum drove
1361 hemispherically asymmetric temperature shifts and millennial-scale cooling feedbacks. A change in the
1362 relative global frequency of hydrovolcanism is one potential mechanism for steering the volcanic climate
1363 control in one direction or another over these timescales. In particular, the outgassing of volcanic CO₂
1364 is likely less affected by surface MWI than is SO₂, since CO₂ exsolves at initially greater crustal depths
1365 (Wallace et al., 2015) than SO₂ and its climate impacts are insensitive to injection height or co-emission
1366 with ash and water. On timescales of centuries to millennia, this process could in principle modulate the
1367 global importance for climate forcing of volcanic sulfate aerosols relative to volcanic carbon and therefore
1368 alter the character (e.g. amplifying or stabilizing) of volcano-climate feedbacks resulting from glacial
1369 unloading. The extent to which hydrovolcanism modulates global volcano-climate forcing remains an open
1370 question, and likely depends critically on both eruption rates and the surface distribution and thickness of
1371 ice sheets overlying volcanic regions, and the resulting frequency and intensity of hydrovolcanic processes.

1372 **4.7 Emerging Constraints and Knowledge Gaps for Silicic Hydrovolcanic Eruptions**

1373 The primary research goal of this study is to highlight external water controls on the climate impacts of
1374 hydrovolcanic eruptions. In attempting to address this central question, we have highlighted connections
1375 among magmatic heat budget, mixing efficiency with external water, and the extent of quench fragmentation
1376 which are relevant to general aspects of hydrovolcanic eruptions. First, we show that the combined effects of
1377 gas decompression and the monotonic development of turbulence in the overlying eruption column reduce
1378 the height over which water entrainment and mixing can occur and the overall rate of entrainment relative to
1379 subaerial jets and plumes. Indeed, a key finding is that without this mechanical modulation and regardless of
1380 the predominant mechanism for water entrainment, water mass fractions sufficient to exhaust the pyroclast
1381 heat budget are ingested in relatively shallow water depths of tens of meters for even very large eruptions
1382 (see the No- L_d -No- L_X scenario in Figure 9b). Second, we include fragmentation in the energy conservation
1383 scheme to quantify a relationship between the amount of entrained external water and the extent of quench
1384 fragmentation. Assuming the fragmentation energy efficiency of Sonder et al. (2011) is broadly applicable,
1385 extensive fines-enrichment of the total PSD can occur for relatively modest mass fractions of entrained
1386 external water ($n_e \approx 0.12$, see Figure 3). Taken together, these two insights highlight two classes of
1387 question for further research into coupled hydrovolcanic processes: 1) What are the quantitative connections
1388 among hydrostatic-pressure influenced volatile exsolution, pyroclast vesicularity and permeability, glass
1389 transition temperature, and particle size distributions following magmatic fragmentation? How do the above

1390 connections modulate the mechanisms and products of fragmentation resulting from water entrainment
 1391 and thermal mixing? 2) What are the predominant mechanisms governing the entrainment and mechanical
 1392 and thermal mixing of external water into hot eruption columns? In particular, under what conditions is
 1393 the erupting mixture particularly affected by the additional intrusion of water into the conduit through
 1394 permeable wall rock (e.g. Barberi et al., 1989; Aravena et al., 2018)? Where and at what spatial scales,
 1395 eruption stages, or flow regimes do processes such as molten-fuel coolant interactions (e.g. Zimanowski
 1396 and Büttner, 2003) dominate? Under what conditions can energetic fuel-coolant interactions or lofting
 1397 from secondary plumes following column collapse enhance stratospheric delivery of sulfur dioxide relative
 1398 to mechanisms presented here?

1399 4.8 Summary

1400 We present a novel coupled integral model of conduit and eruption column dynamics for hydrovolcanic
 1401 eruptions. We have simulated steady phases of explosive eruptions through a shallow water layer ($Z_e \lesssim 500$
 1402 m) overlying the volcanic vent, including the effects of gas exsolution and magma ascent in the conduit,
 1403 water entrainment and quench fragmentation, and eruption column rise and particle fallout. Based on
 1404 our model results and arguments in Sections 4.1 to 4.5, in addition to findings of previous studies, we
 1405 summarize key effects of changes in hydrostatic pressure and direct MWI on steady explosive eruption
 1406 processes:

- 1407 1. Increasing hydrostatic pressure with water depth reduces vent overpressure and the likelihood for
 1408 choking in the conduit. These effects limit the magnitude of explosive decompression and reduce vent
 1409 velocities. Choked vents do not occur in our simulations for water depths greater than about 5 vent
 1410 diameters.
- 1411 2. Increasing hydrostatic pressure with water depth reduces gas exsolution and decompression rates in
 1412 the conduit, decreasing the total fraction of gas that is exsolved on eruption at the vent, and potentially
 1413 limiting the conditions for magmatically-driven fragmentation (e.g. bubble overpressure).
- 1414 3. The total mass of entrained water increases with water depth, driving a decrease in eruption column
 1415 heights. Column collapse occurs for water mass fractions greater than about 30%.
- 1416 4. There is a range of water mass fractions (10-15%) in the starting subaerial jet in which plumes heights
 1417 are increased relative to dry control scenarios as a result of high vapor mass fractions and the release
 1418 of latent height with condensation. However, we find that plume heights are increased only in moist,
 1419 low-latitude atmospheres and for a very narrow range of water depths.
- 1420 5. The critical mass eruption rate required for eruption columns to reach the tropopause is sensitive
 1421 to increasing water depth and is governed primarily by the column collapse condition. For water
 1422 depths greater than about 200 m, only the largest eruptions ($MER \sim 10^9$ kg/s) reach the tropopause,
 1423 independent of the eruption latitude.
- 1424 6. As water depth exceeds the limit for which overpressured vents occur ($Z_e \gtrsim 5$ vent diameters in our
 1425 *Reference* scenario), the magmatic heat budget becomes exhausted, gas phases condense, and water in
 1426 the jet approaches 100% liquid. Such events may still generate subaerial jets and steam plumes, but are
 1427 unlikely to inject significant quantities of SO_2 or ash into the stratosphere. We find that hydrostatic
 1428 pressures sufficient to suppress choking in the vent are similar to those for which minimal steam ($\lesssim 5$
 1429 wt.% of the jet water phase) breaches the surface of the external water layer.
- 1430 7. Fine ash production by quench fragmentation leads to an approximately 2-fold increase in the mass
 1431 flux of fine ash ($< 125\mu\text{m}$) delivered to buoyant eruption clouds in our *Reference* scenario. Entrained
 1432 external water increases mass flux of water to the spreading cloud by up to 10-fold.

1433 8. The total ash surface area available for chemical absorption of SO₂ systematically increases in
1434 hydrovolcanic scenarios relative to control cases. However, the total surface area generated is sensitive
1435 to processes governing particle fallout and to the physics of quench fragmentation (e.g. particle
1436 roughness and surface fracture energy, and the fraction of thermal energy consumed for fragmenting
1437 particles). We suggest that the high water and fine ash content and colder temperature of hydrovolcanic
1438 columns provide conditions that enhance scavenging of SO₂ by ash and hydrometeors relative to
1439 subaerial eruptions (Schmauss and Keppler, 2014).

1440 The above results are consistent with expectations for conduit ascent in submarine and subglacial
1441 eruptions (Smellie and Edwards, 2016; Wallace et al., 2015), and for the rise of hydrovolcanic eruption
1442 columns in the atmosphere (Koyaguchi and Woods, 1996; Mastin, 2007b). Furthermore, increasing water
1443 depths or ice thicknesses beyond threshold conditions for choked flows at the vent will lead to governing
1444 physical processes not included in our model that further act to reduce or prevent stratospheric injections
1445 of ash and volatiles (e.g. Gudmundsson et al., 2004; Manga et al., 2018). On the basis of these arguments,
1446 we hypothesize that hydrovolcanic eruptions will, *on average*, tend towards reduced stratospheric loading
1447 and residence times of sulfate aerosols relative to purely magmatic eruptions. To the extent that volcanic
1448 aerosol radiative forcing is governed by the stratospheric load and injection altitude of SO₂, H₂O, and ash,
1449 hydrovolcanism will reduce the overall climate impact. Thus, depending on the distributions of water and
1450 ice sheets on the Earth's surface, hydrovolcanism could, in principle, modulate putative volcano-climate
1451 feedbacks associated with large scale glacial unloading and associated changes in crustal stress regimes
1452 (e.g. Jellinek et al., 2004; Sigmundsson et al., 2010; Huybers and Langmuir, 2009; Cooper et al., 2018).
1453 In particular, crustal loading or unloading of water and ice may influence volcano-climate forcing both
1454 by locally altering eruption frequency as well as the extent to which eruptions are dominated by MWI
1455 processes. Evaluating the climate impacts of hydrovolcanic eruptions relative to purely magmatic eruptions
1456 requires further detailed analysis of the interplay between the coupled processes of conduit ascent and gas
1457 exsolution, fragmentation mechanisms, and the fluid dynamics, microphysics, and chemistry of transport
1458 and dispersal of SO₂, ash, and water in eruption columns.

CONFLICT OF INTEREST STATEMENT

1459 The authors declare that the research was conducted in the absence of any commercial or financial
1460 relationships that could be construed as a potential conflict of interest.

AUTHOR CONTRIBUTIONS

1461 CR was the primary study author, and performed the bulk of code development for the coupled model,
1462 including novel components. CR performed data analysis and the bulk of manuscript writing. AJ was the
1463 primary investigator and holder of funding sources, and provided physical insight for the development of
1464 model equations and extensive discussion and review of the study results, interpretations, and manuscript
1465 writing. SH is the author of the conduit model and provided relevant code with modifications necessary for
1466 this study, and provided code examples and physical insight for the development of the water-entrainment
1467 model, and authored the conduit model components of the manuscript methods section. TA provided code
1468 for the eruption column model and analysis for estimates of stratospheric injection of sulfur dioxide, and
1469 provided advice and oversight of data analysis related to eruption column components of the study.

FUNDING

1470 C.R.R. and A.M.J. were funded through an NSERC Discovery Grant to A.M. Jellinek. SH was supported by
1471 NSF Grant EAR-1348072 to Helge Gonnermann. T.J.A. acknowledges support from the European Union's

1472 Horizon 2020 research and innovation program under the Marie Skłodowska-Curie grant agreement No
1473 835939, and from the Sidney Sussex college through a Junior Research Fellowship.

ACKNOWLEDGMENTS

1474 This research benefited from conversations and insight provided by Josef Dufek, Erin Fitch, Helge
1475 Gonnermann, Gary Glatzmaier and Thomas Jones. We would like to thank Ingo Sonder, Magnús T.
1476 Guðmundsson, and Steve Self for their thoughtful reviews and comments, which greatly improved the
1477 manuscript.

DATA AVAILABILITY STATEMENT

1478 Complete model output for each of the simulation scenarios presented here (see Table 2) are available at
1479 <https://doi.org/10.6084/m9.figshare.19243230.v1>.

REFERENCES

- 1480 Albino, F., Pinel, V., and Sigmundsson, F. (2010). Influence of surface load variations on eruption
1481 likelihood: Application to two Icelandic subglacial volcanoes, Grímsvötn and Katla. *Geophysical*
1482 *Journal International* 181, 1510–1524. doi:10.1111/j.1365-246X.2010.04603.x
- 1483 Ansmann, A., Tesche, M., Seifert, P., Groß, S., Freudenthaler, V., Apituley, A., et al. (2011). Ash and
1484 fine-mode particle mass profiles from EARLINET-AERONET observations over central Europe after
1485 the eruptions of the Eyjafjallajökull volcano in 2010. *Journal of Geophysical Research: Atmospheres*
1486 116, D00U02. doi:10.1029/2010JD015567
- 1487 Aravena, A., Vitturi, M. d. M., Cioni, R., and Neri, A. (2018). Physical constraints for effective magma-
1488 water interaction along volcanic conduits during silicic explosive eruptions. *Geology* 46, 867–870.
1489 doi:10.1130/G45065.1
- 1490 Aubry, T. J., Cerminara, M., and Jellinek, A. M. (2019). Impacts of Climate Change on Volcanic
1491 Stratospheric Injections: Comparison of 1-D and 3-D Plume Model Projections. *Geophysical Research*
1492 *Letters* 46. doi:10.1029/2019GL083975
- 1493 Aubry, T. J., Engwell, S., Bonadonna, C., Carazzo, G., Scollo, S., Van Eaton, A. R., et al. (2021a). The
1494 Independent Volcanic Eruption Source Parameter Archive (IVESPA, version 1.0): A new observational
1495 database to support explosive eruptive column model validation and development. *Journal of Volcanology*
1496 *and Geothermal Research*, 107295doi:10.1016/j.jvolgeores.2021.107295
- 1497 Aubry, T. J. and Jellinek, A. M. (2018). New insights on entrainment and condensation in volcanic plumes:
1498 Constraints from independent observations of explosive eruptions and implications for assessing their
1499 impacts. *Earth and Planetary Science Letters* 490, 132–142. doi:10.1016/j.epsl.2018.03.028
- 1500 Aubry, T. J., Jellinek, A. M., Degruyter, W., Bonadonna, C., Radić, V., Clyne, M., et al. (2016). Impact
1501 of global warming on the rise of volcanic plumes and implications for future volcanic aerosol forcing.
1502 *Journal of Geophysical Research: Atmospheres* 121, 2016JD025405. doi:10.1002/2016JD025405
- 1503 Aubry, T. J., Staunton-Sykes, J., Marshall, L. R., Haywood, J., Abraham, N. L., and Schmidt, A. (2021b).
1504 Climate change modulates the stratospheric volcanic sulfate aerosol lifecycle and radiative forcing from
1505 tropical eruptions. *Nature Communications* 12, 4708. doi:10.1038/s41467-021-24943-7
- 1506 Baldini, J. U. L., Brown, R. J., and McElwaine, J. N. (2015). Was millennial scale climate change during
1507 the Last Glacial triggered by explosive volcanism? *Scientific Reports* 5, 17442. doi:10.1038/srep17442
- 1508 Barberi, F., Cioni, R., Rosi, M., Santacroce, R., Sbrana, A., and Vecchi, R. (1989). Magmatic and
1509 phreatomagmatic phases in explosive eruptions of Vesuvius as deduced by grain-size and component

- 1510 analysis of the pyroclastic deposits. *Journal of Volcanology and Geothermal Research* 38, 287–307.
1511 doi:10.1016/0377-0273(89)90044-9
- 1512 Bercovici, D. and Michaut, C. (2010). Two-phase dynamics of volcanic eruptions: Compaction,
1513 compression and the conditions for choking. *Geophysical Journal International* 182, 843–864.
1514 doi:10.1111/j.1365-246X.2010.04674.x
- 1515 Bluth, G. J. S., Rose, W. I., Sprod, I. E., and Krueger, A. J. (1997). Stratospheric Loading of Sulfur from
1516 Explosive Volcanic Eruptions. *The Journal of Geology* 105, 671–684. doi:10.1086/515972
- 1517 Bonadonna, C., Ernst, G. G. J., and Sparks, R. S. J. (1998). Thickness variations and volume estimates
1518 of tephra fall deposits: The importance of particle Reynolds number. *Journal of Volcanology and
1519 Geothermal Research* 81, 173–187. doi:10.1016/S0377-0273(98)00007-9
- 1520 Bouhifd, M. A., Whittington, A. G., and Richet, P. (2015). Densities and volumes of hydrous silicate melts:
1521 New measurements and predictions. *Chemical Geology* 418, 40–50. doi:10.1016/j.chemgeo.2015.01.012
- 1522 Brown, R. J., Bonadonna, C., and Durant, A. J. (2012). A review of volcanic ash aggregation. *Physics and
1523 Chemistry of the Earth, Parts A/B/C* 45–46, 65–78. doi:10.1016/j.pce.2011.11.001
- 1524 Bursik, M. I., Sparks, R. S. J., Gilbert, J. S., and Carey, S. N. (1992). Sedimentation of tephra by volcanic
1525 plumes: I. Theory and its comparison with a study of the Fogo A plinian deposit, Sao Miguel (Azores).
1526 *Bulletin of Volcanology* 54, 329–344. doi:10.1007/BF00301486
- 1527 Büttner, R., Dellino, P., Raue, H., Sonder, I., and Zimanowski, B. (2006). Stress-induced brittle
1528 fragmentation of magmatic melts: Theory and experiments. *Journal of Geophysical Research: Solid
1529 Earth* 111. doi:10.1029/2005JB003958
- 1530 Büttner, R., Dellino, P., Volpe, L. L., Lorenz, V., and Zimanowski, B. (2002). Thermohydraulic explosions
1531 in phreatomagmatic eruptions as evidenced by the comparison between pyroclasts and products from
1532 Molten Fuel Coolant Interaction experiments. *Journal of Geophysical Research: Solid Earth* 107, ECV
1533 5–1–ECV 5–14. doi:10.1029/2001JB000511
- 1534 Cahalan, R. C. and Dufek, J. (2021). Explosive Submarine Eruptions: The Role of Condensable Gas
1535 Jets in Underwater Eruptions. *Journal of Geophysical Research: Solid Earth* 126, e2020JB020969.
1536 doi:10.1029/2020JB020969
- 1537 Campagnola, S., Romano, C., Mastin, L. G., and Vona, A. (2016). Confort 15 model of conduit dynamics:
1538 Applications to Pantelleria Green Tuff and Etna 122 BC eruptions. *Contributions to Mineralogy and
1539 Petrology* 171, 60. doi:10.1007/s00410-016-1265-5
- 1540 Capra, L. (2006). Abrupt climatic changes as triggering mechanisms of massive volcanic collapses. *Journal
1541 of Volcanology and Geothermal Research* 155, 329–333. doi:10.1016/j.jvolgeores.2006.04.009
- 1542 Carazzo, G. and Jellinek, A. M. (2012). A new view of the dynamics, stability and longevity of volcanic
1543 clouds. *Earth and Planetary Science Letters* 325–326, 39–51. doi:10.1016/j.epsl.2012.01.025
- 1544 Carazzo, G. and Jellinek, A. M. (2013). Particle sedimentation and diffusive convection in volcanic
1545 ash-clouds. *Journal of Geophysical Research: Solid Earth* 118, 1420–1437. doi:10.1002/jgrb.50155
- 1546 Carazzo, G., Kaminski, E., and Tait, S. (2006). The route to self-similarity in turbulent jets and plumes.
1547 *Journal of Fluid Mechanics* 547, 137–148. doi:10.1017/S002211200500683X
- 1548 Carazzo, G., Kaminski, E., and Tait, S. (2008). On the rise of turbulent plumes: Quantitative effects
1549 of variable entrainment for submarine hydrothermal vents, terrestrial and extra terrestrial explosive
1550 volcanism
- 1551 Carey, R. J., Houghton, B. F., and Thordarson, T. (2009). Abrupt shifts between wet and dry phases
1552 of the 1875 eruption of Askja Volcano: Microscopic evidence for macroscopic dynamics. *Journal of
1553 Volcanology and Geothermal Research* 184, 256–270. doi:10.1016/j.jvolgeores.2009.04.003

- 1554 Cas, R. and Wright, J. (1987). *Volcanic Successions Modern and Ancient: A Geological Approach to*
1555 *Processes, Products and Successions* (Springer Science & Business Media)
- 1556 Cas, R. A. F. and Simmons, J. M. (2018). Why Deep-Water Eruptions Are So Different From Subaerial
1557 Eruptions. *Frontiers in Earth Science* 6. doi:10.3389/feart.2018.00198
- 1558 Cerminara, M., Esposti Ongaro, T., and Berselli, L. C. (2016). ASHEE-1.0: A compressible,
1559 equilibrium–Eulerian model for volcanic ash plumes. *Geoscientific Model Development* 9,
1560 697–730. doi:10.5194/gmd-9-697-2016
- 1561 Cole, P. D., Queiroz, G., Wallenstein, N., Gaspar, J. L., Duncan, A. M., and Guest, J. E. (1995). An historic
1562 subplinian/phreatomagmatic eruption: The 1630 AD eruption of Furnas volcano, Sa~o Miguel, Azores.
1563 *Journal of Volcanology and Geothermal Research* 69, 117–135. doi:10.1016/0377-0273(95)00033-X
- 1564 Colucci, S., de' Michieli Vitturi, M., Neri, A., and Palladino, D. M. (2014). An integrated model of magma
1565 chamber, conduit and column for the analysis of sustained explosive eruptions. *Earth and Planetary*
1566 *Science Letters* 404, 98–110. doi:10.1016/j.epsl.2014.07.034
- 1567 Cooper, C. L., Swindles, G. T., Savov, I. P., Schmidt, A., and Bacon, K. L. (2018). Evaluating the
1568 relationship between climate change and volcanism. *Earth-Science Reviews* 177, 238–247. doi:10.1016/
1569 j.earscirev.2017.11.009
- 1570 Costa, A., Pioli, L., and Bonadonna, C. (2016). Assessing tephra total grain-size distribution: Insights from
1571 field data analysis. *Earth and Planetary Science Letters* 443, 90–107. doi:10.1016/j.epsl.2016.02.040
- 1572 de' Michieli Vitturi, M. and Aravena, Á. (2021). Chapter 6 - Numerical modeling of magma ascent
1573 dynamics. In *Forecasting and Planning for Volcanic Hazards, Risks, and Disasters*, ed. P. Papale
1574 (Elsevier), vol. 2 of *Hazards and Disasters*. 239–284. doi:10.1016/B978-0-12-818082-2.00006-8
- 1575 Degruyter, W. and Bonadonna, C. (2012). Improving on mass flow rate estimates of volcanic eruptions.
1576 *Geophysical Research Letters* 39. doi:10.1029/2012GL052566
- 1577 Degruyter, W. and Bonadonna, C. (2013). Impact of wind on the condition for column collapse of volcanic
1578 plumes. *Earth and Planetary Science Letters* 377–378, 218–226. doi:10.1016/j.epsl.2013.06.041
- 1579 Dingwell, D. B. (1998). The glass transition in hydrous granitic melts. *Physics of the Earth and Planetary*
1580 *Interiors* 107, 1–8. doi:10.1016/S0031-9201(97)00119-2
- 1581 Dufek, J., Manga, M., and Staedter, M. (2007). Littoral blasts: Pumice-water heat transfer and the conditions
1582 for steam explosions when pyroclastic flows enter the ocean. *Journal of Geophysical Research: Solid*
1583 *Earth* 112, B11201. doi:10.1029/2006JB004910
- 1584 Durant, A. J., Rose, W. I., Sarna-Wojcicki, A. M., Carey, S., and Volentik, A. C. M. (2009). Hydrometeor-
1585 enhanced tephra sedimentation: Constraints from the 18 May 1980 eruption of Mount St. Helens. *Journal*
1586 *of Geophysical Research: Solid Earth* 114. doi:10.1029/2008JB005756
- 1587 Dürig, T., Sonder, I., Zimanowski, B., Beyrichen, H., and Büttner, R. (2012). Generation of volcanic ash
1588 by basaltic volcanism. *Journal of Geophysical Research: Solid Earth* 117. doi:10.1029/2011JB008628
- 1589 Dürig, T., White, J. D. L., Murch, A. P., Zimanowski, B., Büttner, R., Mele, D., et al. (2020a). Deep-sea
1590 eruptions boosted by induced fuel–coolant explosions. *Nature Geoscience* 13, 498–503. doi:10.1038/
1591 s41561-020-0603-4
- 1592 Dürig, T., White, J. D. L., Zimanowski, B., Büttner, R., Murch, A., and Carey, R. J. (2020b). Deep-sea
1593 fragmentation style of Havre revealed by dendrogrammatic analyses of particle morphometry. *Bulletin*
1594 *of Volcanology* 82, 67. doi:10.1007/s00445-020-01408-1
- 1595 Elsworth, D., Voight, B., Thompson, G., and Young, S. (2004). Thermal-hydrologic mechanism for
1596 rainfall-triggered collapse of lava domes. *Geology* 32, 969–972. doi:10.1130/G20730.1
- 1597 Farquharson, J. I. and Amelung, F. (2020). Extreme rainfall triggered the 2018 rift eruption at Kīlauea
1598 Volcano. *Nature* 580, 491–495. doi:10.1038/s41586-020-2172-5

- 1599 Fasullo, J. T., Tomas, R., Stevenson, S., Otto-Bliesner, B., Brady, E., and Wahl, E. (2017). The amplifying
1600 influence of increased ocean stratification on a future year without a summer. *Nature Communications* 8,
1601 1236. doi:10.1038/s41467-017-01302-z
- 1602 Fee, D., Lyons, J., Haney, M., Wech, A., Waythomas, C., Diefenbach, A. K., et al. (2020). Seismo-acoustic
1603 evidence for vent drying during shallow submarine eruptions at Bogoslof volcano, Alaska. *Bulletin of*
1604 *Volcanology* 82, 2. doi:10.1007/s00445-019-1326-5
- 1605 Fisher, R. V. and Schmincke, H.-U. (2012). *Pyroclastic Rocks* (Springer Science & Business Media)
- 1606 Fitch, E. P. and Fagents, S. A. (2020). Using the characteristics of rootless cone deposits to estimate
1607 the energetics of explosive lava–water interactions. *Bulletin of Volcanology* 82, 83. doi:10.1007/
1608 s00445-020-01422-3
- 1609 Gilchrist, J. T. and Jellinek, A. M. (2021). Sediment waves and the gravitational stability of volcanic jets.
1610 *Bulletin of Volcanology* 83, 64. doi:10.1007/s00445-021-01472-1
- 1611 Giordano, D., Nichols, A. R. L., and Dingwell, D. B. (2005). Glass transition temperatures of natural
1612 hydrous melts: A relationship with shear viscosity and implications for the welding process. *Journal of*
1613 *Volcanology and Geothermal Research* 142, 105–118. doi:10.1016/j.jvolgeores.2004.10.015
- 1614 Girault, F., Carazzo, G., Tait, S., Ferrucci, F., and Kaminski, É. (2014). The effect of total grain-size
1615 distribution on the dynamics of turbulent volcanic plumes. *Earth and Planetary Science Letters* 394,
1616 124–134. doi:10.1016/j.epsl.2014.03.021
- 1617 Girault, F., Carazzo, G., Tait, S., and Kaminski, E. (2016). Combined effects of total grain-size distribution
1618 and crosswind on the rise of eruptive volcanic columns. *Journal of Volcanology and Geothermal*
1619 *Research* 326, 103–113. doi:10.1016/j.jvolgeores.2015.11.007
- 1620 Glaze, L. S., Baloga, S. M., and Wilson, L. (1997). Transport of atmospheric water vapor by volcanic
1621 eruption columns. *Journal of Geophysical Research: Atmospheres* 102, 6099–6108. doi:10.1029/
1622 96JD03125
- 1623 [Dataset] Global Volcanism Program (2013). South Sarigan Seamount (284193)
- 1624 Gonnermann, H. M. (2015). Magma Fragmentation. *Annual Review of Earth and Planetary Sciences* 43,
1625 431–458. doi:10.1146/annurev-earth-060614-105206
- 1626 Gonnermann, H. M. and Manga, M. (2007). The Fluid Mechanics Inside a Volcano. *Annual Review of*
1627 *Fluid Mechanics* 39, 321–356. doi:10.1146/annurev.fluid.39.050905.110207
- 1628 Gonnermann, H. M. and Manga, M. (2013). Dynamics of magma ascent in the volcanic conduit. In
1629 *Modeling Volcanic Processes: The Physics and Mathematics of Volcanism*, eds. R. M. C. Lopes,
1630 S. A. Fagents, and T. K. P. Gregg (Cambridge: Cambridge University Press). 55–84. doi:10.1017/
1631 CBO9781139021562.004
- 1632 Green, D. N., Evers, L. G., Fee, D., Matoza, R. S., Snellen, M., Smets, P., et al. (2013). Hydroacoustic,
1633 infrasonic and seismic monitoring of the submarine eruptive activity and sub-aerial plume generation at
1634 South Sarigan, May 2010. *Journal of Volcanology and Geothermal Research* 257, 31–43. doi:10.1016/j.
1635 jvolgeores.2013.03.006
- 1636 Gudmundsson, M. T., Pálsson, F., Thordarson, T., Hoskuldsson, A., Larsen, G., Hognadóttir, T., et al.
1637 (2014). Water/magma mass fractions in phreatomagmatic eruption plumes - constraints from the
1638 Grímsvötn 2011 eruption. *AGU Fall Meeting Abstracts* 11, V11B–4718
- 1639 Gudmundsson, M. T., Sigmundsson, F., Björnsson, H., and Högnadóttir, T. (2004). The 1996 eruption at
1640 Gjálp, Vatnajökull ice cap, Iceland: Efficiency of heat transfer, ice deformation and subglacial water
1641 pressure. *Bulletin of Volcanology* 66, 46–65. doi:10.1007/s00445-003-0295-9
- 1642 Gudmundsson, M. T., Thordarson, T., Höskuldsson, Á., Larsen, G., Björnsson, H., Prata, F. J., et al. (2012).
1643 Ash generation and distribution from the April-May 2010 eruption of Eyjafjallajökull, Iceland. *Scientific*

- 1644 *Reports* 2, 572. doi:10.1038/srep00572
- 1645 Hajimirza, S., Gonnermann, H. M., and Gardner, J. E. (2021). Reconciling bubble nucleation in explosive
1646 eruptions with geospeedometers. *Nature Communications* 12, 283. doi:10.1038/s41467-020-20541-1
- 1647 Hajimirza, S., Gonnermann, H. M., Gardner, J. E., and Giachetti, T. (2019). Predicting Homogeneous
1648 Bubble Nucleation in Rhyolite. *Journal of Geophysical Research: Solid Earth* 124, 2395–2416.
1649 doi:10.1029/2018JB015891
- 1650 Hajimirza, S., Jones, T. J., Moreland, W. M., Gonnermann, H. M., and Thordarson, T. (In press).
1651 Quantifying the water-to-melt mass ratio and its impact on eruption plumes during explosive
1652 hydromagmatic eruptions. *Geochemistry, Geophysics, Geosystems* 23, e2021GC010160. doi:10.
1653 1029/2021GC010160
- 1654 Hersbach, H., Bell, B., Berrisford, P., Hirahara, S., Horányi, A., Muñoz-Sabater, J., et al. (2020). The
1655 ERA5 global reanalysis. *Quarterly Journal of the Royal Meteorological Society* 146, 1999–2049.
1656 doi:10.1002/qj.3803
- 1657 Holloway, J. R. (1977). Fugacity and Activity of Molecular Species in Supercritical Fluids. In
1658 *Thermodynamics in Geology*, ed. D. G. Fraser (Dordrecht: Springer Netherlands), NATO Advanced
1659 Study Institutes Series, 161–181. doi:10.1007/978-94-010-1252-2_9
- 1660 Houghton, B. and Carey, R. J. (2015). Chapter 34 - Pyroclastic Fall Deposits. In *The Encyclopedia of*
1661 *Volcanoes (Second Edition)*, ed. H. Sigurdsson (Amsterdam: Academic Press). 599–616. doi:10.1016/
1662 B978-0-12-385938-9.00034-1
- 1663 Houghton, B., White, J. D. L., and Van Eaton, A. R. (2015). Chapter 30 - Phreatomagmatic and Related
1664 Eruption Styles. In *The Encyclopedia of Volcanoes (Second Edition)*, ed. H. Sigurdsson (Amsterdam:
1665 Academic Press). 537–552. doi:10.1016/B978-0-12-385938-9.00030-4
- 1666 Houghton, B. F. and Carey, R. J. (2019). Physical constraints for effective magma-water interaction along
1667 volcanic conduits during silicic explosive eruptions: COMMENT. *Geology* 47, e461–e461. doi:10/c84b
- 1668 Houghton, B. F. and Wilson, C. J. N. (1989). A vesicularity index for pyroclastic deposits. *Bulletin of*
1669 *Volcanology* 51, 451–462. doi:10.1007/BF01078811
- 1670 Huybers, P. and Langmuir, C. (2009). Feedback between deglaciation, volcanism, and atmospheric CO₂.
1671 *Earth and Planetary Science Letters* 286, 479–491. doi:10.1016/j.epsl.2009.07.014
- 1672 Jellinek, A. M., Manga, M., and Saar, M. O. (2004). Did melting glaciers cause volcanic eruptions in
1673 eastern California? Probing the mechanics of dike formation. *Journal of Geophysical Research: Solid*
1674 *Earth* 109. doi:10.1029/2004JB002978
- 1675 Jones, T., Gonnermann, H., Moreland, W., and Thordarson, T. (2019). Quantifying water entrainment in
1676 volcanic jets. In *Geophysical Research Abstracts*. vol. 21, 1
- 1677 Jull, M. and McKenzie, D. (1996). The effect of deglaciation on mantle melting beneath Iceland. *Journal*
1678 *of Geophysical Research: Solid Earth* 101, 21815–21828. doi:10.1029/96JB01308
- 1679 Junglas, P. (2009). Implementation of the IAPWS-95 Standard for Use in Thermodynamics Lectures 25,
1680 3–10
- 1681 Kaminski, E. and Jaupart, C. (1998). The size distribution of pyroclasts and the fragmentation sequence
1682 in explosive volcanic eruptions. *Journal of Geophysical Research: Solid Earth* 103, 29759–29779.
1683 doi:10.1029/98JB02795
- 1684 Kaminski, E., Tait, S., and Carazzo, G. (2005). Turbulent entrainment in jets with arbitrary buoyancy.
1685 *Journal of Fluid Mechanics* 526, 361–376. doi:10.1017/S0022112004003209
- 1686 Kokelaar, P. (1986). Magma-water interactions in subaqueous and emergent basaltic. *Bulletin of*
1687 *Volcanology* 48, 275–289. doi:10.1007/BF01081756

- 1688 Kotsovinos, N. E. (2000). Axisymmetric Submerged Intrusion in Stratified Fluid. *Journal of Hydraulic*
1689 *Engineering* 126, 446–456. doi:10.1061/(ASCE)0733-9429(2000)126:6(446)
- 1690 Koyaguchi, T. (2005). An analytical study for 1-dimensional steady flow in volcanic conduits. *Journal of*
1691 *Volcanology and Geothermal Research* 143, 29–52. doi:10.1016/j.jvolgeores.2004.09.009
- 1692 Koyaguchi, T. and Woods, A. W. (1996). On the formation of eruption columns following explosive
1693 mixing of magma and surface-water. *Journal of Geophysical Research: Solid Earth* 101, 5561–5574.
1694 doi:10.1029/95JB01687
- 1695 Kremser, S., Thomason, L. W., von Hobe, M., Hermann, M., Deshler, T., Timmreck, C., et al. (2016).
1696 Stratospheric aerosol-Observations, processes, and impact on climate: Stratospheric Aerosol. *Reviews of*
1697 *Geophysics* 54, 278–335. doi:10.1002/2015RG000511
- 1698 Krishnamohan, K.-P. S.-P., Bala, G., Cao, L., Duan, L., and Caldeira, K. (2019). Climate system response
1699 to stratospheric sulfate aerosols: Sensitivity to altitude of aerosol layer. *Earth System Dynamics* 10,
1700 885–900. doi:10.5194/esd-10-885-2019
- 1701 Lacis, A. (2015). Volcanic aerosol radiative properties. *Past Global Change Magazine* 23, 50–51.
1702 doi:10.22498/pages.23.2.50
- 1703 Lee, C.-T. and Dee, S. (2019). Does volcanism cause warming or cooling? *Geology* 47, 687–688.
1704 doi:10.1130/focus072019.1
- 1705 LeGrande, A. N., Tsigaridis, K., and Bauer, S. E. (2016). Role of atmospheric chemistry in the climate
1706 impacts of stratospheric volcanic injections. *Nature Geoscience* 9, 652–655. doi:10.1038/ngeo2771
- 1707 Lherm, V. and Jellinek, A. M. (2019). Experimental constraints on the distinct effects of ash, lapilli,
1708 and larger pyroclasts on entrainment and mixing in volcanic plumes. *Bulletin of Volcanology* 81, 73.
1709 doi:10.1007/s00445-019-1329-2
- 1710 Linden, P. F. (1979). Mixing in stratified fluids. *Geophysical & Astrophysical Fluid Dynamics* 13, 3–23.
1711 doi:10.1080/03091927908243758
- 1712 Liu, E. J. (2016). *The Generation of Volcanic Ash during Basaltic Hydromagmatic Eruptions : From*
1713 *Fragmentation to Resuspension*. Ph.D. thesis, University of Bristol
- 1714 Liu, E. J., Cashman, K. V., Rust, A. C., and Gislason, S. R. (2015). The role of bubbles in generating fine
1715 ash during hydromagmatic eruptions. *Geology* 43, 239–242. doi:10.1130/G36336.1
- 1716 Liu, E. J., Cashman, K. V., Rust, A. C., and Höskuldsson, A. (2017). Contrasting mechanisms of magma
1717 fragmentation during coeval magmatic and hydromagmatic activity: The Hverfjall Fires fissure eruption,
1718 Iceland. *Bulletin of Volcanology* 79, 68. doi:10.1007/s00445-017-1150-8
- 1719 Liu, Y., Zhang, Y., and Behrens, H. (2005). Solubility of H₂O in rhyolitic melts at low pressures and a
1720 new empirical model for mixed H₂O–CO₂ solubility in rhyolitic melts. *Journal of Volcanology and*
1721 *Geothermal Research* 143, 219–235. doi:10.1016/j.jvolgeores.2004.09.019
- 1722 Lyons, J. J., Haney, M. M., Fee, D., Wech, A. G., and Waythomas, C. F. (2019). Infrasound from
1723 giant bubbles during explosive submarine eruptions. *Nature Geoscience* 12, 952–958. doi:10.1038/
1724 s41561-019-0461-0
- 1725 Magnússon, E., Gudmundsson, M. T., Roberts, M. J., Sigurðsson, G., Höskuldsson, F., and Oddsson,
1726 B. (2012). Ice-volcano interactions during the 2010 Eyjafjallajökull eruption, as revealed by airborne
1727 imaging radar. *Journal of Geophysical Research: Solid Earth* 117. doi:10.1029/2012JB009250
- 1728 Manga, M., Fauria, K. E., Lin, C., Mitchell, S. J., Jones, M., Conway, C. E., et al. (2018). The pumice
1729 raft-forming 2012 Havre submarine eruption was effusive. *Earth and Planetary Science Letters* 489,
1730 49–58. doi:10.1016/j.epsl.2018.02.025
- 1731 Mann, M. E., Steinman, B. A., Brouillette, D. J., and Miller, S. K. (2021). Multidecadal climate oscillations
1732 during the past millennium driven by volcanic forcing. *Science* 371, 1014–1019. doi:10.1126/science.

- 1733 abc5810
- 1734 Manzella, I., Bonadonna, C., Phillips, J. C., and Monnard, H. (2015). The role of gravitational instabilities
1735 in deposition of volcanic ash. *Geology* 43, 211–214. doi:10.1130/G36252.1
- 1736 Marshall, L., Johnson, J. S., Mann, G. W., Lee, L., Dhomse, S. S., Regayre, L., et al. (2019). Exploring
1737 How Eruption Source Parameters Affect Volcanic Radiative Forcing Using Statistical Emulation. *Journal*
1738 *of Geophysical Research: Atmospheres* 124, 964–985. doi:10.1029/2018JD028675
- 1739 Massol, H. and Koyaguchi, T. (2005). The effect of magma flow on nucleation of gas bubbles in a volcanic
1740 conduit. *Journal of Volcanology and Geothermal Research* 143, 69–88. doi:10.1016/j.jvolgeores.2004.
1741 09.011
- 1742 Mastin, L. G. (2007a). Generation of fine hydromagmatic ash by growth and disintegration of glassy rinds.
1743 *Journal of Geophysical Research: Solid Earth* 112. doi:10.1029/2005JB003883
- 1744 Mastin, L. G. (2007b). A user-friendly one-dimensional model for wet volcanic plumes. *Geochemistry,*
1745 *Geophysics, Geosystems* 8. doi:10.1029/2006GC001455
- 1746 Mastin, L. G. and Ghiorso, M. S. (2000). *A Numerical Program for Steady-State Flow of Magma-Gas*
1747 *Mixtures Through Vertical Eruptive Conduits*. Tech. rep., Department of the Interior, Washington DC
- 1748 Mastin, L. G. and Witter, J. B. (2000). The hazards of eruptions through lakes and seawater. *Journal of*
1749 *Volcanology and Geothermal Research* 97, 195–214. doi:10.1016/S0377-0273(99)00174-2
- 1750 McGimsey, R. G., Neal, C. A., Searcy, C. K., Camacho, J. T., Aydlett, W. B., Embley, R. W., et al. (2010).
1751 The May 2010 submarine eruption from South Sarigan seamount, Northern Mariana Islands 2010,
1752 T11E–07
- 1753 Michaut, C., Ricard, Y., Bercovici, D., and Sparks, R. S. J. (2013). Eruption cyclicality at silicic volcanoes
1754 potentially caused by magmatic gas waves. *Nature Geoscience* 6, 856–860. doi:10.1038/ngeo1928
- 1755 Moitra, P., Sonder, I., and Valentine, G. A. (2020). The role of external water on rapid cooling and
1756 fragmentation of magma. *Earth and Planetary Science Letters* 537, 116194. doi:10.1016/j.epsl.2020.
1757 116194
- 1758 Moreland, W. (2017). *Explosive Activity in Flood Lava Eruptions: A Case Study of the 10th Century Eldgjá*
1759 *Eruption, Iceland*. Ph.D. thesis, University of Iceland, School of Engineering and Natural Sciences,
1760 Faculty of Earth Sciences, Reykjavík, Iceland
- 1761 Moreland, W. M., Thordarson, T., Houghton, B. F., and Larsen, G. (2019). Driving mechanisms of
1762 subaerial and subglacial explosive episodes during the 10th century Eldgjá fissure eruption, southern
1763 Iceland. *Volcanica* 2, 129–150. doi:10.30909/vol.02.02.129150
- 1764 Morton, B. R., Taylor, G. I., and Turner, J. S. (1956). Turbulent gravitational convection from maintained
1765 and instantaneous sources. *Proceedings of the Royal Society of London. Series A. Mathematical and*
1766 *Physical Sciences* 234, 1–23. doi:10.1098/rspa.1956.0011
- 1767 Murch, A. P., White, J. D. L., and Carey, R. J. (2019). Characteristics and Deposit Stratigraphy of
1768 Submarine-Erupted Silicic Ash, Havre Volcano, Kermadec Arc, New Zealand. *Frontiers in Earth*
1769 *Science* 7, 1. doi:10.3389/feart.2019.00001
- 1770 Nelson, C. S. and Lister, G. S. (1995). Surficial bottom sediments of Lake Taupo, New Zealand: Texture,
1771 composition, provenance, and sedimentation rates. *New Zealand Journal of Geology and Geophysics* 38,
1772 61–79. doi:10.1080/00288306.1995.9514639
- 1773 Neri, A., Di Muro, A., and Rosi, M. (2002). Mass partition during collapsing and transitional columns by
1774 using numerical simulations. *Journal of Volcanology and Geothermal Research* 115, 1–18. doi:10.1016/
1775 S0377-0273(01)00304-3
- 1776 Niemeier, U., Timmreck, C., Graf, H.-F., Kinne, S., Rast, S., and Self, S. (2009). Initial fate of fine
1777 ash and sulfur from large volcanic eruptions. *Atmospheric Chemistry and Physics* 9, 9043–9057.

- 1778 doi:10.5194/acp-9-9043-2009
- 1779 Ogden, D. E., Wohletz, K. H., Glatzmaier, G. A., and Brodsky, E. E. (2008). Numerical simulations of
1780 volcanic jets: Importance of vent overpressure. *Journal of Geophysical Research: Solid Earth* 113,
1781 B02204. doi:10.1029/2007JB005133
- 1782 Papale, P. (1999). Strain-induced magma fragmentation in explosive eruptions. *Nature* 397, 425–428.
1783 doi:10.1038/17109
- 1784 Patel, A., Manga, M., Carey, R. J., and Degruyter, W. (2013). Effects of thermal quenching on mechanical
1785 properties of pyroclasts. *Journal of Volcanology and Geothermal Research* 258, 24–30. doi:10.1016/j.
1786 jvolgeores.2013.04.001
- 1787 Prata, F., Woodhouse, M., Huppert, H. E., Prata, A., Thordarson, T., and Carn, S. (2017). Atmospheric
1788 processes affecting the separation of volcanic ash and SO₂ in volcanic eruptions: Inferences from the
1789 May 2011 Grímsvötn eruption. *Atmospheric Chemistry and Physics* 17, 10709–10732
- 1790 Robock, A. (2000). Volcanic eruptions and climate. *Reviews of Geophysics* 38, 191–219. doi:10.1029/
1791 1998RG000054
- 1792 Rose, W. I. (1977). Scavenging of volcanic aerosol by ash: Atmospheric and volcanologic implications.
1793 *Geology* 5, 621–624. doi:10.1130/0091-7613(1977)5<621:SOVABA>2.0.CO;2
- 1794 Rose, W. I., Bluth, G. J. S., Schneider, D. J., Ernst, G. G. J., Riley, C. M., Henderson, L. J., et al.
1795 (2001). Observations of Volcanic Clouds in Their First Few Days of Atmospheric Residence: The
1796 1992 Eruptions of Crater Peak, Mount Spurr Volcano, Alaska. *The Journal of Geology* 109, 677–694.
1797 doi:10.1086/323189
- 1798 Rose, W. I., Delene, D. J., Schneider, D. J., Bluth, G. J. S., Krueger, A. J., Sprod, I., et al. (1995). Ice in
1799 the 1994 Rabaul eruption cloud: Implications for volcano hazard and atmospheric effects. *Nature* 375,
1800 477–479. doi:10.1038/375477a0
- 1801 Rust, A. C. and Cashman, K. V. (2011). Permeability controls on expansion and size distributions of
1802 pyroclasts. *Journal of Geophysical Research: Solid Earth* 116. doi:10.1029/2011JB008494
- 1803 Saffaraval, F. and Solovitz, S. A. (2012). Near-exit flow physics of a moderately overpressured jet. *Physics*
1804 *of Fluids* 24, 086101. doi:10.1063/1.4745005
- 1805 Saffaraval, F., Solovitz, S. A., Ogden, D. E., and Mastin, L. G. (2012). Impact of reduced near-field
1806 entrainment of overpressured volcanic jets on plume development. *Journal of Geophysical Research:*
1807 *Solid Earth* 117. doi:10.1029/2011JB008862
- 1808 Santer, B. D., Bonfils, C., Painter, J. F., Zelinka, M. D., Mears, C., Solomon, S., et al. (2014). Volcanic
1809 contribution to decadal changes in tropospheric temperature. *Nature Geoscience* 7, 185–189. doi:10.
1810 1038/ngeo2098
- 1811 Schleussner, C. F. and Feulner, G. (2013). A volcanically triggered regime shift in the subpolar North
1812 Atlantic Ocean as a possible origin of the Little Ice Age. *Climate of the Past* 9, 1321–1330. doi:10.5194/
1813 cp-9-1321-2013
- 1814 Schmauss, D. and Keppler, H. (2014). Adsorption of sulfur dioxide on volcanic ashes. *American*
1815 *Mineralogist* 99, 1085–1094. doi:10.2138/am.2014.4656
- 1816 Schmid, A., Sonder, I., Seegelken, R., Zimanowski, B., Büttner, R., Gudmundsson, M. T., et al. (2010).
1817 Experiments on the heat discharge at the dynamic magma-water-interface. *Geophysical Research Letters*
1818 37. doi:10.1029/2010GL044963
- 1819 Schmidt, A., Carslaw, K. S., Mann, G. W., Rap, A., Pringle, K. J., Spracklen, D. V., et al. (2012).
1820 Importance of tropospheric volcanic aerosol for indirect radiative forcing of climate. *Atmospheric*
1821 *Chemistry and Physics* 12, 7321–7339. doi:10.5194/acp-12-7321-2012

- 1822 Self, S. and Sparks, R. S. J. (1978). Characteristics of widespread pyroclastic deposits formed by the
1823 interaction of silicic magma and water. *Bulletin Volcanologique* 41, 196. doi:10.1007/BF02597223
- 1824 Shea, T. (2017). Bubble nucleation in magmas: A dominantly heterogeneous process? *Journal of*
1825 *Volcanology and Geothermal Research* 343, 155–170. doi:10.1016/j.jvolgeores.2017.06.025
- 1826 Sigl, M., Winstrup, M., McConnell, J. R., Welten, K. C., Plunkett, G., Ludlow, F., et al. (2015). Timing
1827 and climate forcing of volcanic eruptions for the past 2,500 years. *Nature* 523, 543–549. doi:10.1038/
1828 nature14565
- 1829 Sigmarsson, O., Haddadi, B., Carn, S., Moune, S., Gudnason, J., Yang, K., et al. (2013). The sulfur budget
1830 of the 2011 Grímsvötn eruption, Iceland. *Geophysical Research Letters* 40, 6095–6100. doi:10.1002/
1831 2013GL057760
- 1832 Sigmundsson, F., Pinel, V., Lund, B., Albino, F., Pagli, C., Geirsson, H., et al. (2010). Climate effects
1833 on volcanism: Influence on magmatic systems of loading and unloading from ice mass variations, with
1834 examples from Iceland. *Philosophical Transactions of the Royal Society A: Mathematical, Physical and*
1835 *Engineering Sciences* 368, 2519–2534. doi:10.1098/rsta.2010.0042
- 1836 Smellie, J. L. and Edwards, B. R. (2016). *Glaciovolcanism on Earth and Mars* (Cambridge University
1837 Press)
- 1838 Solomon, S., Daniel, J. S., Neely, R. R., Vernier, J.-P., Dutton, E. G., and Thomason, L. W. (2011). The
1839 Persistently Variable “Background” Stratospheric Aerosol Layer and Global Climate Change. *Science*
1840 333, 866–870. doi:10.1126/science.1206027
- 1841 Sonder, I., Schmid, A., Seegelken, R., Zimanowski, B., and Büttner, R. (2011). Heat source or heat sink:
1842 What dominates behavior of non-explosive magma-water interaction? *Journal of Geophysical Research:*
1843 *Solid Earth* 116. doi:10.1029/2011JB008280
- 1844 Soreghan, G. S., Soreghan, M. J., and Heavens, N. G. (2019). Explosive volcanism as a key driver of the
1845 late Paleozoic ice age. *Geology* 47, 600–604. doi:10.1130/G46349.1
- 1846 Starostin, A. B., Barmin, A. A., and Melnik, O. E. (2005). A transient model for explosive and
1847 phreatomagmatic eruptions. *Journal of Volcanology and Geothermal Research* 143, 133–151.
1848 doi:10.1016/j.jvolgeores.2004.09.014
- 1849 Staunton-Sykes, J., Aubry, T. J., Shin, Y. M., Weber, J., Marshall, L. R., Luke Abraham, N., et al. (2021).
1850 Co-emission of volcanic sulfur and halogens amplifies volcanic effective radiative forcing. *Atmospheric*
1851 *Chemistry and Physics* 21, 9009–9029. doi:10.5194/acp-21-9009-2021
- 1852 Telling, J., Dufek, J., and Shaikh, A. (2013). Ash aggregation in explosive volcanic eruptions. *Geophysical*
1853 *Research Letters* 40, 2355–2360. doi:10.1002/grl.50376
- 1854 Textor, C., Graf, H.-F., Herzog, M., and Oberhuber, J. M. (2003). Injection of gases into the stratosphere
1855 by explosive volcanic eruptions. *Journal of Geophysical Research: Atmospheres* 108, 4606. doi:10.
1856 1029/2002JD002987
- 1857 Timmreck, C. (2012). Modeling the climatic effects of large explosive volcanic eruptions. *Wiley*
1858 *Interdisciplinary Reviews: Climate Change* 3, 545–564. doi:10.1002/wcc.192
- 1859 Toohey, M., Krüger, K., Schmidt, H., Timmreck, C., Sigl, M., Stoffel, M., et al. (2019). Disproportionately
1860 strong climate forcing from extratropical explosive volcanic eruptions. *Nature Geoscience* 12, 100.
1861 doi:10.1038/s41561-018-0286-2
- 1862 Toohey, M., Krüger, K., Sigl, M., Stordal, F., and Svensen, H. (2016). Climatic and societal impacts of a
1863 volcanic double event at the dawn of the Middle Ages. *Climatic Change* 136, 401–412. doi:10.1007/
1864 s10584-016-1648-7
- 1865 Turner, J. S. (1986). Turbulent entrainment: The development of the entrainment assumption, and
1866 its application to geophysical flows. *Journal of Fluid Mechanics* 173, 431–471. doi:10.1017/

- 1867 S0022112086001222
- 1868 Van Eaton, A. R., Herzog, M., Wilson, C. J. N., and McGregor, J. (2012). Ascent dynamics of large
1869 phreatomagmatic eruption clouds: The role of microphysics. *Journal of Geophysical Research: Solid*
1870 *Earth* 117, B03203. doi:10.1029/2011JB008892
- 1871 Van Eaton, A. R., Mastin, L. G., Herzog, M., Schwaiger, H. F., Schneider, D. J., Wallace, K. L., et al.
1872 (2015). Hail formation triggers rapid ash aggregation in volcanic plumes. *Nature Communications* 6,
1873 7860. doi:10.1038/ncomms8860
- 1874 van Otterloo, J., Cas, R. A. F., and Scutter, C. R. (2015). The fracture behaviour of volcanic glass and
1875 relevance to quench fragmentation during formation of hyaloclastite and phreatomagmatism. *Earth-*
1876 *Science Reviews* 151, 79–116. doi:10.1016/j.earscirev.2015.10.003
- 1877 Walker, G. P. L. (1973). Explosive volcanic eruptions — a new classification scheme. *Geologische*
1878 *Rundschau* 62, 431–446. doi:10.1007/BF01840108
- 1879 Walker, G. P. L. (1981). Characteristics of two phreatoplinian ashes, and their water-flushed origin. *Journal*
1880 *of Volcanology and Geothermal Research* 9, 395–407. doi:10.1016/0377-0273(81)90046-9
- 1881 Wallace, P. J., Plank, T., Edmonds, M., and Hauri, E. H. (2015). Chapter 7 - Volatiles in Magmas. In *The*
1882 *Encyclopedia of Volcanoes (Second Edition)*, ed. H. Sigurdsson (Amsterdam: Academic Press). 163–183.
1883 doi:10.1016/B978-0-12-385938-9.00007-9
- 1884 Watt, S. F. L., Pyle, D. M., and Mather, T. A. (2013). The volcanic response to deglaciation: Evidence
1885 from glaciated arcs and a reassessment of global eruption records. *Earth-Science Reviews* 122, 77–102.
1886 doi:10.1016/j.earscirev.2013.03.007
- 1887 Waythomas, C. F., Angeli, K., and Wessels, R. L. (2020). Evolution of the submarine–subaerial edifice of
1888 Bogoslof volcano, Alaska, during its 2016–2017 eruption based on analysis of satellite imagery. *Bulletin*
1889 *of Volcanology* 82, 21. doi:10.1007/s00445-020-1363-0
- 1890 Wilson, C. J. N. (2001). The 26.5ka Oruanui eruption, New Zealand: An introduction and overview.
1891 *Journal of Volcanology and Geothermal Research* 112, 133–174. doi:10.1016/S0377-0273(01)00239-6
- 1892 Wilson, C. J. N. and Walker, G. P. L. (1985). The Taupo eruption, New Zealand I. General aspects.
1893 *Philosophical Transactions of the Royal Society of London. Series A, Mathematical and Physical*
1894 *Sciences* 314, 199–228. doi:10.1098/rsta.1985.0019
- 1895 Wilson, L., Sparks, R. S. J., and Walker, G. P. L. (1980). Explosive volcanic eruptions — IV. The
1896 control of magma properties and conduit geometry on eruption column behaviour. *Geophysical Journal*
1897 *International* 63, 117–148. doi:10.1111/j.1365-246X.1980.tb02613.x
- 1898 Wohletz, K. (1983). Mechanisms of hydrovolcanic pyroclast formation: Grain-size, scanning electron
1899 microscopy, and experimental studies. *Journal of Volcanology and Geothermal Research* 17, 31–63.
1900 doi:10.1016/0377-0273(83)90061-6
- 1901 Wohletz, K., Zimanowski, B., and Büttner, R. (2013). Magma–water interactions. In *Modeling Volcanic*
1902 *Processes: The Physics and Mathematics of Volcanism* (Cambridge: Cambridge University Press).
1903 doi:10.1017/CBO9781139021562.011
- 1904 Woodcock, D. C., Gilbert, J. S., and Lane, S. J. (2012). Particle-water heat transfer during explosive
1905 volcanic eruptions. *Journal of Geophysical Research. Solid Earth* 117. doi:http://dx.doi.org/10.1029/
1906 2012JB009240
- 1907 Woods, A. W. (2010). Turbulent Plumes in Nature. *Annual Review of Fluid Mechanics* 42, 391–412.
1908 doi:10.1146/annurev-fluid-121108-145430
- 1909 Woods, A. W. and Bower, S. M. (1995). The decompression of volcanic jets in a crater during explosive
1910 volcanic eruptions. *Earth and Planetary Science Letters* 131, 189–205. doi:10.1016/0012-821X(95)
1911 00012-2

- 1912 Zanchettin, D., Timmreck, C., Bothe, O., Lorenz, S. J., Hegerl, G., Graf, H.-F., et al. (2013). Delayed
 1913 winter warming: A robust decadal response to strong tropical volcanic eruptions? *Geophysical Research*
 1914 *Letters* 40, 204–209. doi:10.1029/2012GL054403
- 1915 Zhang, X., Li, S., Yu, D., Yang, B., and Wang, N. (2020). The Evolution of Interfaces for Underwater
 1916 Supersonic Gas Jets. *Water* 12, 488. doi:10.3390/w12020488
- 1917 Zhong, Y., Miller, G. H., Otto-Bliesner, B. L., Holland, M. M., Bailey, D. A., Schneider, D. P., et al. (2011).
 1918 Centennial-scale climate change from decadal-paced explosive volcanism: A coupled sea ice-ocean
 1919 mechanism. *Climate Dynamics* 37, 2373–2387. doi:10.1007/s00382-010-0967-z
- 1920 Zhu, Y., Toon, O. B., Jensen, E. J., Bardeen, C. G., Mills, M. J., Tolbert, M. A., et al. (2020). Persisting
 1921 volcanic ash particles impact stratospheric SO₂ lifetime and aerosol optical properties. *Nature*
 1922 *Communications* 11, 4526. doi:10.1038/s41467-020-18352-5
- 1923 Zimanowski, B. and Büttner, R. (2003). Phreatomagmatic explosions in subaqueous volcanism. In
 1924 *Geophysical Monograph Series*, eds. J. D. L. White, J. L. Smellie, and D. A. Clague (Washington, D. C.:
 1925 American Geophysical Union), vol. 140. 51–60. doi:10.1029/140GM03
- 1926 Zimanowski, B., Büttner, R., Dellino, P., White, J. D. L., and Wohletz, K. H. (2015). Chapter
 1927 26 - Magma–Water Interaction and Phreatomagmatic Fragmentation. In *The Encyclopedia of*
 1928 *Volcanoes (Second Edition)*, ed. H. Sigurdsson (Amsterdam: Academic Press). 473–484. doi:10.
 1929 1016/B978-0-12-385938-9.00026-2

5 TABLES

Table 1 List of variables and subscript nomenclature.

Variable	Description	Units
a	Radius of conduit or plume	m
A	Cross-sectional area of conduit or plume	m ²
B	Entrainment weighting for αRT scenario	-
C	Heat capacity	J/(kg K)
c	Sound speed	m/s
c_{H_2O}	Concentration of water dissolved in melt	wt. %
D_0	Power law exponent for initial particle size distribution	-
E_s	Particle fracture surface energy	J/m ²
\dot{E}	Energy flux	J/s
ΔE_{ss}	Specific fragmentation energy (per mass of melt)	J/(kg m)
F_{fric}	Frictional pressure loss	Pa/m
f	Friction factor	-
g	Gravitational acceleration	m/s ²
h	Enthalpy	J/kg
h_{vap}	Bulk mixture enthalpy at $T = T_{sat}$ and $x_v = 1$	J/kg
h_{vap}	Bulk mixture enthalpy at $T = T_{sat}$ and $x_v = 0$	J/kg
K	Bulk modulus	Pa
L_d	Decompression length scale	m
L_X	Crossover length scale	m
M	Mach number	-
N_i	Number of particles in size bin i	-
N_ϕ	Number of particle size bins	-

Continuation of Table 1

Variable	Description	Units
n	Mass fraction	-
n_{ec}	Mass fraction of external water infiltrating the conduit	-
r	Particle radius	m
r_{c1}	Critical particle radius for maximum effective porosity	m
r_{c2}	Critical particle radius for zero effective porosity	m
R_v	Gas constant for water vapor	J/(kg K)
p	Pressure	Pa
p_{choke}	Theoretical gas pressure for a choked vent	Pa
\dot{p}	Magma decompression rate	MPa/s
Δp_b	Bubble overpressure	MPa
q	Mass flux	kg/s
q_c	Adjusted conduit mass flux (MER) for hydrovolcanic simulations	kg/s
Q_0	Reference conduit MER for control ($Z_e = 0$) simulations	kg/s
Q_{crit}	Critical MER to reach the tropopause	kg/s
S	Specific surface area of particles	m ² /kg
T	Temperature	K
T_g	Glass transition temperature lower bound	K
ΔT_g	Temperature range for glass transition	K
T_0	Initial magma temperature	K
T_{ref}	Reference temperature for enthalpy calculations	K
T_{sat}	Water saturation temperature	K
u	Vertical velocity (radially averaged)	m/s ²
x_v	Water phase dryness fraction	-
z	Vertical coordinate	m
Z_e	External surface water depth	m
$Z_{e,choke}$	Critical water depth at which hydrostatic pressure exceeds choking pressure	m
Z_{tp}	Height of tropopause	m
Z_{max}	Maximum height of eruption column	m a.v.l.
Z_{nbl}	Neutral buoyancy (spreading) height of eruption column	m a.v.l.
α	Entrainment coefficient	-
α_{RT}	Rayleigh-Taylor entrainment coefficient	-
β	Vent overpressure ratio	-
ζ	Fragmentation energy efficiency	-
η	Magma mixture dynamic viscosity	Pa s
Λ	Particle roughness scaling parameter	-
λ	Water vapor condensation rate	s ⁻¹
ρ	Density	kg/m ³
ϕ	Particle sieve size	-
ϕ_μ	Mean ϕ size of quench fragmented particles	-
ϕ_σ	Standard deviation ϕ size of quench fragmented particles	-
χ	Volume fraction	-
χ_i	Porosity of particle size bin i	-

Continuation of Table 1

Variable	Description	Units
χ_0	Threshold porosity for conduit fragmentation	-
ψ_{SO_2}	Gaussian profile for vertical distribution of SO_2 injection	-
ω	Jet-water interface acceleration for Rayleigh-Taylor entrainment	-
Subscripts:		
—	Bulk mixture (no subscript for material property)	
<i>a</i>	Dry air phase	
<i>b</i>	Bubble gas properties in pyroclasts	
<i>c</i>	Property of mixture in the conduit or vent	
<i>d</i>	Property after vent decompression	
<i>e</i>	Property of external water (MWI model) or air (plume model)	
<i>f</i>	"Final" value, or next iteration step	
<i>i</i>	Particle size bin <i>i</i>	
<i>l</i>	Liquid water phase	
<i>m</i>	Magma phase (excluding bubbles)	
<i>s</i>	"Solids" phase (melt + bubbles)	
<i>v</i>	Water vapor phase	
<i>w</i>	Total water phase in conduit or plume (liquid + vapor)	
0	Initial value	

Table 2. List of simulations sets highlighting varied model parameters: Atmospheric profile, external water temperature T_e , decompression length switch, crossover length switch, entrainment equation, PSD power-law exponent D , particle roughness scale Λ , and fragmentation energy efficiency ζ .

Name	Atmosphere	T_e (K)	use L_d ?	use L_X ?	α Equation	D	Λ	ζ
<i>Reference</i>	Iceland	274	Yes	Yes	27	2.9	10	0.1
<i>Low-Lat</i>	Ecuador	294	Yes	Yes	27	2.9	10	0.1
<i>No-L_d</i>	Iceland	274	No	Yes	27	2.9	10	0.1
<i>No-L_X</i>	Iceland	274	Yes	No	27	2.9	10	0.1
<i>No-L_d-No-L_X</i>	Iceland	274	No	No	27	2.9	10	0.1
<i>αRT</i>	Iceland	274	Yes	No	35	2.9	10	0.1
<i>High-Λ</i>	Iceland	274	Yes	Yes	27	2.9	25	0.1
<i>High-ζ</i>	Iceland	274	Yes	Yes	27	2.9	10	0.2
<i>Low-ζ</i>	Iceland	274	Yes	Yes	27	2.9	10	0.05
<i>High-D</i>	Iceland	274	Yes	Yes	27	3.2	10	0.1

FIGURE CAPTIONS

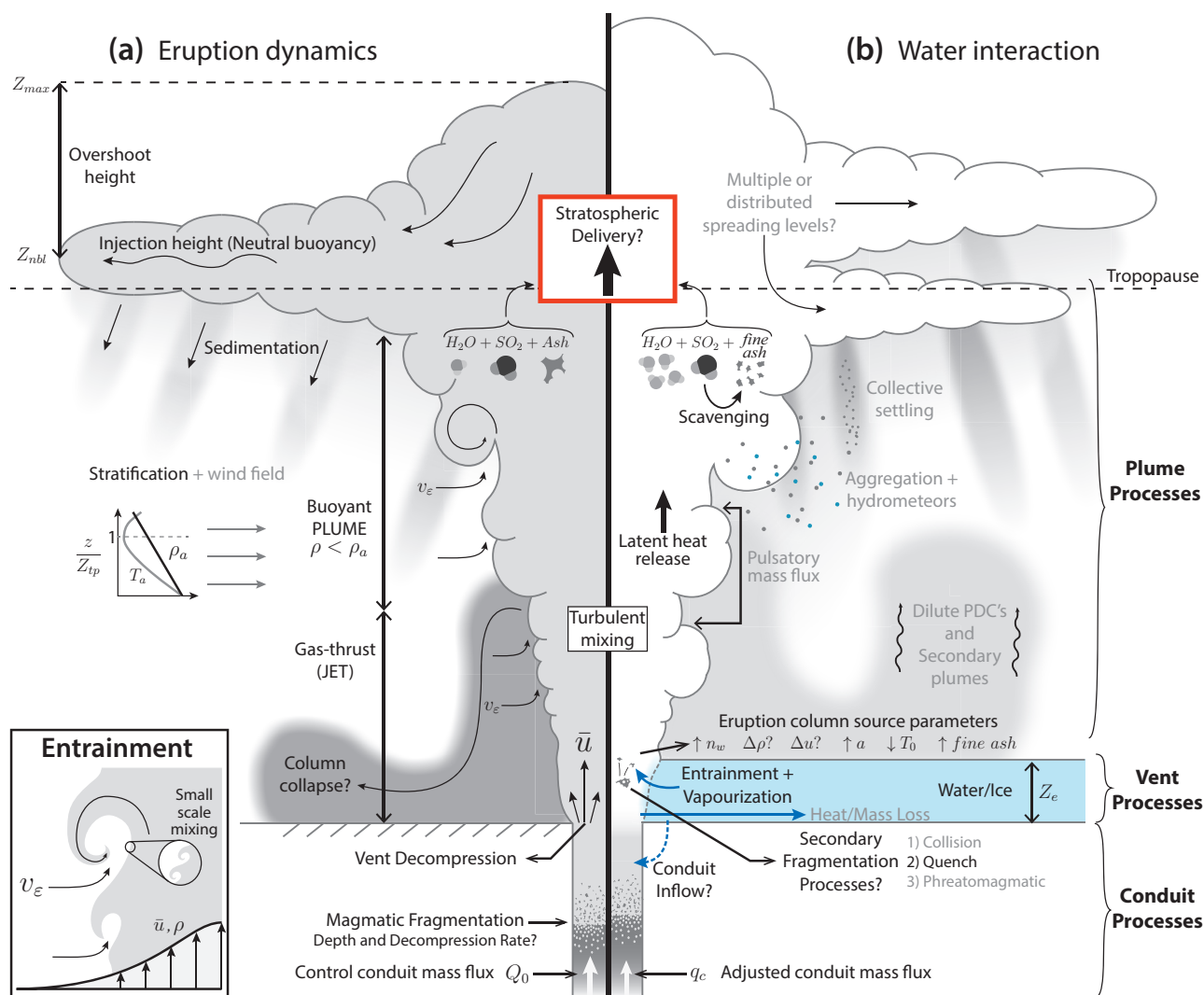


Figure 1. Summary of eruption processes from conduit to atmospheric dispersal. See text for a description of processes and their relevance for SO_2 transport. See Table 1 for a complete description of symbols. (a) Dynamical processes during a sustained, "dry" Plinian eruption. Inset: illustration of the entrainment process. (b) Summary of processes influenced by surface water interaction during a hydrovolcanic eruption. Processes in lighter gray text are those not considered in this study, but which are relevant to hydrovolcanic eruptions processes and may play a role in stratospheric delivery of SO_2 .

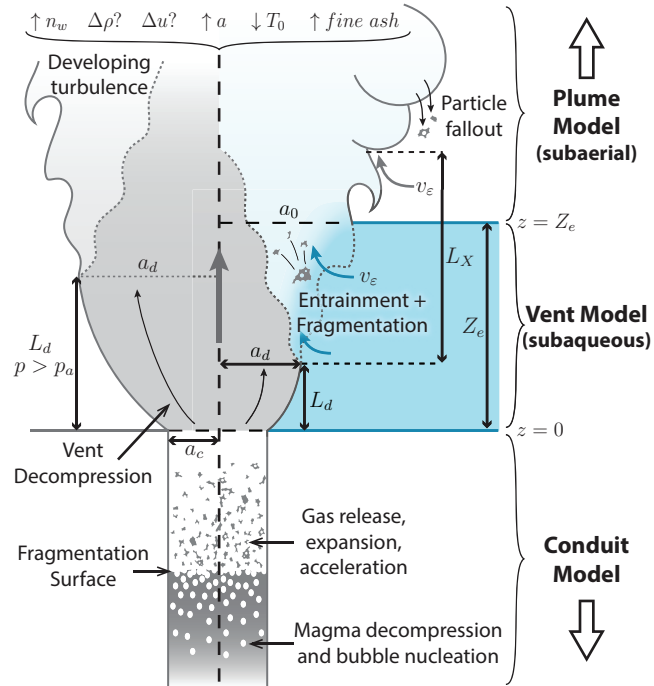


Figure 2. Schematic summary of coupled model, highlighting geometry of the vent and MWI region. The left and right sides are divided between a control scenario with no external water and a scenario with a shallow water layer, respectively. In the hydrovolcanic case, decompression of the erupting jet of gas and pyroclasts is suppressed relative to the dry control scenario (indicated by decompression length L_d and radius a_d), and initiation of turbulent mixing with external water results in water entrainment and quench fragmentation. In the water layer scenario shown here, water depth Z_e is greater than the decompression length L_d but less than the height at which large entraining eddies are fully developed, $L_d + L_X$. See Table 1 and Sections 2.2, 2.3, and 2.4 for a complete description of symbols and processes.

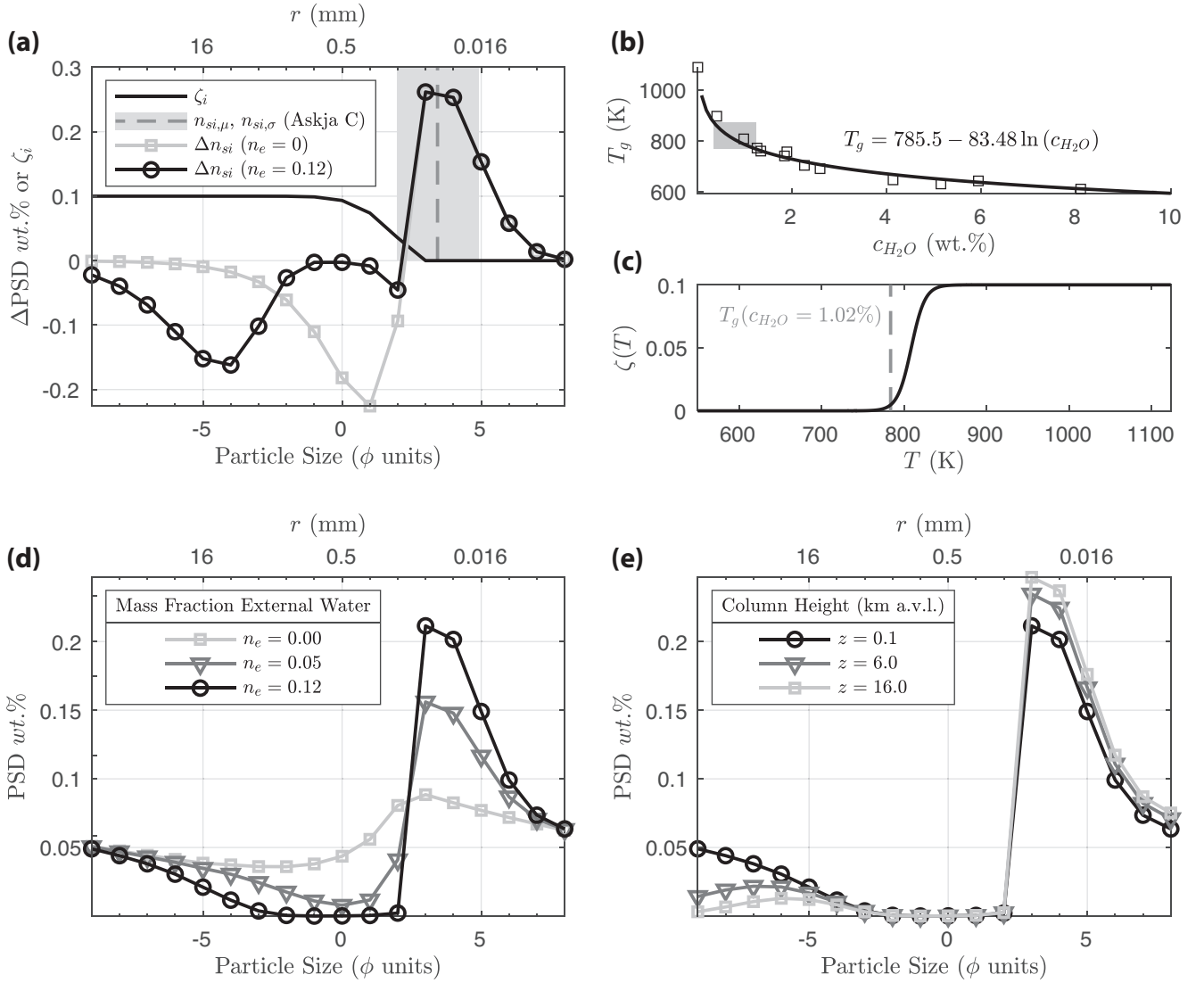


Figure 3. PSD and quench fragmentation model for rhyolitic melt, using a single example simulation with $q = 1.03 \times 10^8$ kg/s, $Z_e = 120$ m, and $\zeta = 0.1$. (a) Change in PSD, ($\Delta n_{s,i} = -n_{s,i,0} + n_{s,i,f}$) from Equation 52 at two different mass fractions of entrained external water n_e . The “output” particle sizes of quench fragmentation $n_{s,i,f}$ are defined from the mean and standard deviation (in ϕ units, shown as the vertical grey dashed line and shaded region, respectively) of the Askja phase C deposit, as reported in Costa et al. (2016). The “input” particle sizes $-n_{s,i,0}$ (i.e. from which mass is removed to generate the products of quench fragmentation), are a function of available surface area in the PSD coarse fraction (Equation 49), and evolve as the total PSD coarse fraction is progressively depleted with increasing n_e (see also panel (d)). The solid black line shows ζ_i (Equation 47), which defines the size bins for the “coarse” fraction. (b) Glass transition temperature T_g data from Dingwell (1998) (squares) and curve fit (black line) as a function of concentration of dissolved water in the melt. The grey shaded rectangle shows the range of values in the *Reference* set of simulations after exit from the vent. (c) Fragmentation energy efficiency as a function of temperature (Equations 45, 46) for $T_g = 784$ K. (d) Evolution of the total PSD $n_{s,i}$ during quench fragmentation. The initial power law PSD, with no external water, and therefore no quench fragmentation ($n_e = 0$), is shown in light grey, with a reduced mass fraction in the range $\phi \lesssim 2$ arising from the large porosity and consequently low density of these particles (Equations 11-13). The remaining dark grey and black lines show $n_{s,i}$ after quench fragmentation for $n_e = 0.05$ and $n_e = 0.12$, respectively. After sufficient external water is entrained ($n_e \approx 0.12$) to cross T_g , $n_{s,i}$ does not evolve further from quench fragmentation. Note that owing to their larger surface area, particles are preferentially depleted in the mid-size-range ($-3 \lesssim \phi \lesssim 2$). (e) Further evolution of $n_{s,i}$ due to particle fallout, after water breach and during subaerial column rise, with preferential fallout of the coarsest fraction ($\phi \lesssim -3$) and additional enriching of fines.

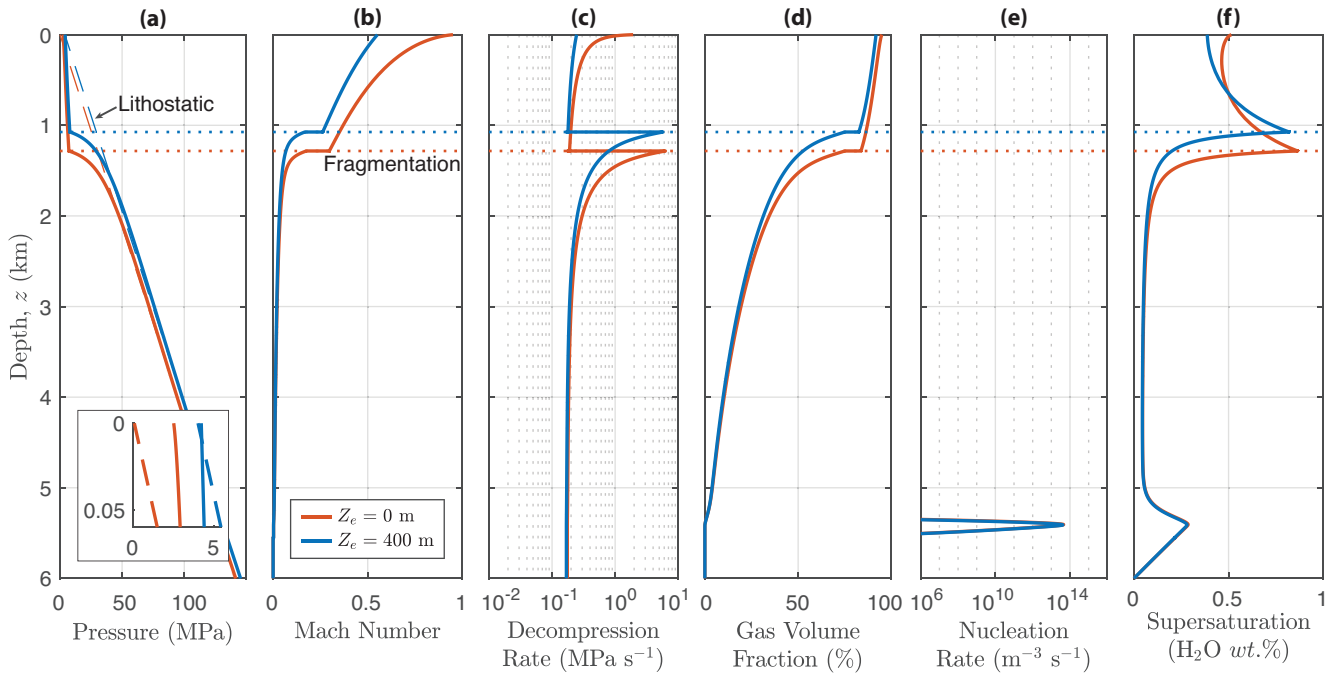


Figure 4. Example conduit model output from the *Reference* set (see Table 2) versus depth below the vent for a pair of simulations: red lines show a “dry” control run with $a_c = 53.8$ m, $Z_e = 0$, and $Q_0 = 1.6 \times 10^8$ kg/s. Blue lines show a hydrovolcanic scenario with $a_c = 53.8$ m, $Z_e = 400$ m, and $q_c = 1.53 \times 10^8$ kg/s (blue lines). (a) Magma pressure. Inset: pressure in the top 60 m of the conduit (same units as panel (a) axes), highlighting the vent overpressure of the control run versus the pressure-balanced vent of the hydrovolcanic run. (b) Mach number. (c) Decompression rate. (d) Gas Volume Fraction. (e) Bubble Nucleation Rate. (f) Supersaturation of dissolved water (i.e. difference between dissolved water c_{H_2O} and water solubility).

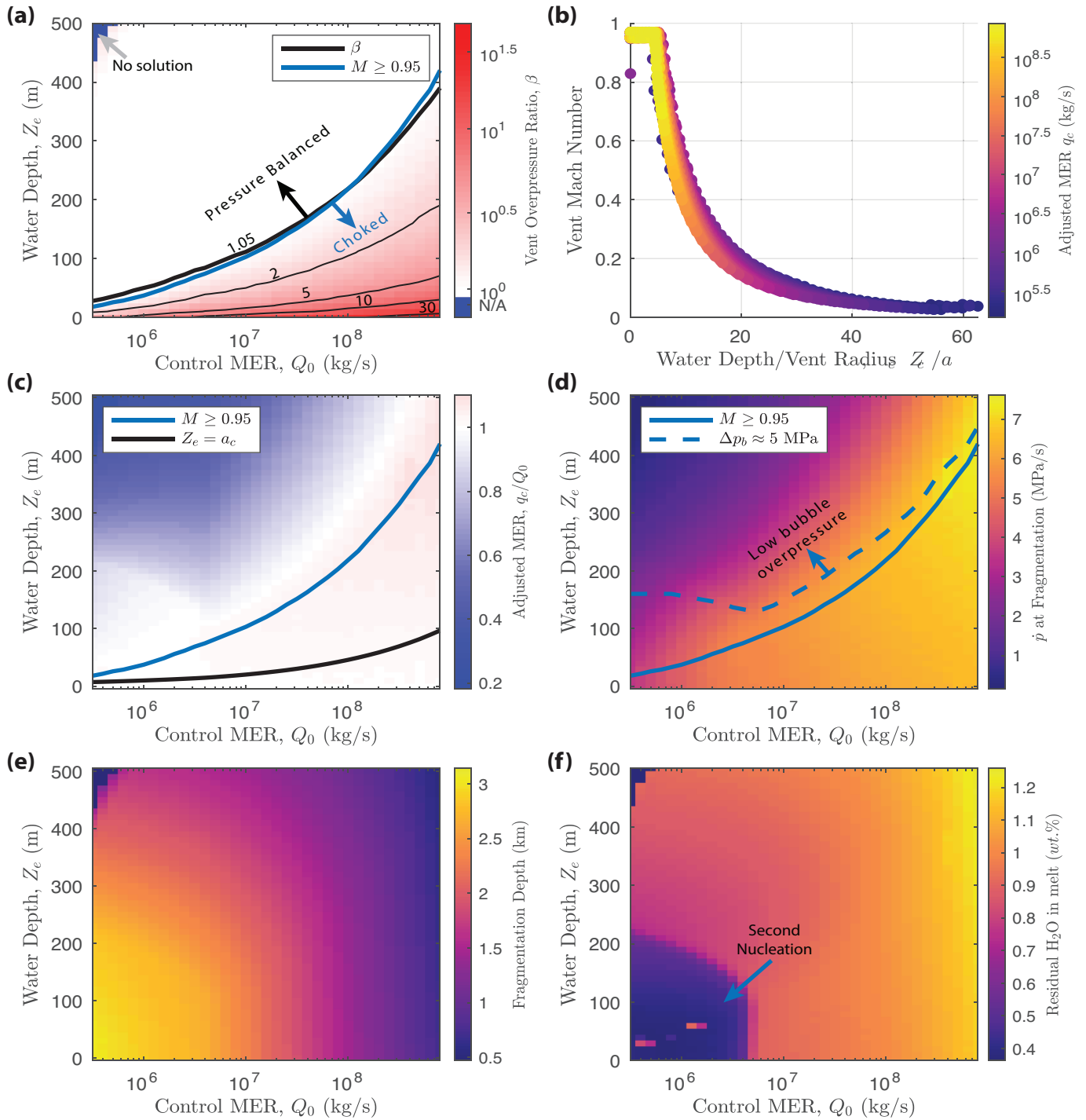


Figure 5. Conduit model output as a function of control MER, Q_0 , and external water depth, Z_e . (a) Vent overpressure β . The blue line in panels (a), (c), and (d) denotes the tolerance threshold for Mach number ($M = 0.95$), and the red line is the (approximately coincident) vent overpressure threshold, $\beta = 1.05$. The vent is choked and overpressured for water depths less than this. The blue region in the top left (high Z_e and low Q_0) are failed simulations - no viable conduit solutions were found in this region. (b) Vent Mach number. (c) Mass eruption rate adjustment for fixed conduit radius, relative to the control case for $Z_e = 0$. (d) Maximum decompression rate recorded at fragmentation ($\chi_0 = 0.75$). The dashed blue line highlights the maximum water depth for which peak bubble overpressure is at least 5 MPa, which is an approximate low bound for bubble wall rupture (Cas and Simmons, 2018). (e) Fragmentation depth. (f) Residual dissolved water in pyroclasts at the vent, highlighting a strong second nucleation event for low MER and water depths less than about 200 m.

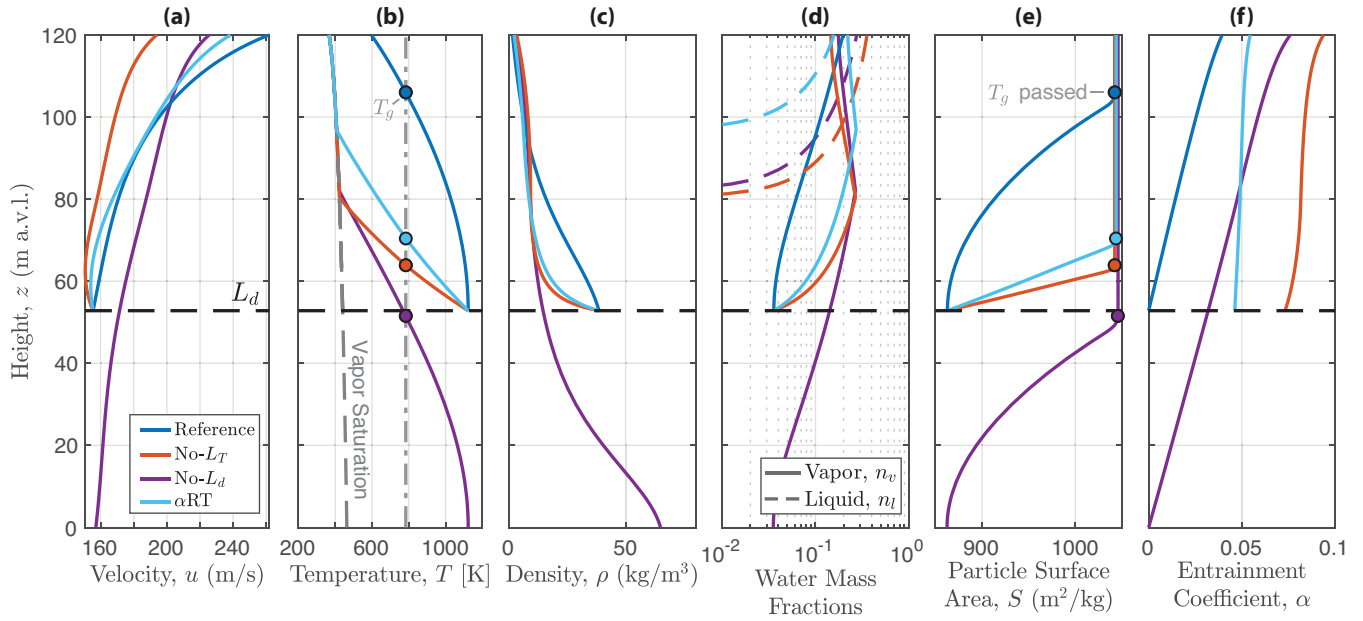


Figure 6. Example MWI model parameters versus position in the water layer above the vent for a single simulation at $q_c = 1.03 \times 10^8$ kg/s, and $Z_e = 120$ m. Four different water entrainment scenarios are shown: the *Reference* scenario using an entrainment condition modified by both decompression and crossover length scales (blue), a scenario with no scaling for turbulent mixing length (*no- L_X* , red), a scenario with no decompression length scale, where entrainment initiates immediately at the vent (*no- L_d* , purple), and a scenario using the weight Rayleigh-Taylor entrainment mode of Equation 35 (*αRT* scenario, light blue). (a) Vertical velocity. (b) Jet mixture temperature. (c) Jet bulk density. (d) Jet water liquid and vapor mass fractions. (e) Specific surface area of pyroclasts. (f) Local entrainment coefficient. Colored circles in (b), (e) highlight the crossing of the glass transition temperature.

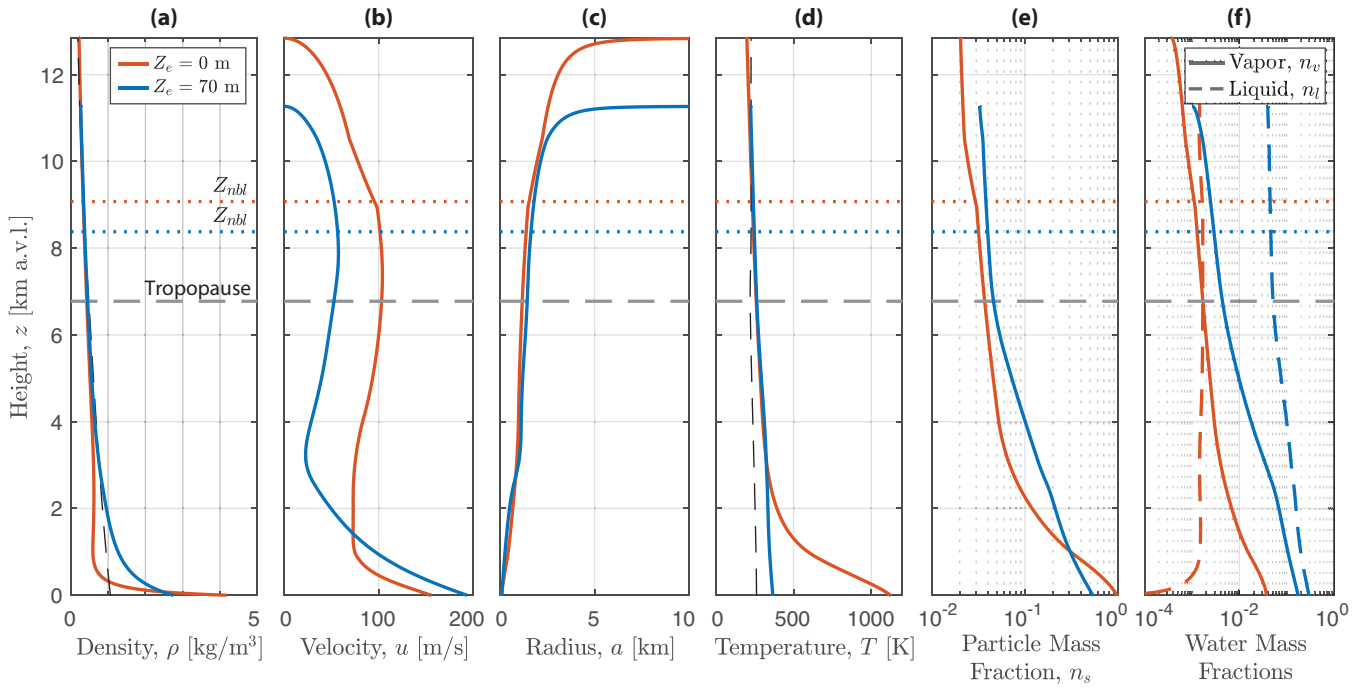


Figure 7. Example plume model output from the *Reference* set (see Table 2) versus height above the vent for a pair of simulations: red lines show a “dry” control run with $a_c = 20.0$ m, $Z_e = 0$, and $Q_0 = 1.00 \times 10^7$ kg/s. Blue lines show a hydrovolcanic scenario with $a_c = 20.0$ m, $Z_e = 70$ m, and $q_c = 1.01 \times 10^7$ kg/s (blue lines). (a) Bulk density. (b) Vertical velocity. (c) Column Radius. (d) Bulk temperature. (e) Particle mass fraction. (f) Water liquid and vapor mass fractions. Horizontal dotted lines show the level of neutral buoyancy for each case, and the horizontal dashed gray line shows the height of the tropopause (note y-axis is kilometers above vent level).

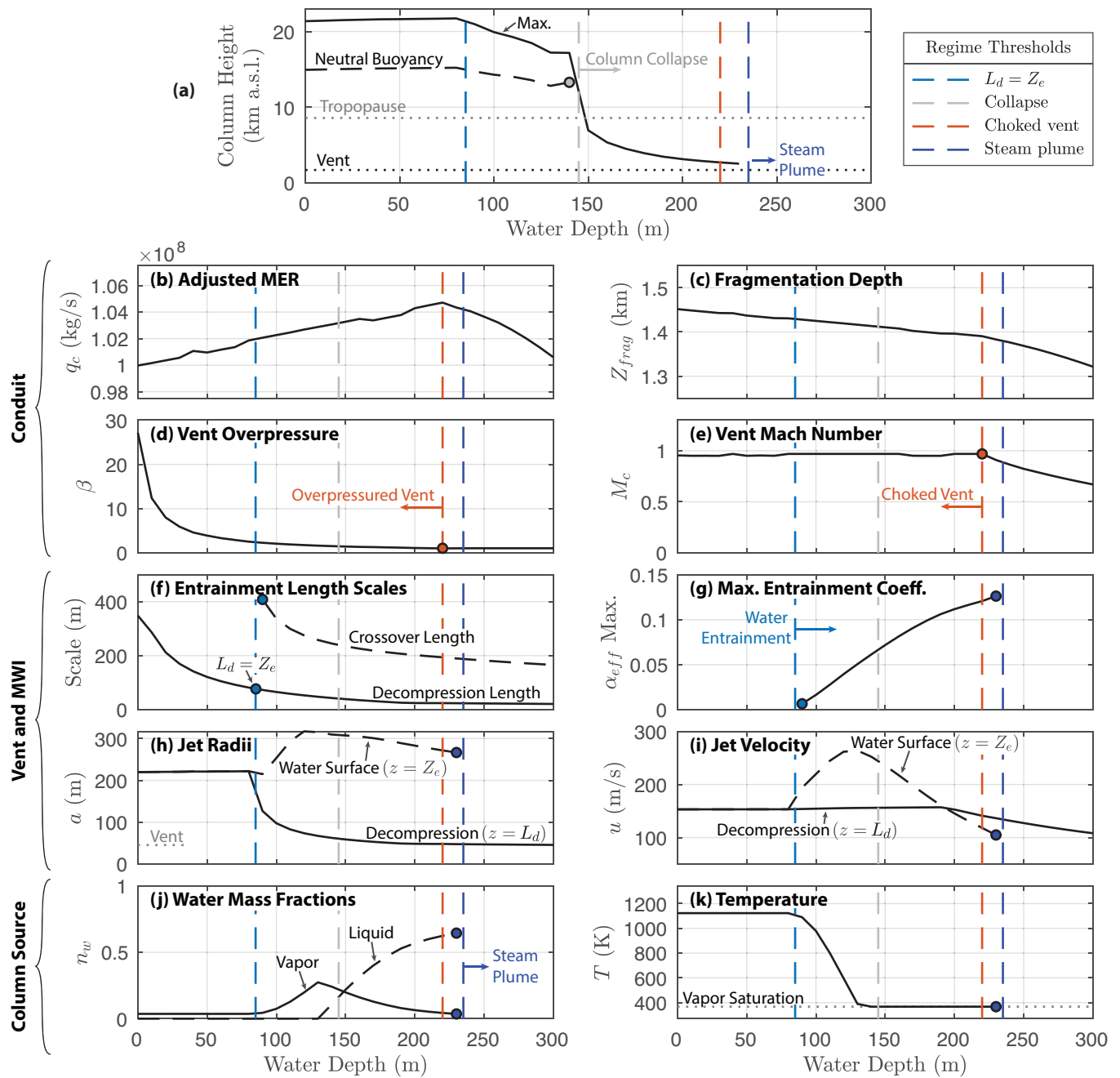


Figure 8. Output of the coupled model (conduit, vent, and column) *Reference* scenario for $Q_0 = 10^8$ kg/s and a range of water depths. Behavior thresholds for decomposition length, column collapse, vent choking, and steam plumes corresponding to regimes in Figure 9a are marked with vertical dashed lines. (a) Eruption column maximum height and neutral buoyancy height above sea level, shown with vent and tropopause altitude. Conduit results: (b) adjusted conduit MER q_c ; (c) depth of fragmentation surface; vent (d) overpressure β and (e) Mach number M . MWI model results: (f) decomposition L_d and crossover L_X length scales; (g) maximum value of the entrainment coefficient in the water layer; (h) radius of the vent and jet after initial decompression (at $z = L_d$) and at the water surface ($z = Z_e$); (i) velocity of the jet after initial decompression (at $z = L_d$) and at the water surface ($z = Z_e$). Column source conditions: (j) vapor and liquid water mass fractions; (k) bulk mixture temperature.

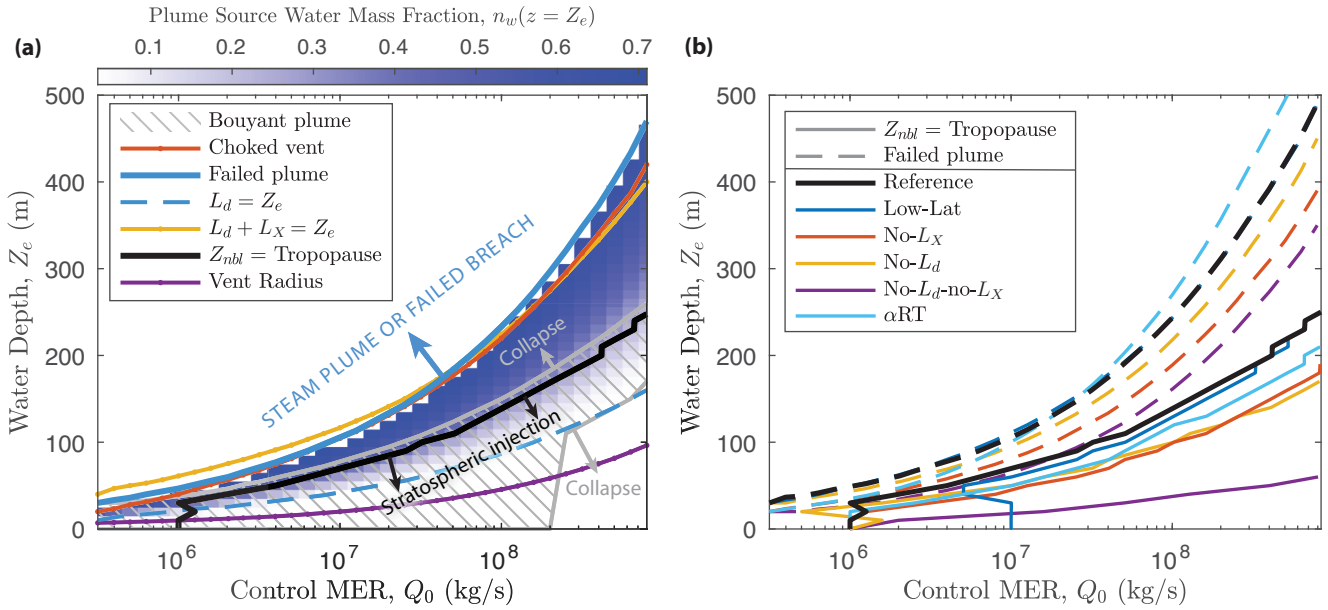


Figure 9. (a) Plume source water mass fraction as a function of MER and water depth, with overlaid thresholds for behavior of the coupled conduit-plume system. The red line marks the threshold for which the vent is choked and overpressured, with pressure-balanced, subsonic jets occurring at deeper depths. The decompression length is equal to water depth at the blue dashed line, which is the depth above which water entrainment begins. Bouyant columns occur within the grey hatched region, with column collapse elsewhere. The steam plume threshold is marked by the solid blue line - failed plumes with only negligibly small amounts of steam reach the water surface for depths greater than this (indicated by the blue arrow). Finally, the solid black line marks the water depth above bouyant columns breach the tropopause. (b) Variation in the critical MER to reach the tropopause (solid lines) and maximum water depth before plume failure (i.e. the steam plume condition, dashed lines) for different simulation scenarios (see Table 2). Black lines are for the *Reference* scenario (high latitude atmosphere), while blue lines are for the low latitude atmosphere. The remaining colors are for the four scenarios with different water entrainment parameterizations: no mixing length (*No- L_X* , red), no decompression length (*No- L_d* , yellow), neither mixing length nor decompression length (*No- L_X -no- L_X* , purple), and the weighted Rayleigh-Taylor entrainment mode (αRT , light blue).

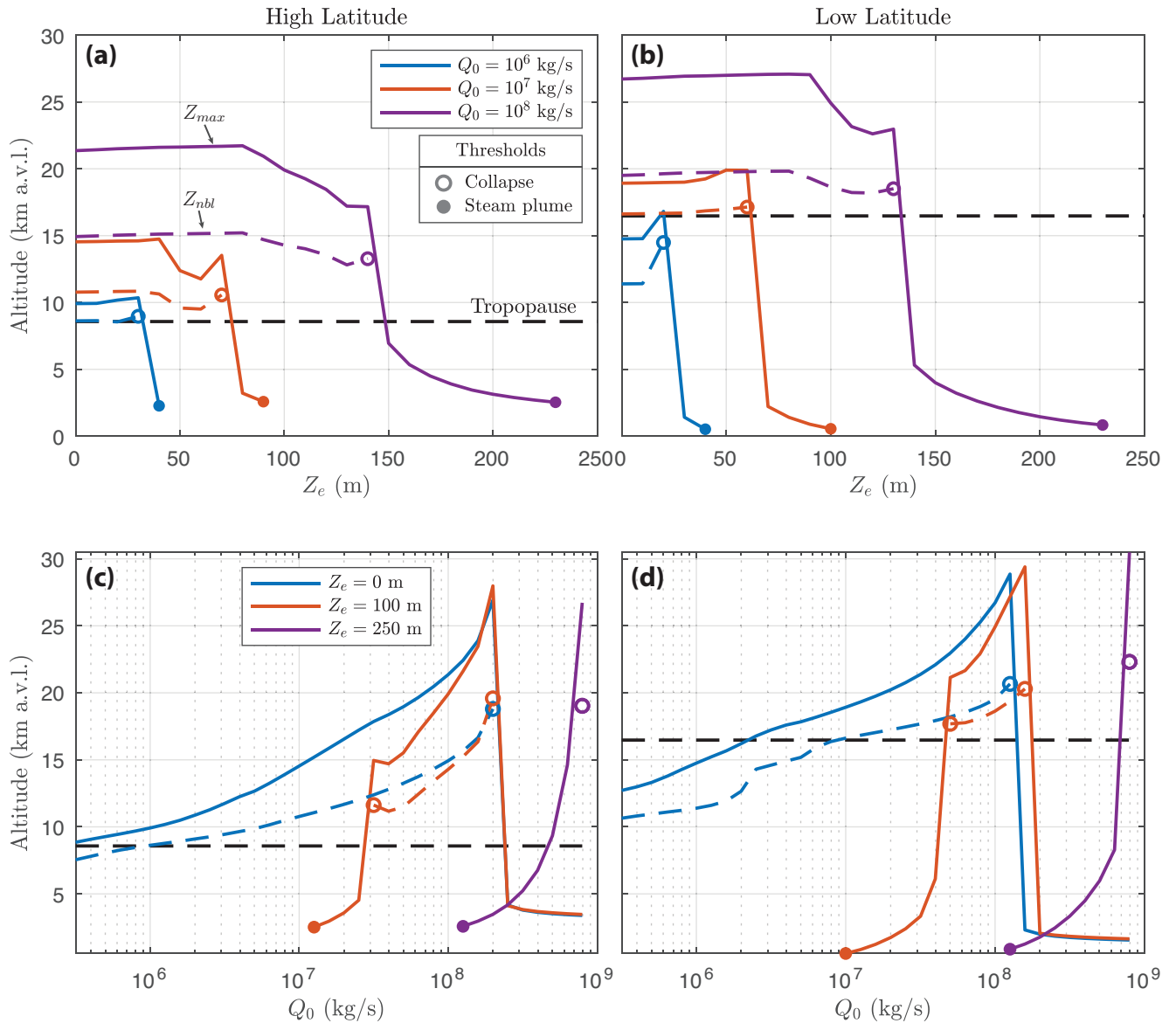


Figure 10. Eruption column height (above vent level) versus (a,b) surface water depth for three control values of MER and (c,d) MER for three fixed values of water depth. Left column plots (a,c) are for high latitude and right column (b,d) for low latitude atmospheres. For all plots, solid lines denote maximum column height, Z_{max} , dashed lines are height of neutral buoyancy, Z_{nbl} , open circles indicate threshold values for column collapse, and closed circles indicate threshold values for steam plumes at the water surface.

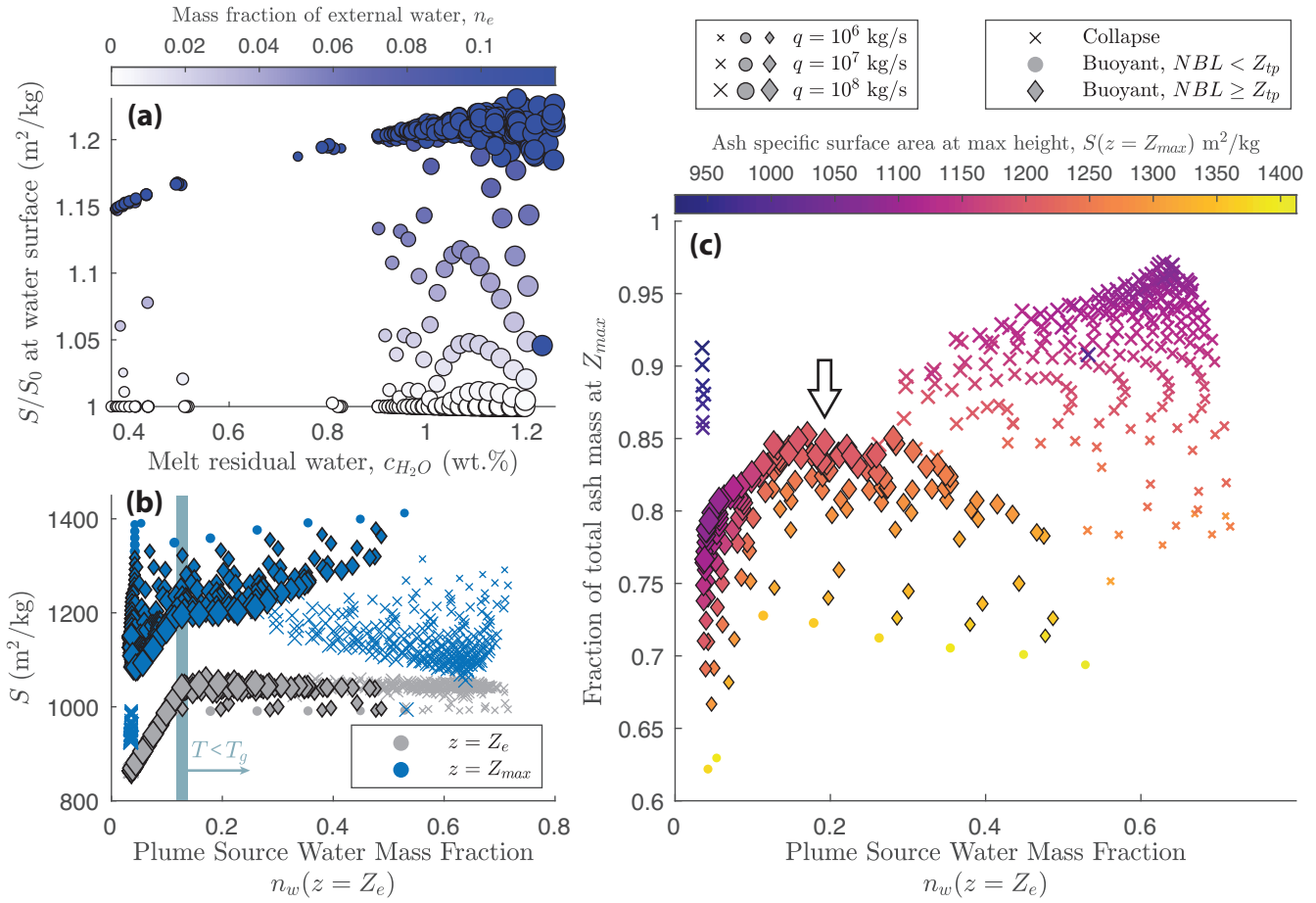


Figure 11. Effects of MWI and sedimentation on particle specific surface area S . (a) Specific surface area, S , immediately after the jet breaches the water surface ($Z = Z_e$), as a function of c_{H_2O} , the water mass fraction still dissolved in the melt after conduit exit. Symbols are sized according to MER at the vent and colored according to the mass fraction of entrained external water. The dissolved water content controls the glass transition temperature, T_g , which in turn is the primary limiting factor in the model for how much surface area can be generated during quench fragmentation. (b) S at two different heights in the eruption column: at column source, immediately after MWI ($Z = Z_e$, grey symbols), and at the column maximum height ($z = Z_{max}$, blue symbols) as a function of water mass fraction at column source. Symbol sizes as in (a). An 'x' denotes a collapsing column, a filled circle denotes a column that is buoyant but with Neutral Buoyancy Level (NBL) below the tropopause, and diamonds are columns that are buoyant with NBL at or above the tropopause. Evolution from grey to blue symbols is a result of sedimentation over the rise height of the column. The approximate water mass fraction above which the pyroclasts cool below the glass transition temperature T_g is marked with a vertical blue bar. (c) Fraction of particle mass remaining in the column at its maximum rise height as a function of column source water mass fraction. Symbols are sized by MER as in (a) and (b), and colored according to the value of S at maximum column height. Symbol shapes as in (b). The arrow highlights the subset of simulations with NBL above the tropopause and where the column retains increased (relative to "dry" runs) particle mass and specific surface area.

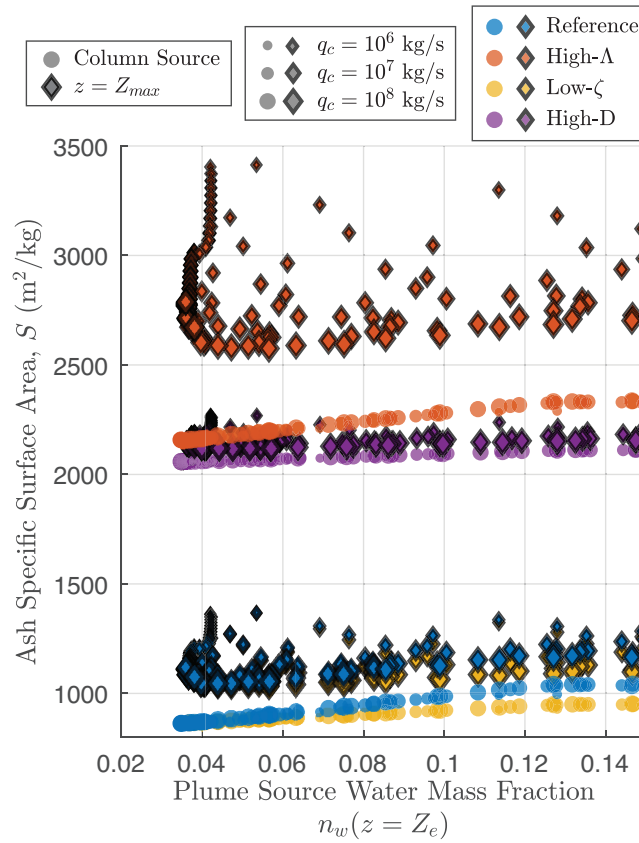


Figure 12. Pyroclast specific surface area as a function of water mass fraction at the water surface (circles) and height of neutral buoyancy (diamonds) for scenarios with different fragmentation properties. The *Reference* scenario is shown in blue. Reducing the fragmentation energy efficiency to $\zeta = 0.05$ (*Low- ζ* scenario, yellow symbols) reduces the amount of energy consumed to generate surface area per unit mass of entrained water, resulting in a smaller increase in S during MWI relative to the *Reference* scenario. Conversely, a high initial value of the PSD power-law exponent, $D = 3.2$ (*High- D* scenario, purple symbols), concentrates initial particle mass in the fine fraction. Because of the fixed particle sizes for output from quench fragmentation used here (see Figure 3), there is relatively little particle mass available to fragment for the creation of new surface area and the relative change in S with water entrainment is small. Finally, increasing the particle roughness scale, $\Lambda = 25$ (*High- Λ* scenario, red symbols), results in initially high particle surface area, but also a greater energy requirement to generate new particles of a given size. This scenario results in the highest absolute changes in particle surface area after quench fragmentation and sedimentation, but a smaller relative change than for the *Reference* scenario.

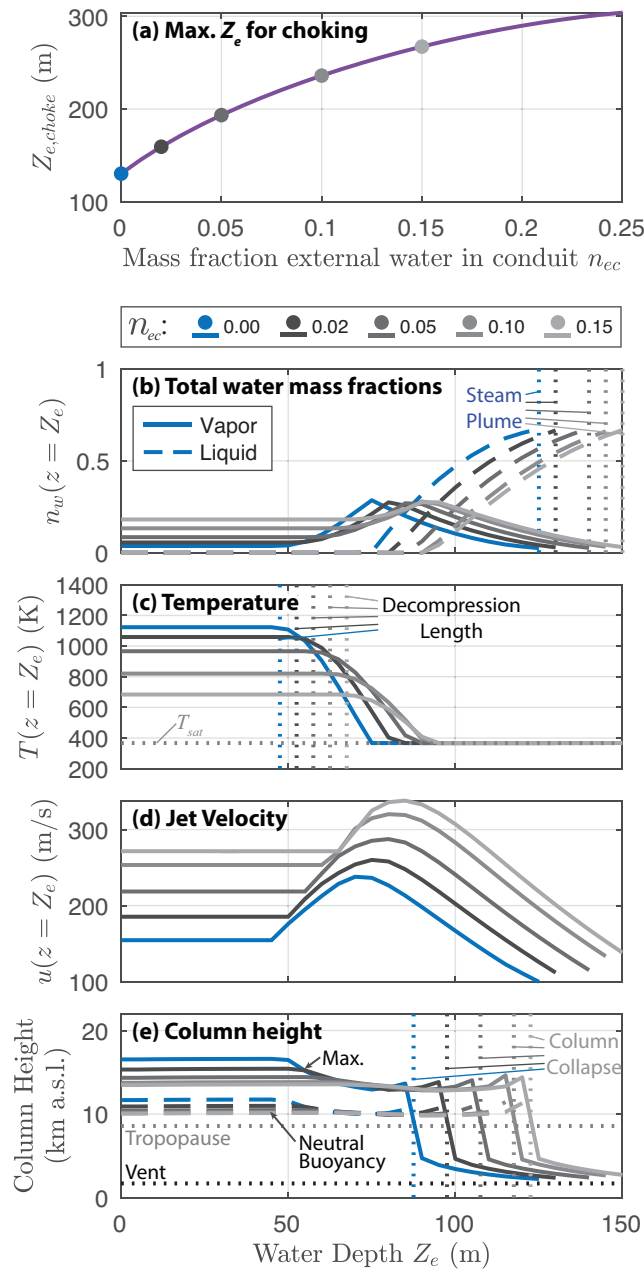


Figure 13. Sensitivity analysis for infiltration of a prescribed mass fraction of external water infiltrating into the conduit n_{ec} . Simulations use a magmatic mass flux of 2×10^7 kg/s, and all other parameters including atmospheric profiles are held fixed relative to the *Reference* scenario. Vent conditions are calculated according to Equations 63 and 65. (a) Critical surface water depth at which hydrostatic pressure exceeds vent choking pressure (Equation 63) as a function of water infiltration into the conduit. Circles highlight the values of n_{ec} used in the simulations shown for panels (b) to (e). Panels (b)-(d) show parameters at the subaerial eruption column source after breach of the water surface ($z = Z_e$). (b) Total mass fractions of liquid and vapor water phases. Vertical dotted lines show the water depth threshold for steam plumes for each of the conduit water scenarios. (c) Jet mixture temperature. Vertical dotted lines show the threshold at which decomposition length scale L_d is equal to water depth Z_e . (d) Jet vertical velocity. (e) Maximum eruption column height (solid lines) and level of neutral buoyancy (dashed lines). Vertical dotted lines show the water depth threshold for column collapse.

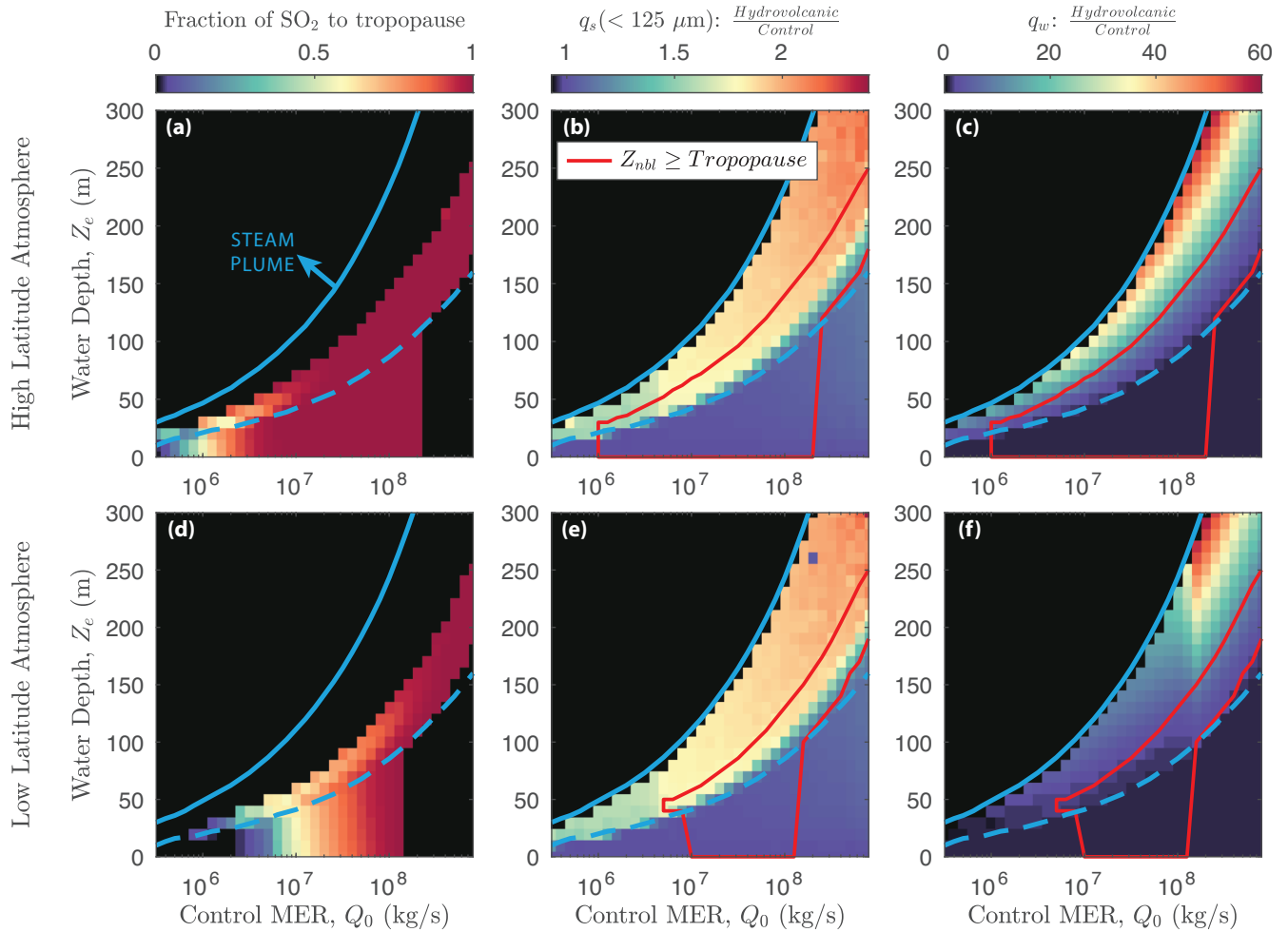


Figure 14. Estimated fraction of SO_2 , fine ash mass flux, and water mass flux to the stratosphere. (a) Estimated fraction of outgassed SO_2 injected above the tropopause assuming a gaussian injection profile centered about the height of neutral buoyancy (Equation 66), as a function of control MER Q_0 and water depth Z_e . In all panels, the dashed blue line is threshold water depth for water entrainment (decompression length equal to water depth, $L_d = Z_e$), and the solid blue line is the threshold depth for steam plumes (see Figure 9). Black regions indicate column collapse. (b) Fine ash mass flux to the eruption column maximum height as a ratio of hydrovolcanic ($Z_e > 0$) to control ($Z_e = 0$) simulations, for particle diameters less than $125 \mu\text{m}$. Red line outlines simulations with buoyant plumes at spreading heights at or above the tropopause. (c) Water mass flux to the eruption column maximum height as a ratio of hydrovolcanic ($Z_e > 0$) to control ($Z_e = 0$) simulations. Black regions indicate the steam plume regime in panels (b), (c), (e), (f). Panels (a)-(c) are for with a high latitude (Iceland) atmospheric profile (*Reference* scenario). Panels (d)-(f) are the same as (a)-(c), respectively, but for the low latitude (Equador) atmosphere (*Low-lat* scenario).